Investigating and Improving the Timepix Performance in Imaging Ac-225 and Daughter Nuclides

by

E. van Lieshout

to obtain the degree of Master of Science
at the Delft University of Technology,
to be defended publicly on June 29, 2023.

Student number: 4617827

Project duration: October 24, 2022 – June 15, 2023

Thesis committee:

Dr. ir. A. G. Denkova,	TU Delft, supervisor
Dr. ir. D. Lathouwers,	TU Delft
Dr. ir. M. C. Goorden,	TU Delft
Dr. ing. J. Plomp,	TU Delft, supervisor

Acknowledgements

First of all, I would like to express my sincere gratitude to my supervisors, Antonia Denkova and Jeroen Plomp. Their guidance and support throughout this thesis were truly invaluable. Our meetings were always light-hearted, and whenever I felt lost, guided me into the right direction. This research was very interesting and I cannot emphasise enough how thankful I am for having this incredible opportunity.

Moreover, this research could not have been concluded without the help from staff members from the TUDelft Reactor Institute, specifically Ernst van der Wal, Michel Thijs and Henk van Doorn. Ernst provided us with essential 3D prints which were vital for the Timepix measurement setup. Michel Thijs developped a code for controlling the x-y translation table for the α calibration. Henk van Doorn was incredibly helpfull whenever I needed radioactive sources for my experiments. I am very grateful.

Additionally, I want to give a special thanks to Thomas Toet, a fellow student who worked alongside me with the Timepix detector. Having him as a sparring partner helps to stay sharp and keep critical about the results and underlying theory. Thank you for the experience.

Furthermore, an appreciation for the members of my thesis committee, Danny Lathouwers and Marlies Goorden. I am grateful for them taking the time to read and review this thesis.

Last but not least, a big thanks to everyone from the research group. Our coffee breaks and lunches were always enjoyable, and they provided me with the much-needed opportunity to clear my head and share any concerns. This has been essential for maintaining a good mindset during the research.

E. van Lieshout
Leiden, June 2023

Abstract

The main objective of this research was to determine the feasibility of using the Timepix3 detector, a novel hybrid-pixel detector developed by CERN, as a tool for imaging ex-vivo slices of tumour tissue treated with ^{225}Ac Targeted Alpha Therapy. Targeted Alpha Therapy using ^{225}Ac-PSMA shows promise as a therapeutic method, as it allows direct targeting of the tumour and precise irradiation of cancer cells while sparing healthy tissue due to the short range of α-particles (typically 50-100μm). However, due to the recoil effect, the daughters of ^{225}Ac can break loose from the targeting vector, potentially diffusing away from the tumour site and harming healthy tissue resulting in unwanted side effects. To investigate this, several experiments were conducted using the Timepix3 detector, capable of energy, spatial and time-resolved measurements. Before experiments could be conducted, a data processing tool was developed and an optimal bias voltage of 30V was determined. Subsequently, the Timepix was calibrated using a γ and α calibration, which yielded energy resolutions of 4.27±0.06% and 4.96±0.06% compared to 6.35±0.04% without calibration when measuring α-particles from ^{225}Ac locally. The Timepix3 was then tested using different collimators for whole surface measurements. For a plastic collimator (L/D=2.5, ⌀=1mm) the energy resolution improved from 15.7±0.3% to 11.9% and 9.6±0.1%. For a lead-glass collimator (L/D=50, ⌀=24.8μm) the energy resolution improved to 13.5% and 12.6±0.4%, here the uncalibrated resolution could not be determined. Finally, the spatial resolution of the Timepix was determined using the plastic collimator, which was 310±10μm. Based on the findings, the Timepix3 detector is not suitable for the proposed application, an imaging tool to determine nuclide distribution in ^{225}Ac-PSMA treated tissue samples, using this particular setup. However, using a different collimator with a more suitable L/D ratio should definitely be capable as this improves spatial and energy resolution further.

Furthermore, the Timepix3 detector was used in a clinical test to directly measure and determine the nuclide contents of the radio-pharmaceutical ^{225}Ac-PSMA separated by high-performance liquid chromatography. The results indicated an initially lower amount of ^{213}Po in the sample which grew over time This indicates that the HPLC is capable of separating individual nuclides. This result also demonstrated the potential use of the Timepix3 detector for these types of applications.

In experiments where the Timepix3 was placed inside a 70MeV and 120MeV proton beam to test its feasibility as a beam verification tool, the results were less successful due to the high intensity of the proton beam. However, it was concluded that it was still possible to measure scattered protons and secondary products.

Contents

1 Introduction

In 2020, an estimated 19.3 million people worldwide were diagnosed with cancer, and 10 million people died due to this disease, making cancer the second leading cause of death [1]. Despite advances in treatment that increase progression-free and overall survival, cancer remains incurable in many cases, with cycles of remission and recurrence being common [2]. Furthermore, each type of cancer can vary, requiring personalised treatment strategies. This highlights the need for innovative cancer treatments alongside traditional approaches such as surgery, chemotherapy, and radiation therapy.

This research focuses on investigating a treatment method called Targeted Alpha Therapy (TAT). TAT utilises an α-emitting nuclide that is bound to a targeting vector to deliver short-range radiation specifically to cancer cells [3][4]. One promising nuclide for TAT is ^{225}Ac. It has a favourable half-life of 9.9 days, multiple production routes, and increased cell-killing efficiency due to its emission of four α-particles in total [5][6]. However, the high cell-killing potential of ^{225}Ac due to the emitted α-particles could induce unwanted side effects. This is attributed to the recoil effect, where a small portion of the kinetic energy released during decay is transferred to the daughter nucleus, breaking the chemical bonds with the targeting vector and reducing its effectiveness in targeting cancer cells [7][8]. The extent of this problem is not yet fully understood due to the challenges in imaging α-particles. The Timepix, a novel hybrid-pixel detector, offers the potential to investigate the distribution of daughter nuclides of ^{225}Ac in TAT.

The Timepix detector consists of a semiconductor slab that converts radiation into detectable charge, and a readout chip containing pixels of 55μm x 55μm in size, which converts the charge into an output signal [9]. By processing the output data, it is possible to determine the type, energy, and position of the detected radiation particles. Previous research has shown that the Timepix can achieve a spatial resolution of up to 10μm and an energy resolution of 5-10% for α-particles with energies larger than 1.5MeV [10][11]. With these specifications, it may be possible to measure tissue slices of tumours treated with ^{225}Ac TAT and identify the distribution of different nuclides in the sample, considering that cancer cells range in size from 8μm to 20μm and the emitted α-particles of ^{225}Ac and ^{221}Fr differ by approximately 10% in energy [12][5].

Therefore, the main research question is: Is the Timepix3 detector able to image the distribution of ^{225}Ac and daughter nuclides in a tissue sample treated with Targeted Alpha Therapy? To answer this, a data processing code needs to be developed to transform the Timepix output data into particles and identify their type, energy, and position. Subsequently, different different collimators need to be tried in order to find the ideal setup.

In addition to the main research project, two related side projects were conducted to explore the capabilities of the Timepix detector in different applications. The first project took place at Erasmus MC, where clinical research is being conducted using ^{225}Ac-PSMA. In this case, the ^{225}Ac is labelled in-house, and the quality of the radio-pharmaceutical is assessed using γ spectroscopy, which indirectly measures the ^{225}Ac content through the detection of ^{221}Fr [13]. However, the Timepix detector has

the potential to directly measure the α -particles emitted by all nuclides in the sample. An experiment was conducted to measure the α -particles of a fraction of ^{225}Ac-PSMA that was passed through a High-Performance Liquid Chromatography (HPLC). This experiment aimed to determine whether the Timepix detector is suitable for such experiments and whether the HPLC is effective in separating differently labelled nuclides.

The second side project was conducted at HollandPTC, a facility where proton therapy is performed. In proton therapy, it is crucial to verify the beam energy and shape to ensure accurate dose delivery. Research is ongoing at HollandPTC to study the proton beam, including the detection of scattered protons and secondary particles in different scenarios. To assess the suitability of the Timepix detector for beam verification and other experiments in this context, the detector was placed inside the proton beam and on the side where the beam passed through a silicon wafer. The goal was to determine whether the Timepix detector can be effectively used for beam verification and other related measurements [14][15][16].

This research is structured in multiple chapters. In the first chapter, the theory and background information is given, which is about α radiation, TAT, the Timepix and related side projects. The subsequent chapter gives a structured overview of the conducted experiments. The results together with the discussion are given in the chapter thereafter, together with a small summary of the discussion and recommendations. Finally, the conclusions are given.

2

Theory & Background

2.1. Alpha radiation

There are different types of radiation, each with its own unique characteristics. For this research, α radiation is of particular importance. Therefore, some theory is dedicated to this type of radiation. α-decay, typically observed in unstable heavy nuclides, is characterised by the following general equation [17]:

$$ {}^{A}_{Z}X \rightarrow {}^{A-4}_{Z-2}Y^{-2} + {}^{4}_{2}He^{2+} + Q. \tag{2.1} $$

Here, a parent radionuclide (X) decays into a daughter nuclide (Y) and emits a high energy 4-Helium particle (He), also known as an α-particle or α radiation. Due to the spontaneous ejection of the Helium particle, the ejected particle has a 2+ charge[1]. The daughter nuclide is often left in an excited state, resulting in accompanying γ radiation. The released energy (Q) of α-decay, due to the difference in binding energy, is generally in the range of a few MeV. This energy is distributed as kinetic energy for the resulting particles in the following way:

$$ KE_Y = \frac{M_\alpha}{M_Y + M_\alpha} \qquad\qquad KE_\alpha = \frac{M_Y}{M_Y + M_\alpha}, \tag{2.2} $$

where KE_i is the kinetic energy of the daughter nucleus (Y) and the α-particle (α). Similarly, M_i is the atomic mass of the particles. Since α-decay typically occurs for heavy unstable nuclides, a large portion of the energy (≈99%) is distributed to the α-particle and the rest to the daughter nucleus. The energy that the daughter nucleus gets is a small portion, but not neglectable, since it is typically in the range of 100keV. This causes effects such as the recoil effect, which will be explained in a later section. Having a mass of approximately 4 atomic mass units and a charge of 2+ the α-particle falls in the category of heavy charged particles and is directly ionising radiation. The main interactions that α-particles have are electron excitation and ionisation. These interactions are types of energy transfer and slow down the α-particle of which the degree of slowing down is given by the linear (S) or mass stopping power (S/ρ), which are defined as:

$$ S = -\frac{dE}{dx}\left[\frac{MeV}{cm}\right] \qquad\qquad \frac{S}{\rho} = -\frac{1}{\rho}\frac{dE}{dx}\left[\frac{MeV\ cm^2}{g}\right], \tag{2.3} $$

where ρ is the density of the matter which is traversed and dE/dx is the lost energy (dE) for a small distance (dx). Fundamentally, the stopping power for charged particles is given by the Bethe-Bloch equation, which is in simplified form:

$$ S = -\frac{dE}{dx} = \frac{4\pi e^4 z^2}{m_0 v^2} NB \qquad\qquad B = Z\left[ln\left(\frac{2m_0 v^2}{I}\right) - ln\left(1 - \frac{v^2}{c^2}\right) - \frac{v^2}{c^2}\right], \tag{2.4} $$

[1] This is often not displayed in equation 2.1 due to total conservation of charge.

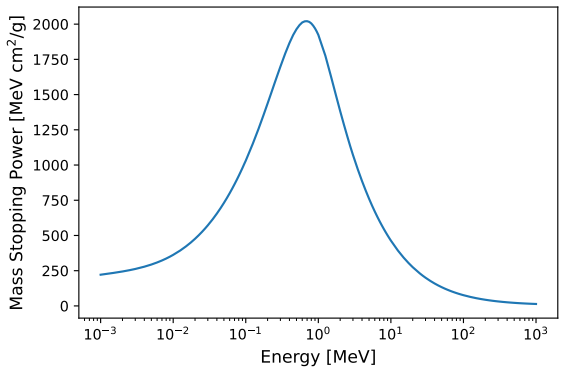

Figure 2.1: A graph showing the mass stopping powers for different energies for an α-particle in air. The stopping power is very low for high energies and increases for lower energies. The data was retrieved from NIST [21].

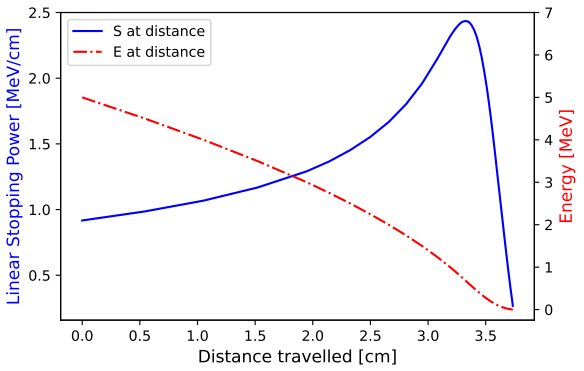

Figure 2.2: A graph showing the linear stopping power and energy for a 5MeV α-particle travelling through air. Both are given for a certain distance travelled. This kind of graph is also called a Bragg curve. The data was retrieved from NIST [21].

where e is the electron charge, z is the charge of the particle, m_0 is the electron rest mass, v is the velocity of the particle, N is the atomic density of the material, Z is the atomic number of the material, I is the average excitation and ionisation potential of the material and c is the speed of light in vacuum [18][19]. All these parameters, therefore, influence the way a charged particle loses energy in a medium. The main takeaways are that the stopping power increases significantly when a charged particle slows down (v^{-2} dominant term) and that the stopping power is proportional to the traversed medium's density and atomic number, thus electron density. The formula describes a simplified situation, stopping power is often simulated using SRIM or found in databases such as NIST, which will often be used in this research [20][21]. The stopping power of an α-particle for different energies is shown in Figure 2.1. Figure 2.2 shows the stopping power and energy of a 5MeV alpha particle in its path through the air, the first is also called the Bragg curve [22][23].

In these figures, the range and energy deposition behaviour of an α-particle or any other heavy charged particle is clearly characterised. The stopping power is relatively low for high-energy particles and increases very rapidly for lower energies, which is called the Bragg peak. This is caused by the particle moving slowly and thus being influenced more by the electrons of the material [19]. This property of a very well-defined point of large energy deposition, which is a general property for all heavy charged particles, will later be discussed in some more detail. What can also be seen from the Bragg curve is that the particles have a maximum range. The slowing down of particles is a statistical process, but a maximum range can be extrapolated. As mentioned before is the stopping power related to the material properties and energy of the particle. For a 5MeV α-particle the range in air is 3.6cm and the range in water is 37.6µm [21]. α-particles have a very short range in solid matter, which makes the shielding of α-particles fairly simple. It is often said that α-particles are stopped by a piece of paper[2]. A dose from external α radiation is often not taken into account for radiation protection, due to the short range in air and the inability to penetrate the upper dead layer of the skin [25]. However, internal exposure to α radiation can be extremely harmful due to the high energy and short range. At the same time can these properties also be used for cancer treatment, which is what this research is about and will be explained in Section 2.2.1.

[2]It is a good rule of thumb for shielding α-particles, however, people should be cautious of falling into a habit that α-particles are always stopped by anything thin. A piece of paper might just stop an α-particle (thickness 50-100µm and projected range 32.15µm in 100% cellulose and ρ=1.200kg/m^3) [20][24]. However, when working on the micrometre scale there is a large probability that α-particles might not be stopped, for example with collimators. Therefore, this should always be checked.

2.2. Current treatment methods for mCRPC and Targeted Alpha Therapy

For the treatment of cancer, there are various methods. Even for the same type of cancer, multiple factors can influence the choice of approach. In this research, the focus is on treatment methods for Metastatic Castration-Resistant Prostate Cancer (mCRPC). Metastasised cancer is challenging to treat as it has spread to multiple difficult-to-reach locations and is hard to detect due to its microscopic size. Consequently, all current treatments for mCRPC are palliative and aimed at prolonging life. Unfortunately, the prognosis for survival is poor [26]. The classic approach for metastasised prostate cancer is hormone therapy, which aims to lower the amount of testosterone that the cancer relies on, in order to stop tumour growth or shrink them [27]. However, the cancer eventually becomes independent of testosterone, and hormone therapy starts to fail. It then becomes mCRPC. Other treatments that can be used in combination with hormone therapy or after hormone therapy are radiation therapy, surgery, chemotherapy, targeted drug therapy, or a combination of these. More interesting are the newly researched therapies. Immunotherapy is still being developed for prostate cancer. Immunotherapy relies on boosting T-cells or training them to kill cancer cells. Immunotherapy has been successful for other types of cancer, however, for prostate cancer, immunotherapy has not yet been successfully implemented [28]. Then there is Targeted Radiation Therapy. This therapy uses radionuclides bound to a tumour-specific vector to target cancer cells and radiates them from close by, as shown in Figure 2.3 [3]. The two used radiation types are β^- and α. β^--particles and α-particles have a short range of a few millimetres and micrometres, respectively [29]. A commonly used β^- emitter is ^{177}Lu. Treatment with ^{177}Lu is in clinical phase 3, which is being evaluated in hospitals internationally and has had promising results in studies with large numbers of patients [30]. The downside of using β^- is that cancer can get resistant to it due to its low Linear Energy Transfer (LET). The only alternative is then to use α-emitters, which is called Targeted Alpha Therapy (TAT).

2.2.1. Targeted Alpha Therapy

Targeted Alpha Therapy (TAT) is a relatively new form of cancer treatment, which has its first clinical studies just before the turn of the century [3]. TAT makes use of an α-particle emitting nuclide that is bound with a chelator to a tumour-specific vector. Using α-particles for cancer treatment has multiple advantages. α-particles have a very short range, typically 50-100µm (about 6 cell diameters), in which they deposit an enormous amount of energy (on average 100keV/µm) [3][31]. α-particles are therefore also called high LET radiation. Their high energy, typically few MeV's, and high LET causes DNA double-strand and DNA cluster breaks [4], making α-particles highly effective cell killers. α-particles are also able to kill cancer cells in any stage of the cell cycle and oxygenation level and cancer cells which are resistant to β^- or γ radiation.

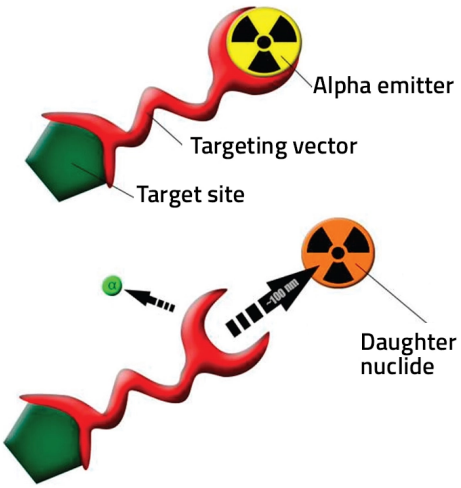

Figure 2.3: Schematic representation of a recoiling daughter radionuclide detaching from a targeting vector as a consequence of α decay [31].

There are many flavors of α-emitters, each with their own pros and cons. ^{225}Ac, ^{211}At, ^{212}Bi, ^{213}Bi, ^{212}Pb, ^{223}Ra, and ^{227}Th are clinically usable for TAT [3]. The potential cons include high cost, unresolved chemistry, limited availability, unfavourable half-life time, and weak binding to the chelator [10]. The most promising clinical results are from ^{225}Ac and its daughter ^{213}Bi [4]. The focus here is on ^{225}Ac, the most promising of the two. ^{225}Ac and its daughters emit a total of four α-particles, which increases cell-killing efficiency. It has a half-value time of 9.9 days, which makes it easy to handle and is enough time to bind to the tumour site [32]. The decay scheme of ^{225}Ac includes α, β^- and γ radiation, which will later be explained in more detail. ^{225}Ac is obtained by either radiochemical extraction from ^{229}Th or by use of an accelerator [4].

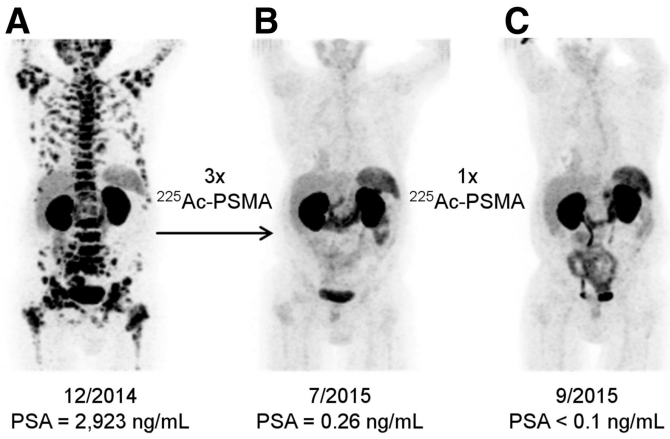

Figure 2.4: ^{68}Ga-PSMA-11 PET/CT scans of a patient, during multiple cycles of treatment with ^{225}Ac-PSMA-617 [33]. Black spots indicate where PSMA-617 accumulates.

2.2.2. Clinical results of Ac-225 Targeted Alpha Therapy

The use of ^{225}Ac bound to Prostate Specific Membrane Antigen 617 (^{225}Ac-PSMA-617) has had promising but mixed results when used to treat metastasised Castration-Resistant Prostate Cancer (mCRPC). In Figure 2.4 a case of mCRPC is shown. In the figure, the black parts are places where the PSMA-617 accumulates. PSMA-617 accumulates at tumour sites, the liver and the excretory system (kidneys) [33]. The patient, who did not respond to any other treatment like ^{177}Lu as mentioned earlier, had an impressive response, with the only side effect occurring during the study being Xerostomia (dry mouth syndrome). Other studies also found measurable anti-tumour effects [34][35][36]. Even though ^{225}Ac-PSMA-617 has had promising results of the extension of overall survival and for 10% a complete remission, PSMA-TAT has only just had its first clinical trials with a small number of patients [37]. Another study found less promising results, where 3 out of 15 patients did not see improvement, 7 patients died during the observation period, 5 requested to stop treatment due to Xerostomia and multiple side effects occurred [38]. Therefore, it is hard to make a good comparison and draw proper conclusions. A study from 2022 that did a meta-analysis drew the following conclusions [35]: Even though there are only a few reviews of ^{225}Ac-PSMA-617, results showed that there were significant therapeutic effects and low toxicity. All patients received a different treatment, like ^{177}Lu-PSMA-617, and failed. The treatment with ^{225}Ac-PSMA-617 after that showed better overall survival than the standard treatment. Quality of life also improved significantly for patients receiving ^{225}Ac-PSMA-617 treatment. There is still a standard empirical dose of 100kBq/kg and 1-8 cycles, which could be explored more. Overall, ^{225}Ac-PSMA-617 is an effective and safe treatment option, with low treatment-related side effects. However, the treatment is still in the clinical trial stage and the safety and efficacy needs to be further evaluated. Furthermore, long-term side effects are relatively unknown due to the short life expectancy of the patients involved in the clinical studies.

2.2.3. Decay chain of Ac-225

The decay chain of ^{225}Ac is given in Figure 2.5. ^{225}Ac has a relatively long half-life time, which is favourable for clinical use, though short enough such that treatment does not take too long. In its decay chain, ^{225}Ac will typically emit four α's and two β^-'s before it reaches the relatively stable ^{209}Bi. Emitting all these particles in a relatively short period makes ^{225}Ac very potent to kill cancer cells, however, due to the recoil effect, the daughters of ^{225}Ac might not remain at the tumour site leading to side effects discussed in the next subchapter. There are two decays where a potential γ can be emitted: ^{221}Fr 218keV (11.4%) and ^{213}Bi 440keV (25.9%). These γ's can be used to image the distribution of the daughters in-vivo by SPECT, however, the poor spatial resolution, a few millimetres, does not allow for imaging at cellular scale [3][39][40]. The emitted γ from ^{221}Fr can be used to determine the quality of the radio-pharmaceutical ^{225}Ac-PSMA-617 with γ chromatography as mentioned earlier.

^{225}Ac and the α emitting daughter nuclides reach secular equilibrium in a fairly short time, due to the short half-life time of the daughter nuclides. The ratio of daughter and parent is approximately 98% after six half-life times of the daughter nucleus. In a situation where initially no daughters are present ^{221}Fr and ^{217}At reach secular equilibrium with ^{225}Ac in 30 minutes and ^{213}Bi and ^{213}Po in 270 minutes. This can also be seen in Figures A.1 and A.2, where the activities of the nuclides are simulated. Therefore, when measuring the α spectrum of ^{225}Ac, typically four α peaks will be visible in equilibrium and the γ from ^{221}Fr can be used for quality control as it is close to the activity of ^{225}Ac after 30 minutes.

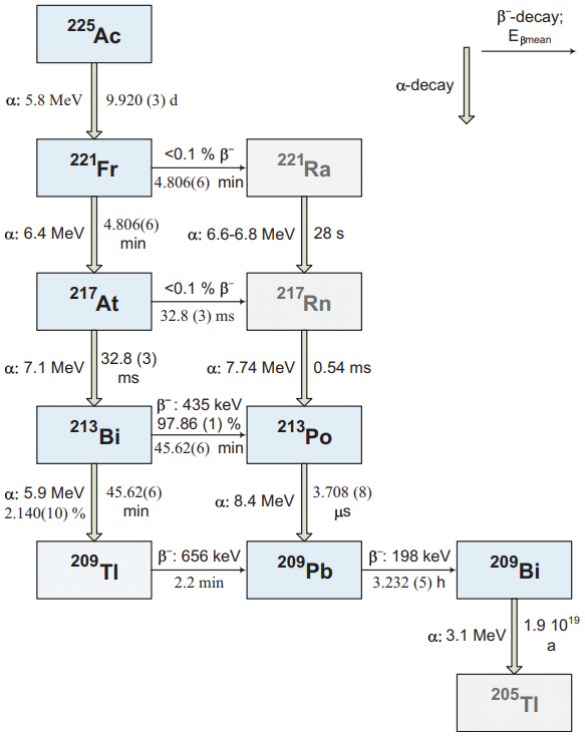

Figure 2.5: The decay chain of ^{225}Ac. Here decay type, mean or typical energy and half-life time is given per nuclide [41].

2.2.4. Recoil of the daughters

While treating mCRPC with ^{225}Ac-PSMA-617 has proven to be very promising, one of the difficulties is retaining the daughters of ^{225}Ac, which are also α-particle emitters. This problem arises due to the recoil effect, which occurs when ^{225}Ac or one of its daughters (^{221}Fr, ^{217}At, ^{213}Bi) decays with recoil energies of 104.8keV, 116.3keV, 132.8keV, and 112.0keV, respectively, breaking the chemical bond with the chelator, as also shown in Figure 2.3 [7][8]. The free radionuclides will not be able to target the tumour site anymore or could move away from the tumour. Not only does this effect cause the radionuclides to migrate to places other than the tumour, resulting in damage to healthy tissue, but it also reduces the cell-killing efficiency due to less α-particles being delivered to the tumour. This is a serious issue because α-particle emitters can cause side effects such as leukaemia and other malignant diseases [42]. Additionally, if ^{225}Ac is unable to deliver the four α-particles to the tumour, its advantage over ^{213}Bi TAT is lost [43]. While studies have confirmed the toxicity to healthy tissue due to the migration of free daughter nuclides, there have been no studies investigating the effect of recoil at the tumour site itself. Therefore, it is relatively unknown whether the daughters can diffuse away from the tumour site or if they remain there. Although simulations with SRIM indicate that the projected paths of the recoiling daughters (E ≈ 100keV) are on the order of 0.1µm, other mechanisms such as diffusion can cause the daughters to disperse away from the tumour site [20].

In order to reduce the toxicity to healthy tissue and improve retention at the tumour site, there are ways to improve the retention of the nuclides to the targeting vector. Methods to retain a higher amount of the daughter nuclides of ^{225}Ac have been promising, however, not perfect. There are different approaches to reduce the recoil effect: cell internalisation, local administration, or encapsulation in a nano-carrier [31]. A study found that when the cell has internalised the radionuclide compound, the recoiling nuclide is retained within the cell [43]. Improvement of cell internalisation has been successful, however, only at low doses. Local administration is only feasible for large and easy-to-access tumours. The most promising and often studied method is using nanoparticles. For example, liposome carriers with 31% retention of ^{213}Bi or $InPO_4$ nanoparticles with 40% retention of ^{213}Bi [44][32]. Achieving near 100% retention has not yet been demonstrated, and therefore decreasing the side effects of ^{225}Ac in TAT has not yet been successful.

2.3. Timepix3 detector

The detector that is going to be used for this research is the ADVAPIXTPX3 detector, made by ADVACAM, based on the Timepix3 chip. Timepix is a hybrid-pixel detector, developed by CERN [9]. It is called a hybrid detector since the detector is made out of two separate parts bonded together: the sensor (semiconductor) and the readout (microchip). This is also shown in Figure 2.6. In the semiconductor, radiation is converted into charge carriers, which are accelerated by the bias voltage to the pixel electrodes and converted into an observable signal in the microchip as is shown schematically in Figure 2.7 [10]. All Timepix readout chips contain 256x256 pixels with a size of 55µm x 55µm, resulting in a total surface of 1.98cm^2. Over the years different versions of Timepix have been developed all originating from the Medipix project. If required, multiple Timepix can be arranged in such a way that they form a 2x2 square, a line or behind each other, all for different purposes. The Timepix has three count modes, shown in Figure 2.8: counting mode, Time over Threshold (ToT) and Time of Arrival (ToA). ToT registers the time that the charge signal of a pixel is above a certain threshold, allowing the calculation of the energy. ToA registers the time that a charge is detected, allowing the determination of the direction of energy deposition. With the information of ToA and ToT α-, β^-- and γ-particles can be distinguished and spatial position and energy can be determined. The Timepix3 is capable of measuring ToT and ToA at the same time and is event-based, which means that as soon as a pixel measures a signal, it stores the data of that event. The ADVAPIXTPX3 is able to do 40Mhits/s/cm^2, which is 79.2Mhits/s for the whole detector surface [45]. The MINIPIXTPX3, a smaller version of the ADVAPIXTPX3, is able to do 2.35Mhits/s/cm^2, with the same sensor size. An estimated relative energy resolution of 5-10% for α-particle energies above 1.5MeV was found when calibrated with an ^{241}Am source [11]. The spatial resolution was determined to be up to 10µm [10].

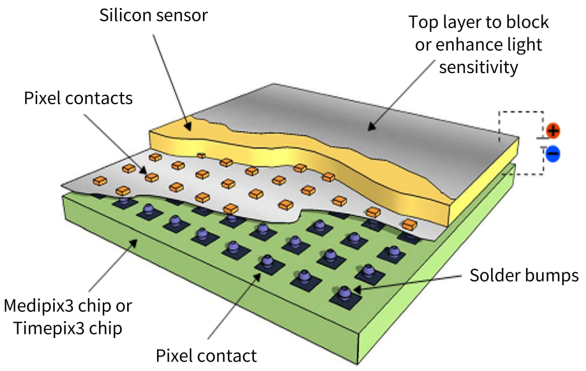

Figure 2.6: A 3D schematic overview of the Timepix detector [9]. Different components are labelled.

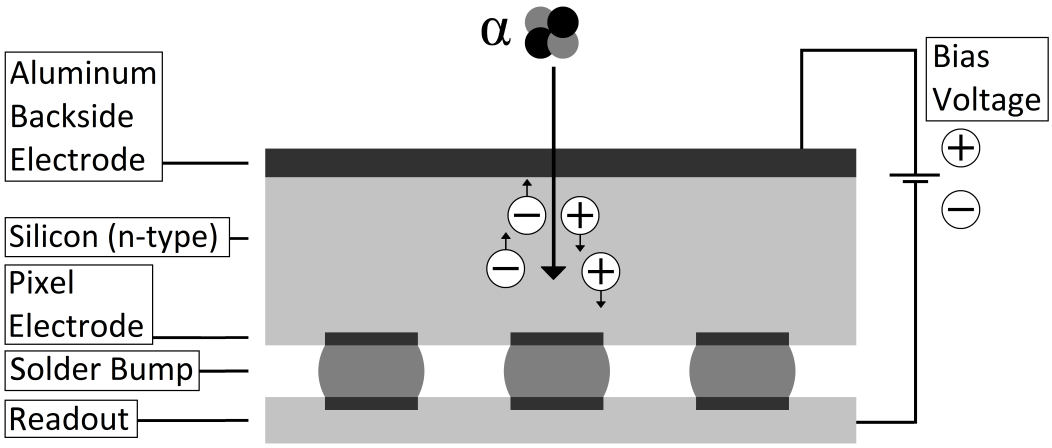

Figure 2.7: A 2D schematic overview of the Timepix3 components. Here an α-particle hits the semiconductor part of the detector and gets converted into charger carriers [46]. (Adapted from original)

2.3.1. Characteristics of radiation detection with the Timepix3

As radiation hits the silicon of the chip, it is converted into charge as shown in Figure 2.7. This induced charge is not always detected by a single pixel. Each radiation type and energy causes its own pattern on the chip, similar to a cloud chamber. This is caused by the charge sharing effect, where the released

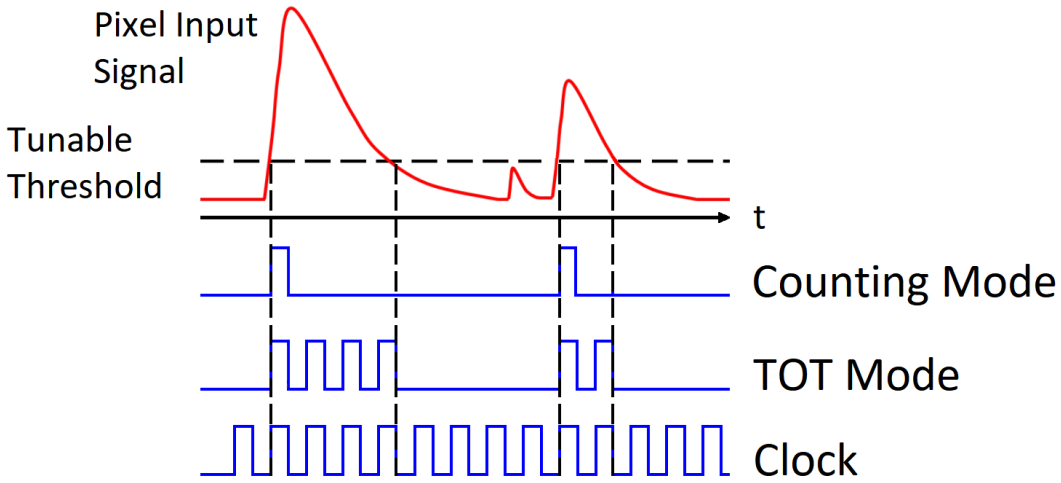

Figure 2.8: Different counting modes of the Timepix detector. The pixel input signal (top) is compared to a threshold and together with the clock gives an output signal, which is a count or a ToT value [47]. (Adapted from original)

charge diffuses into the neighbouring pixels, the way radiation interacts with the silicon and the angle of incidence [48][49][50]. Radiation is characterised in track patterns as shown in Figure 2.9. Generally, for each type of radiation, the size or length of the pattern increases with the energy of the incident radiation, as shown in Figure 2.10. These characteristic patterns allow for the determination of radiation types. However, similar patterns caused by different types of radiation can make it hard to distinguish between them. For example, a highly energetic electron can produce a curly track in such a way that it appears as a blob. This can be resolved by examining the ToT and ToA values of the pattern. Unfortunately, there is no way to determine with certainty if a small blob or dot is created by a photon or electron, or if a curly track is created by an energetic electron or a Compton-scattered electron from γ radiation since their patterns are the same. This limits the scope of usability of the detector. As this research focuses mainly on α-particles, it is important to define some characteristics of the heavy blob, also called a cluster. A cluster, adjacent pixels in a circular shape, has a height, which is the maximum value of the ToT of all pixels in the cluster, and has a volume, which is the sum of the ToT values of all pixels in the cluster and is related to the deposited energy.

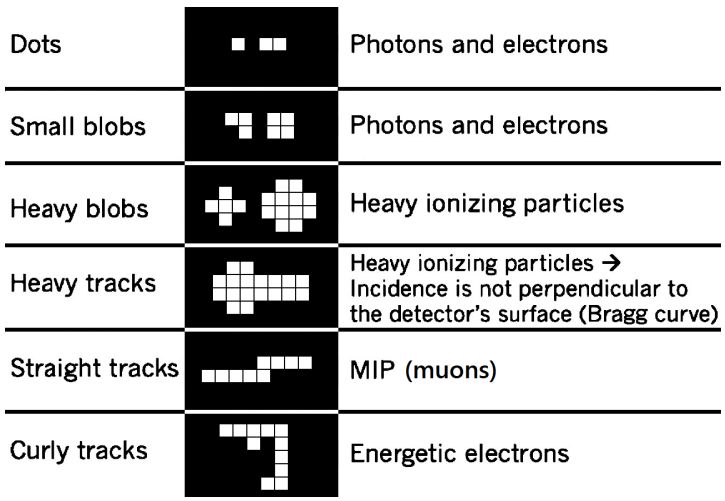

Figure 2.9: Schematic representation of the characterisation of radiation patterns from the Timepix. Each pattern, which is named on the left, is a result of a certain type of radiation, given on the right [51]. (Adapted from original)

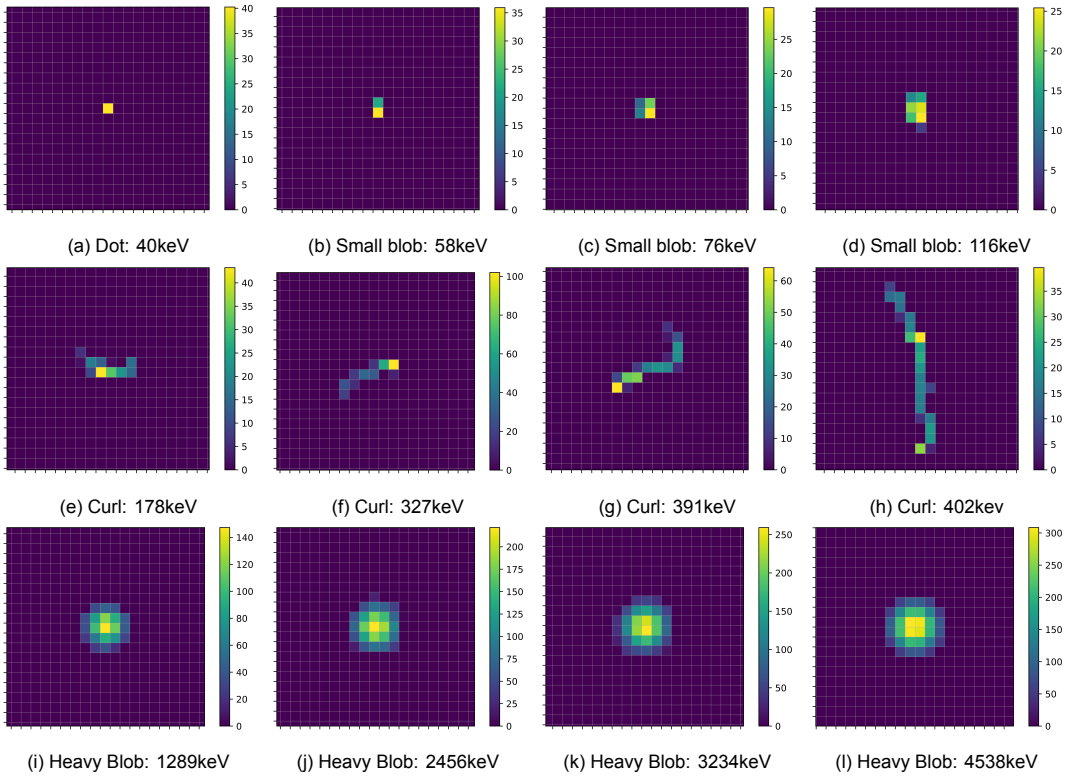

Figure 2.10: Radiation patterns categorised by type and energy. Each row contains the same type of pattern from top to bottom: Dot/Small blob, Curly track, Heavy blob. The dots, small blobs and curly tracks are created by the γ's and β^-'s from ^{225}Ac and its daughters, and the Heavy blobs are created by their α's. The energy is increasing from left to right and is given for each pattern (gamma calibrated, see Section 2.3.3). The patterns are chosen to illustrate the trend of the changing shape, but each pattern can look different or similar for different energies. The α's are collimated and have an incidence perpendicular to the detector surface. The bias voltage is set to 30V and the threshold is set to 2.01keV.

2.3.2. Timepix bias voltage

The response of the Timepix3 detector is non-linear for high-energy ranges, as illustrated in the following Section and Figure 2.13. Due to limitations of the Timepix electronics, the signal from a pixel receiving high energy (>850keV) can become distorted or decrease in intensity [52]. The output signal of the pixel preamplifier may become excessively high (negative), leading to undershooting caused by saturation. Consequently, the signal of the comparator, which compares the signal with the set threshold, temporarily drops to zero [53]. After a period of time, the undershoot dissipates, causing the comparator signal to rise back to a high level. This results in two brief Time over Threshold (ToT) signals, separated in time and much shorter in duration than the actual total ToT duration, as depicted in Figure 2.11.

This effect often occurs for highly energetic heavy ionising particles, such as protons, α-particles, and heavy ions. Due to their distinctive heavy blob pattern, which is a symmetric 2D Gaussian for 0° incidence as shown in Figure 2.10, only the central region becomes saturated and consequently underestimated. This phenomenon is known as the volcano effect, named after its similar shape [54][55]. The bias voltage can be adjusted to influence the diffusion and lateral spread of the charge, thereby affecting the shape and height of the blobs [53][56]. A lower bias voltage decreases the height and volume of the cluster while increasing its width. Figure 2.12 illustrates the changes in the clusters as the bias voltage is modified. As the bias voltage increases, the cluster becomes smaller but exhibits increased volume and height. Above a certain bias voltage, the volcano effect starts to occur due to the growing height of the cluster. With higher bias voltages, more pixels become over-saturated and underestimated, resulting in a void within the cluster. Therefore, a proper bias voltage is crucial when measuring heavy ionising particles. The appropriate bias voltage needs to be determined before conducting measurements. It should be noted that very low bias voltages may result in no response to very low-energy radiation (>8keV) [57]. However, this is not relevant to this research.

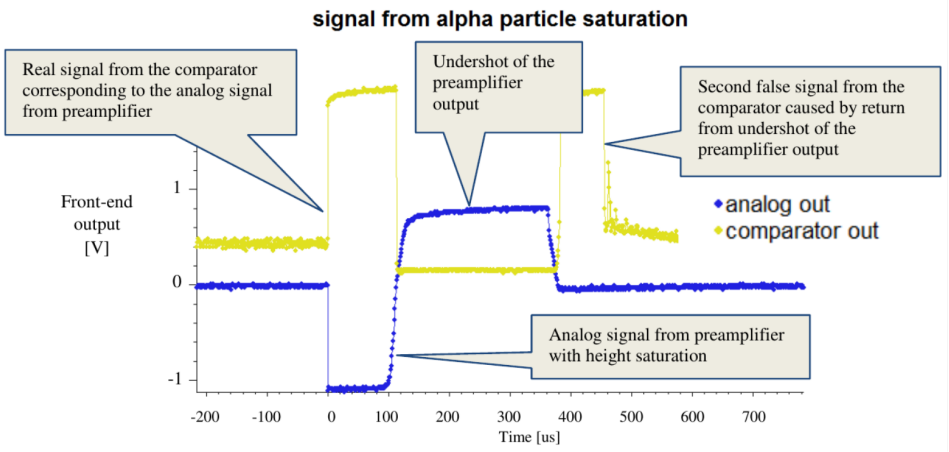

Figure 2.11: The demonstration of non-linear saturation. Due to the high incoming signal, the output from the preamplifier becomes saturated, causing it to undershoot. This first sets the comparator output to high (saturation), then to low (undershot). On the return from the undershot to zero, the comparator output becomes high once more, resulting in two short ToT pulses [53].

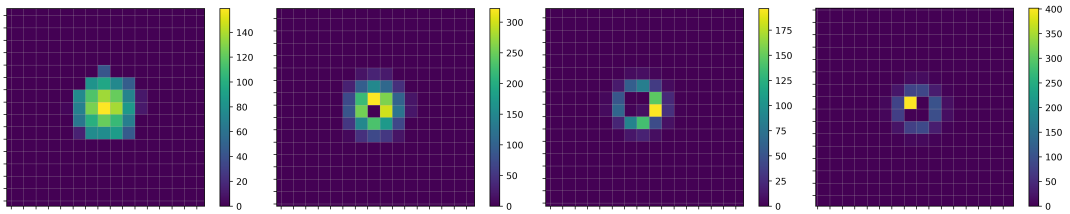

(a) Bias: 15V (b) Bias: 45V (c) Bias: 90V (d) Bias: 200V

Figure 2.12: Uncollimated α-particles from ^{225}Ac and its daughters for different bias voltages. The colour scale is for ToT per pixel (uncalibrated). The patterns are chosen to illustrate the trend of increasing volcano effect. The threshold is set to 2.01keV.

2.3.3. Timepix calibration

2.3.3.1 Gamma calibration

The Timepix gives information about the deposited energy in ToT values. This is the time that the input signal of the pixel is above a set threshold value, thus it is an indirect measurement of energy. Calibration is needed in order to convert ToT values to particle energy. The pixel response to deposited energy is not linear but segmented in different regions, as shown in Figure 2.13. For low energies (E/pixel<15keV) the response is non-linear. The response is then linear for 15keV<E/pixel<850keV. After this, the distorted region and the saturated (volcano) region occur. These regions usually occur for high-energy ions. Since the highest energy alpha in this research, from ^{213}Po, has an energy of 8.4Mev, deposited in about 20-30 pixels at 30V bias voltage, only the linear part of the normal regular region is considered (15-850)keV/px.

No pixel response can be the same since each pixel is individually read out, amplified and processed, which results in a different ToT value for each pixel for the same radiation [58]. This variation is demonstrated in Figure 2.14. The figure shows the single-hit responses from the 14.41keV γ emitted by ^{57}Co and the low energy γ and X-rays from ^{241}Am for two sets of individual pixel responses and all the pixels combined [5]. Clearly, the peaks are at different positions, resulting in a washed-out response for the whole detector, reducing energy resolution. This washing-out is also clearly demonstrated in the spectrum of ^{241}Am, where γ peaks cannot be distinguished if the response of the whole uncalibrated detector is taken. Therefore a per-pixel calibration is needed, which can be done in a few ways:

1. γ or X-ray Radiation: An external radiation source is used, a low-energy γ or X-ray emitter, in order to get single pixel hits [52]. The response of the pixel (ToT) is then converted to an energy value. When this is done with at least 2 energies a calibration graph can be made. This is the

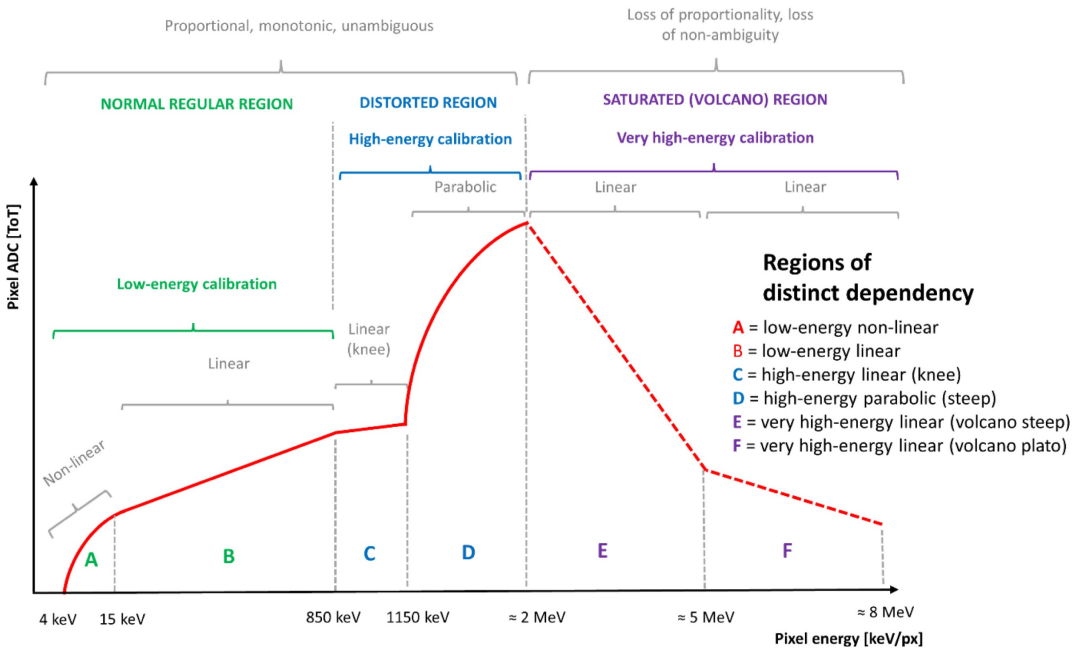

Figure 2.13: Pixel responses for deposited energies, showing different types of responses [56]. For low energies, the response is initially non-linear, becomes linear and bends at higher energies. Above 1150keV/pixel the energy response becomes distorted.

most precise method, though time-consuming [53].

2. Internal/External test pulses:

   (a) Internal: Each pixel has an analog test structure to test its capacitance [58]. A variable voltage pulse can be injected into the pixel from the readout hardware to simulate charge deposition by radiation.

   (b) External: This is similar to the internal test pulse, but now an external voltage is applied to the bias voltage, generating a charge on the capacitors of the pixels.

   These methods are faster than calibration with radiation, though less precise. They also do not require a radiation source.

3. Common electrode signal: This method uses α emitters with well defined energy [59]. Instead of looking at single pixels, a signal is read out from the common backside electrode, representing the absolute energy deposited, and related to the individual pixel responses in the cluster. In order to read out the common backside electrode, a different readout interface needs to be used, the FITPix COMBO.

While it depends on the manufacturer of the Timepix, the Timepix3 from ADVACAM is already calibrated per pixel [60]. This is done with an ^{241}Am source (γ: 59.5keV) in combination with K_α X-ray fluorescence of Fe, Cu, Zr, Cd, or In [5]. This calibration is done with a bias voltage of 200V. Therefore, it is possible to use the Timepix immediately for low-energy radiation. However, as mentioned before, a different bias voltage setting is required for the spectroscopy of α-particles, so a new calibration on the chosen bias voltage needs to be performed.

For this research, calibration with a γ source is chosen since these sources were available and provided the most precise calibration, which is favourable considering that the four α energies need to be distinguished requiring an energy resolution as high as possible. The other methods were also not available in the provided software from ADVACAM, since their internal research concluded that X-ray calibration was the best option [61]. This method relies on calibrating the pixels with known energy radiation causing a single pixel hit on the detector. A single pixel hit is required for calibration since

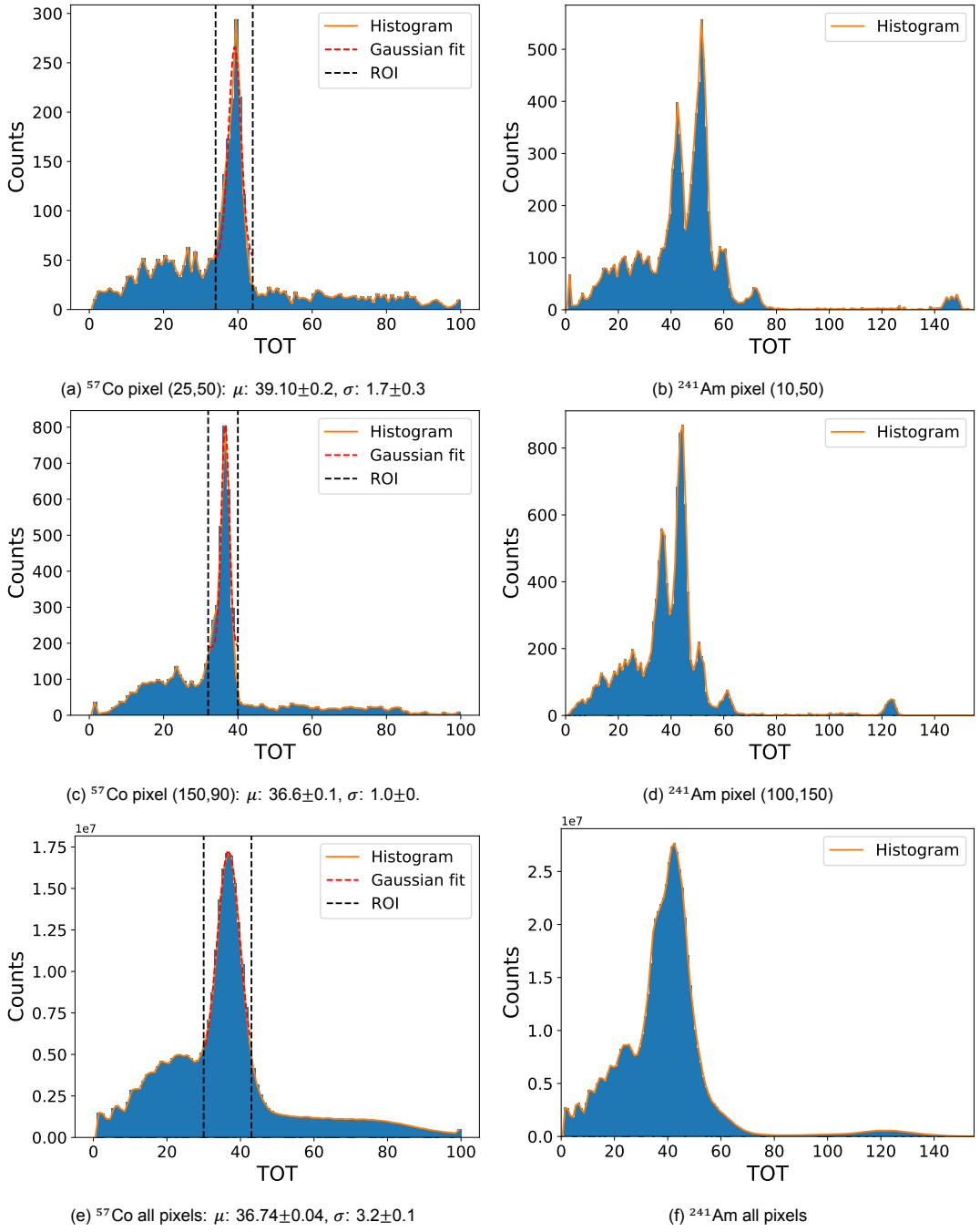

(a) ^{57}Co pixel (25,50): μ: 39.10±0.2, σ: 1.7±0.3

(b) ^{241}Am pixel (10,50)

(c) ^{57}Co pixel (150,90): μ: 36.6±0.1, σ: 1.0±0.

(d) ^{241}Am pixel (100,150)

(e) ^{57}Co all pixels: μ: 36.74±0.04, σ: 3.2±0.1

(f) ^{241}Am all pixels

Figure 2.14: The single pixel hit response of the Timepix3 detector to the decay radiation of ^{57}Co (left) and ^{241}Am (right). This is done for the response of all pixels and 2 sets of individual pixel responses. On the spectrum of ^{57}Co a Gaussian is fitted within a certain region of interest to determine the average ToT response of the 14.41keV γ peak and to indicate the displacement and loss of resolution. The bias voltage is set to 30V and the threshold to 2.01keV.

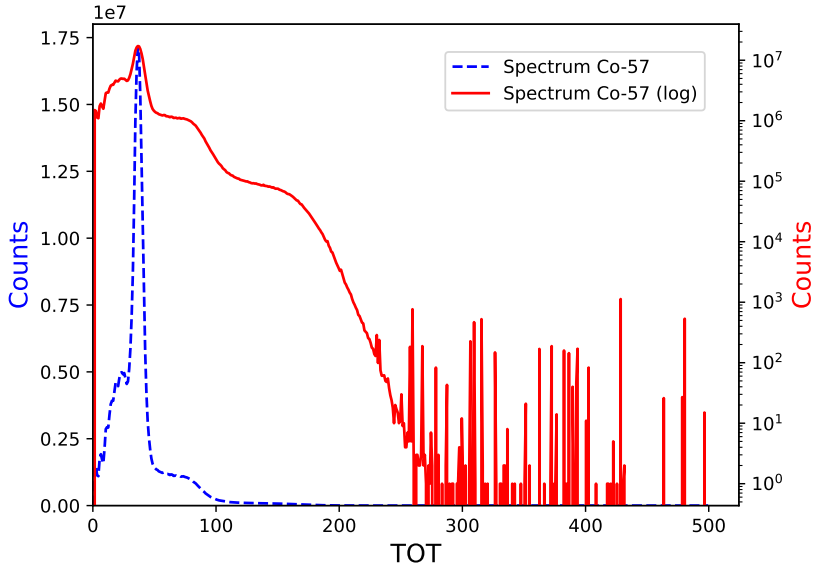

Figure 2.15: Single pixel hit responses of ^{57}Co on a normal and logarithmic scale. The bias voltage is set to 30V and the threshold is set to 2.01keV.

only then is it possible to retrieve information about the response of a single pixel. The response of the pixels relies on the incoming radiation as each has its own energy deposition pattern on the chip as explained in Section 2.3.1. Only γ radiation and very low energy β radiation are able to produce single-pixel hits. However, β-particles do not have well-defined energies at the surface of the detector due to slowing down. Therefore, only γ radiation is a suitable option. When choosing a radionuclide to calibrate, it should be kept in mind that the emitted radiation should be distinguishable in energy and the response pattern on the detector. The nuclide should therefore not emit γ and β radiation in the same energy range or the β-particles should be shielded. Often chosen nuclides are ^{241}Am together with Fe, Cu, Zr, Cd, or In X-ray fluorescence, ^{57}Co, ^{109}Cd or ^{55}Fe for low energy non-linear calibration [52][48][60][47][56]. A monochromatic synchrotron beam could also be used. The energy of the emitted γ radiation should not be too high, since that would produce fewer single pixel hits due to the charge sharing effect [48]. The 59.54keV γ of ^{241}Am is considered as the practical maximum for calibration [53]. It is possible, however, to use larger energies, though the chance of single-pixel hits decreases. In Figure 2.15 the single pixel response is shown when measuring γ's of ^{57}Co (14.41keV, 122.06keV and 136.47keV). From the Figure, it is evident that the highest two γ energies (122.06keV and 136.47keV) do not give a clear spectrum with single-pixel hits. Single-pixel hits also have a small charge-sharing effect to the neighbouring pixels, which will not register as a hit if they are below the set threshold value. This could lead to an underestimation of the energy. However, as shown in Figure 2.16, the single-pixel hit response is very close to the true value and larger cluster sizes overestimate the true energy. Therefore, together with the fact that the response is linear in this region, the calibration by using single-pixel hits can be extrapolated to higher energy alpha clusters and be accurate.

2.3.3.2 Alpha calibration

In the previous Section γ calibration was mentioned to improve energy resolution and uniformity of the detector surface. Even though this should be enough, there is another calibration method that can be used to improve resolution at higher energies. This type of calibration is done with α-particles. Normally, calibration with heavy charged particles is done to correct for the distorted region or the saturated volcano region (see Figure 2.13), however, in this case, a correction to improve the calibration at the end of the linear region is required [56][55]. This type of calibration is not a per-pixel calibration since α-particles create a blob pattern, as energy is shared or leaked to neighbouring pixels. Therefore, this method is an estimation and still relies on an initial per-pixel calibration performed with γ's and is used to correct errors. In this case, α-particles are measured from an α source and processed. You could

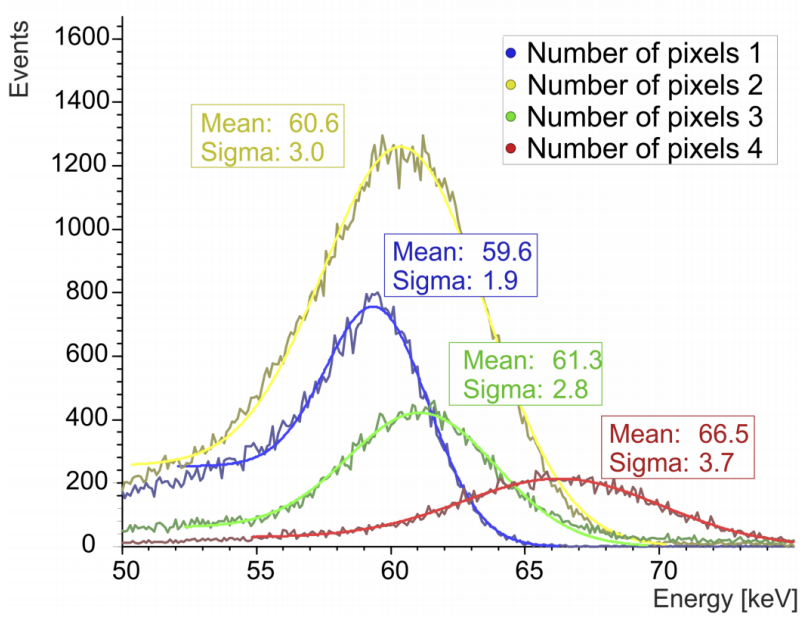

Figure 2.16: Responses for different cluster sizes of the 59.54keV γ photon of a ^{241}Am source measured with the Timepix after γ calibration [48].

calculate the total energy of a measured α-particle and store this information in the pixel coinciding with the centre of mass. The average value of all these measured energies would then be defined as the response of that pixel to the certain α-particle energy coinciding with that pixel. The response, or better said the deviation from the average response of the chip, is used to calculate a correcting factor. However, the blob contains information about multiple pixels. Therefore, it could be possible to define the average blob shape by measuring the α-particles on the whole chip. This blob shape, which is a 2D Gaussian shape is also seen in Figure 2.9 [62]. The average blob shape can be defined as a weighting factor. As an α-particle is processed, its energy is calculated and saved in all the surrounding pixels with a weighting factor which is determined by the average blob shape. You could go further by defining a weighting factor by determining the shape for each measured α-particle, however, this could lead to errors and increase processing time.

2.4. Data analysis

For this research, the chosen output data type for the Timepix is the .t3pa type. In this type, each event (pixel is over the threshold value) is appended as a row. The columns are defined in Table 2.1. Since all events are separate pixels and energy is given indirectly, a code that analyses the data is required to determine the particle type, location and energy. In Algorithm 1, the general data analysis algorithm is given, which is also given in Section A.5 as Python code. This code was extended to utilise multiprocessing in order to speed up the code. The output of the analysis code then contains the following information about each detected particle: type, (calibrated) energy and detected position.

Table 2.1: Data structure of the .t3pa file output of the Timepix [57].

Column	Header	Description
1	Index	Indicates event number
2	Matrix Index	Gives information about the (x,y) coordinates of the pixel: (x = Matrix Index%256, y = Matrix Index//256)
3	ToA	Gives the Time of Arrival. To calculate time in ns: Time (ns) = TOA*25 - FToA*1.5625
4	ToT	Gives the Time over Threshold. Which is the duration of a signal above the threshold.
5	FToA	Fast Time of Arrival. Improves time resolution, as explained in column 3
6	Overflow	Indicates data overflow if the maximum hit rate is exceeded.

Algorithm 1 A global overview of the analysis of the Timepix3 data output. This algorithm clusters pixels into particles and determines if they are: heavy blobs, curly tracks or small blobs, or dots. After converting ToT to energy with a provided calibration, it stores the particle's energy-weighted location, energy and type.

```
Load data-file (.t3pa), calibration data and dead pixel data
Convert Matrix Index to coordinates
Define index matrix and define borders
Create arrays to hold and save processed data
Split the data based on large time differences in ToA data (Comment: There might still be multiple particles within a time frame, this is fixed later by labelling)
for Particles in split data set do
    Save ToA and ToT info on 2 (256,256) arrays
    Split particles by labelling adjacent pixels
    for Particle in Particles do
        Convert ToT into energy by using γ calibration data
        Check if none of the pixels are dead by using dead pixel data
        Calculate energy and ToA values around COM
        if Particle is round and surrounding energy is sufficiently high and ToA is highest for the COM and the particle does not coincide with the borders and cluster size is sufficiently large then
            Correct α energy based on α calibration
            Save energy and COM coordinates as α-particle
        else if If the particle is larger than one pixel and particle does not coincide with the borders then
            Save energy and COM coordinates as β-/γ-particle
        else if If the particle is a single pixel then
            Save energy and COM coordinates as single-hit particle
        end if
    end for
end for
Save data
```

2.5. Spatial and energy resolution

2.5.1. Collimators

The Timepix is able to give information about the type, energy, position and sometimes even direction of incoming radiation. However, to fully optimise the energy and spatial resolution a suitable collimator needs to be chosen with the trade-off in mind that the efficiency drastically reduces. This is, of course, different for each case of use. The concept of a collimator will now be explained in more detail.

A collimator is essentially an object that creates a narrow parallel beam from incoming radiation. It is usually a slab of material with holes in it, such that radiation not travelling in a parallel direction will be absorbed by the material and radiation that is travelling through a hole and parallel to its direction will be transmitted, as shown in Figure 2.17. Collimators can have different geometries based on the application and radiation source. The most commonly used types of collimators are parallel hole (Figure 2.17), converging hole, diverging hole and pinhole collimators [63]. This research focuses on parallel hole collimators since the detector and sample are plate/slab geometries. The spatial and energy resolution of the collimator is determined by the length (L) and width (D) of the holes, the wall thickness and its attenuation, and the distance between the radiation source and the collimator (B) [64]. The effect of the L/D ratio and B is shown in Figure 2.18. A larger L results in a higher spatial resolution and a larger D results in a lower spatial resolution. It is clear that the for the reverse, the effect on the resolution is also reversed. Since they both influence the resolution in an equal manner, the L and D parameters are often expressed as a ratio. Increasing both L and D, such that L/D stays the same, will not affect the resolution. As B increases, the angle of detectable radiation reduces and radiation is able to go through more different holes, reducing the spatial resolution. If the walls of the collimator are not thick enough or have a low attenuation coefficient, radiation is able to penetrate the collimator walls and be detected at a different position, also reducing the spatial resolution.

Not only does a collimator increase the spatial resolution, but in the case of charged particles it also increases energy resolution, by making the travelled paths of the radiation more uniform. The effect of the parameters on the energy resolution is quite similar to spatial resolution, since limiting the angle of detected radiation also limits the deviation in the travelled path and thus energy lost. However, the effect on the resolution by the wall width is now doubled, since not only does the radiation travel a longer path due to the path through a wall, but its energy is also attenuated by the wall. Therefore it is important to check that the amount of radiation still detected with a path through a wall is sufficiently low.

As mentioned before increasing L and decreasing D would give a higher resolution, however, it should be kept in mind that there are practical limits for L and D. Especially the effectiveness, the amount of radiation detected by the whole system, drastically reduces for larger L and smaller D since the angle of transmitted radiation reduces. It is not favourable for the resolution to reduce the wall width to a width where a large portion of the radiation is still transmitted if it goes through the wall. This also sets a practical limit to the parameter D, as smaller D than wall width limits the view of the object.

The holes of the collimator can have different shapes, as shown in Figure 2.19. The geometry of the holes determines the effectiveness of the collimator and influences the uniformity of resolution [65]. The round holes are most uniform in energy resolution, however, due to the thicker walls, effectiveness is lost. The most commonly used collimator is the hexagonal collimator, which has better effectiveness at the cost of loss of energy resolution uniformity. The square hole collimator also has better effectiveness but the uniformity deviates quite a lot by at most a factor $\sqrt{2}$. Uniformity in energy resolution is also determined by the quality of fabrication since deviation in holes changes the energy resolution.

2.6. Determination of spatial and energy resolution

For γ spectroscopy, the width of the photo-peak determines the resolution of the detector [65]. A photo-peak can be described by a Gaussian function, which is defined as

$$f(x) = A\exp\left(-\frac{(x-B)^2}{2C^2}\right) = A\exp\left(-\frac{(x-\mu)^2}{2\sigma^2}\right), \tag{2.5}$$

with $A, B, C \in \mathbb{R}$ and $C > 0$. Here A denotes the height of the curve peak, B denotes the position of

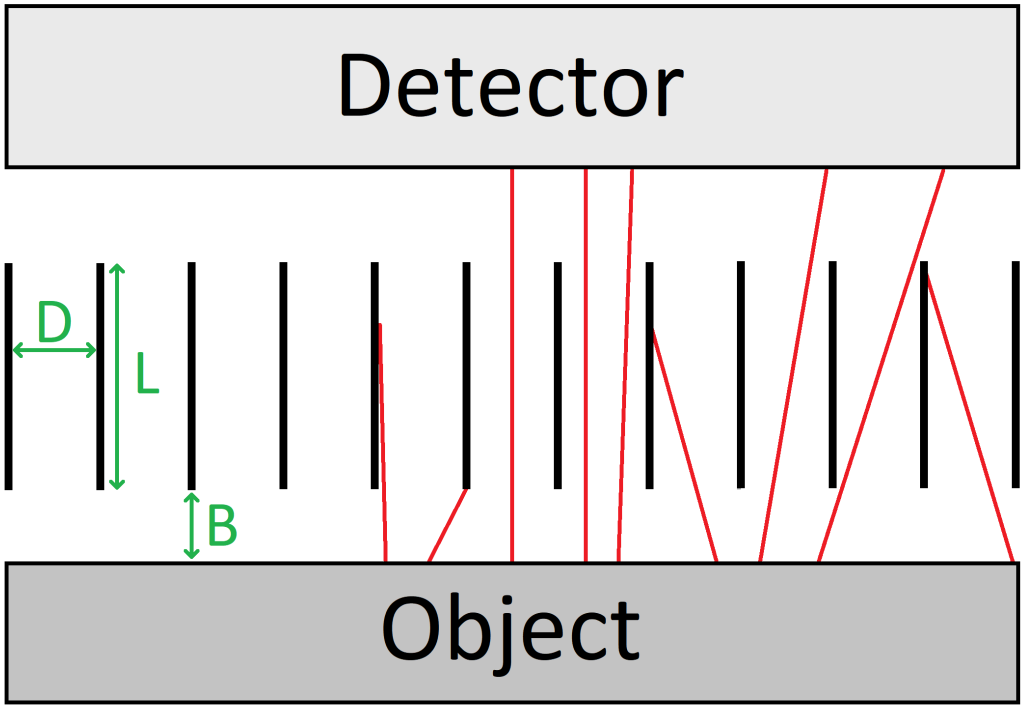

Figure 2.17: A schematic view of a parallel hole collimator, between an object and a detector. The red lines originating from the object are emitted radiation. The radiation that hits one of the collimator walls is absorbed (idealised) and the rest is transmitted and reaches the detector. The effect of the collimator is that the paths of the transmitted radiation are more parallel and that the travelled path length is more uniform. The geometry of detectors is typically given by the parameters L (length) and D (diameter) or its ratio L/D and B (object to collimator distance).

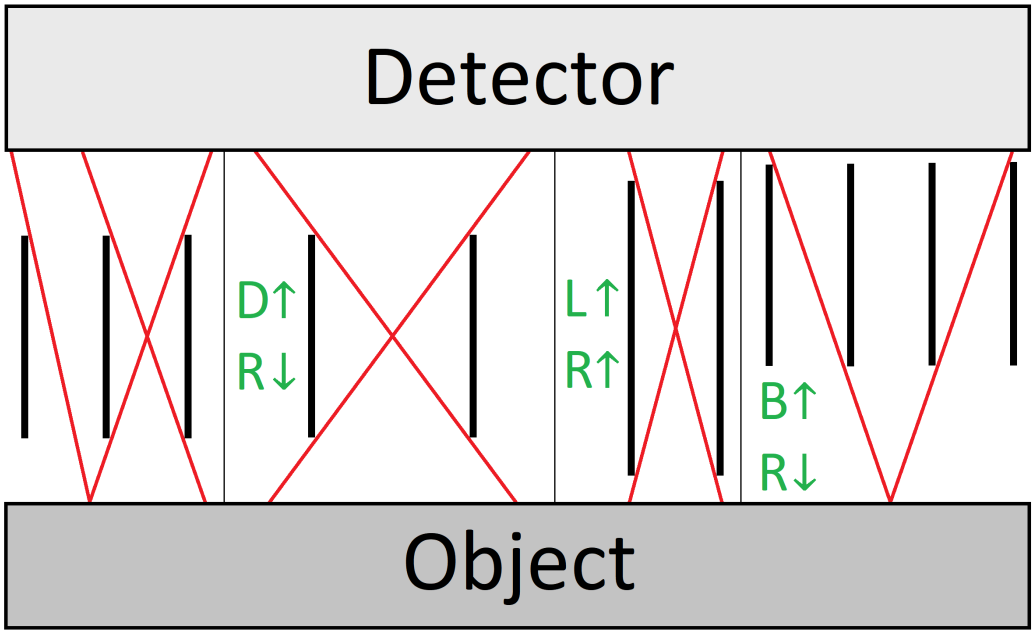

Figure 2.18: The effect of the L, D and B parameters on the spatial resolution of the collimator. The deviation between the horizontal emission position and detection position determines the resolution. The beam becomes wider for larger D, thus reducing the spatial resolution, and more narrow for larger L, thus increasing the spatial resolution. As B increases, radiation is able to go through more holes, reducing the spatial resolution.

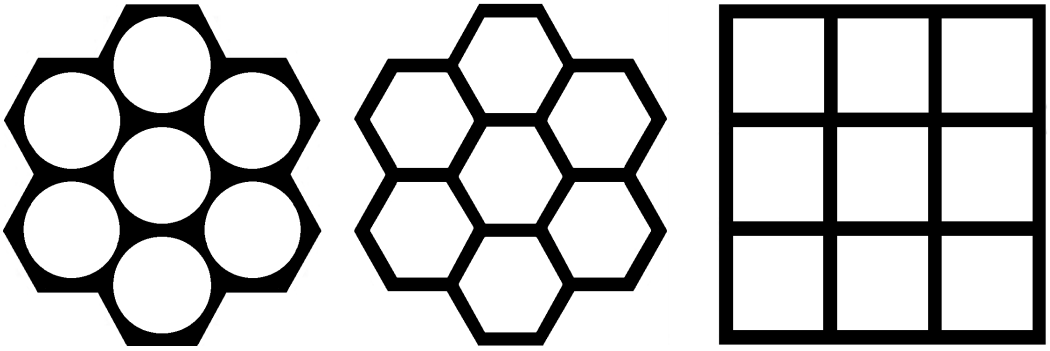

Figure 2.19: Different types of hole shapes for collimators. From left to right: round, hexagonal and square [65].

the curve peak and C denotes the spread or width of the curve. As the Gaussian is commonly used in statistics, the last two coefficients are also often denoted as μ (average) and σ (standard deviation), respectively. The width determines the resolution but more specifically is it expressed as

$$R_E = \frac{FWHM}{E} \cdot 100\%, \tag{2.6}$$

where FWHM is the Full Width at Half Maximum (of the Gaussian) and E is the Energy of the peak [65]. This equation can be expressed differently by using the following steps. First, both the x positions at half maximum (x_{HM}) can be found in the following way:

$$\begin{aligned} f(x_{HM}) = A\exp\left(-\frac{(x_{HM}-\mu)^2}{2\sigma^2}\right) = 0.5A, \\ ln(2) = \frac{(x_{HM}-\mu)^2}{2\sigma^2}, \\ x_{HM}^{\pm} = \mu \pm \sqrt{2\sigma^2 \ln 2} = \mu \pm \sigma\sqrt{2\ln(2)}. \end{aligned} \tag{2.7}$$

Then the FWHM is the distance between the two positions:

$$FWHM = x^+ - x^- = 2\sigma\sqrt{2\ln(2)} \approx 2.355\sigma. \tag{2.8}$$

Using the new definition of the FWHM and the fact that E in equation 2.6 can also be written as μ, the equation rewrites to[3]:

$$R_E = \frac{2.355\sigma}{\mu} \cdot 100\%. \tag{2.9}$$

The error is then given by:

$$\delta R_E = R_E \sqrt{(\frac{\delta\sigma}{\sigma})^2 + (\frac{\delta\mu}{\mu})^2}. \tag{2.10}$$

This principle of energy resolution can also be extended to α spectroscopy [66]. The previously named parameters and an example calculation of the energy resolution are also shown in Figure 2.20, where a Gaussian (more specifically a Normal Distribution) is plotted together with annotation for the FWHM.

[3] Only valid for a symmetric Gaussian.

Common ways to characterise the spatial resolution of a detector is by using a Point Spread Function (PSF) using a point source or a Line Spread Function (LSF) using a line source [65]. Both are measurements of how the signal is spread out over the detector and both are Gaussian in shape. However, a point or line source can not be created in all circumstances. An alternative way to derive the LSF is by using an Edge Spread Function (ESF) or sometimes also called a Spatial Frequency Response (SFR) of which the LSF is the derivative [67][68]. The ESF can be measured by using a well-defined edge on a radiation source to create a sharp discontinuity by blocking radiation. Then, by taking the derivative of the resulting ESF, the LSF can be obtained. This method is much simpler and gives a similar result. The spatial resolution is then given by the FWHM of the LSF. An example shape of the ESF (integral of Gaussian) and LSF (Gaussian) is also given in Figure 2.20.

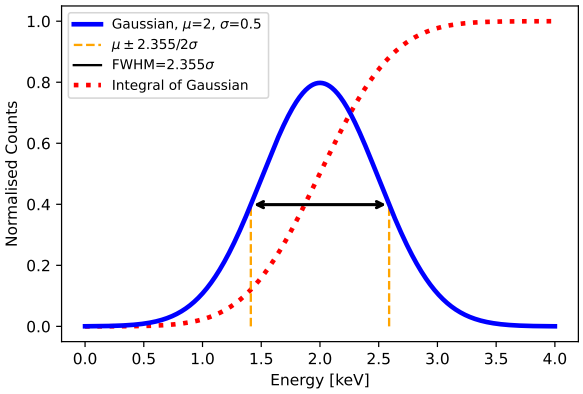

Figure 2.20: A normal distribution with parameters μ=2 and σ=0.5 is plotted to mimic an energy spectrum with an energy peak of E=2keV and σ=0.5keV. Here the edges of the FWHM are indicated with a dotted line and the FWHM is indicated with a double-sided arrow. In this case, the energy resolution would be 2.355*σ/E≈60%. The dotted line is the integral of the Gaussian, used for spatial resolution.

2.7. Background of related projects

Besides trying to use the Timepix to get information about the distribution of ^{225}Ac and its daughters, the Timepix was also used for other small research projects. This last part will be devoted to the background information on these projects.

2.7.1. Quality control of 225-Ac-PSMA-617

For the treatment of mCRPC with ^{225}Ac-PSMA-617 the PSMA-617, a molecule that links to the antigens found in this specific type of cancer cells, first needs to be labelled with ^{225}Ac. This is done with a commonly used chelator, called Dodecane Tetraacetic Acid (DOTA) [33]. This labelling needs to be of a high yield, otherwise a large amount of unbound ^{225}Ac (and daughters) is injected into the patient, unable to target the tumour thus delivering an unwanted dose to healthy tissue. This quality is defined as the Radio-Chemical Purity (RCP), which is the ratio between the desired radio-pharmaceutical (labelled ^{255}Ac and daughters) and the rest (unlabelled radionuclides) [69]. The determination of the RCP is done with Radio Thin Layer Chromatography (Radio-TLC) or High-Performance Liquid Chromatography (HPLC) [13]. Both methods rely on separating compounds, called the stationary phase, based on the varying affinity of the compounds with a solution passing through the stationary phase called the mobile phase. The goal is then to separate the radio-labelled compounds from the free radionuclides and measure the activity of both. Currently, for these methods, only γ's are measured, which means in this case that the γ's from ^{221}Fr are measured. However, this requires equilibrium to be established, which is after 30 minutes or longer and is still an indirect measurement of ^{225}Ac[4]. The Timepix is able to do a direct measurement of all emitted particles and if the resolution is sufficient they can also be distinguished. It can then be used to measure the sample without delay to save valuable time. Using the Timepix could also give an insight into the amount of a certain nuclide in a fraction or on a position since it is not fully known if there is a separation between the differently radio-labelled compounds or that the chelator has a different affinity to ^{225}Ac or its daughters [70]. These concepts can now be better understood with a direct measurement method and a small experiment is devoted to this.

2.7.2. Proton therapy

Proton therapy is a relatively new method to treat cancer. It has been proven to be effective and safe, though at a higher cost [71]. The advantages over current methods are case-dependent and it has not yet been demonstrated to be the best option overall. However, there is still a lot of research being

[4]This is after approximately 6 half-life times of the daughter (^{221}Fr), also seen in Appendix A.1

done in this field to improve this therapy. The therapy makes use of high-energy protons, which are accelerated by a cyclotron to an energy of around 250MeV [72]. This energy is often modulated to lower energies in order to change the range of the protons in tissue. The main advantage of using protons is that protons, which are heavy charged particles, have a very well-defined range and deposit a large amount of their energy at the end of this range. This is the same mechanism as explained for α-particles in Section 2.1. A graph showing the relative delivered dose of protons compared to photons is shown in Figure 2.21.

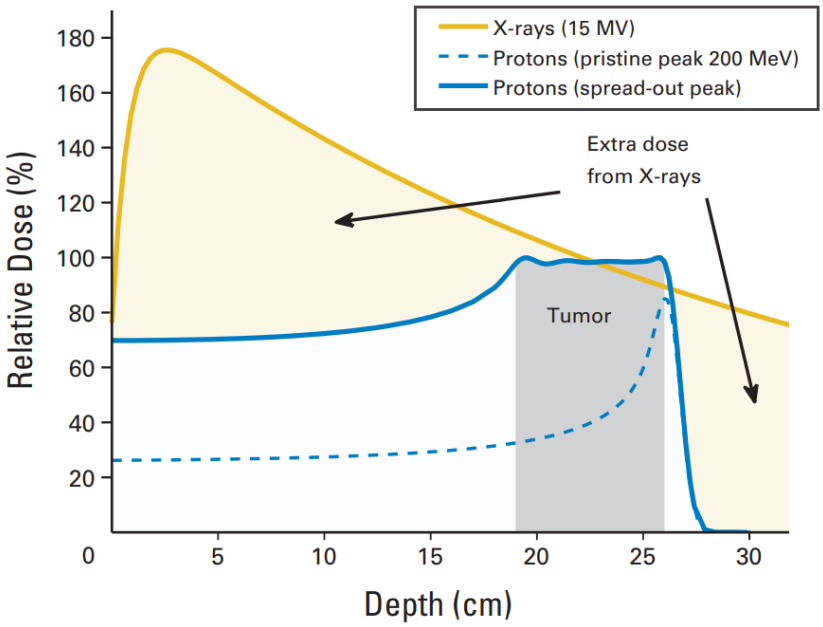

Figure 2.21: Comparison of relative depth dose distributions of photons versus protons. The comparison is made for 15MV X-rays, 200MeV protons and a spread out 200MeV proton peak. [73].

Overall, proton therapy is able to deliver a dose more locally concentrated, therefore sparing healthy tissue. The well-defined range allows for treatments of tumours with an Organ At Risk (OAR) behind them. However, errors like the movement of the patient, breathing, moving internal structures and setup uncertainty make positioning the Bragg peak inside the tumour more difficult. In-vivo, there are methods to validate the proton range, for example, prompt γ's (online), PET (on/offline) and MRI (offline) [74]. However, it is also important to calibrate and verify the proton beam energy, position and shape before treatment or in a research setting. Current methods make use of ionisation chambers. The Timepix, with its energy and spatial measurement abilities, should be able to do the same and might be a new tool to do proton beam research, as measurements with high energy protons are possible [14][15][16].

3

Methods

3.1. Preparing the Timepix and making holders of ^{225}Ac

In order to accurately determine the energy of the incoming α-particles, the distance between the source and the sample should be as short as possible. The Timepix comes with a protective casing where the sensor is positioned lower than the surface of the Timepix detector to prevent the sensor from being touched. This casing is swapped with an in-house 3D-printed casing, which has the same shape, but is lower and allows placement of a foil of 1.8μm Mylar above the sensor to protect it from contamination and dust. The distance between the top of the casing and the sensor is now 4mm approximately. The Timepix3 with custom casing and Mylar is shown in Figure 3.1.

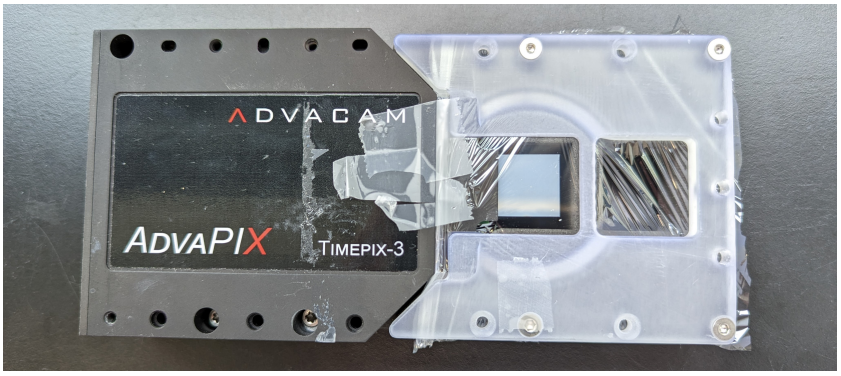

Figure 3.1: The Timepix3 detector from ADVACAM used in this research. The normal casing is removed and replaced with a 3D-printed casing displayed on the right. Mylar is placed in the new casing protecting the detector chip. Some tape was applied to straighten the Mylar.

Samples of ^{225}Ac are made by pipetting a solution of dissolved ^{225}Ac in 0.01M HCl onto a holder, which is 3D printed in-house, shown in Figure 3.2. The holder itself is made out of plastic and has a hole in the middle with a glass plate. ^{225}Ac is pipetted on the glass plate and dried by air in a fume hood. This process can be repeated to make a spot with high activity or you could make any other shape. When the ^{225}Ac solution has dried, a foil of 1.8μm Mylar is placed on top of the holder and tightened by screwing a plastic ring with a rubber ring on top of the holder with Mylar to create a closed source of ^{225}Ac. The holder can then be placed standing upright or laying flat on top of the Timepix. Figure 3.3 shows the sample holder in its usual position, laying flat on top of the Timepix.

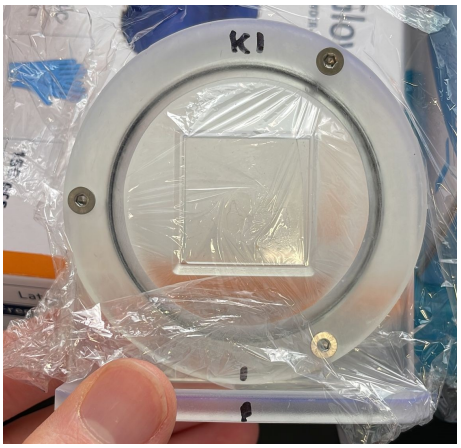

Figure 3.2: The sample holder which was used to create closed sources of ^{225}Ac [75]. On the glass plate, the sample is pipetted and a sheet of Mylar together with the seal ring creates a closed source.

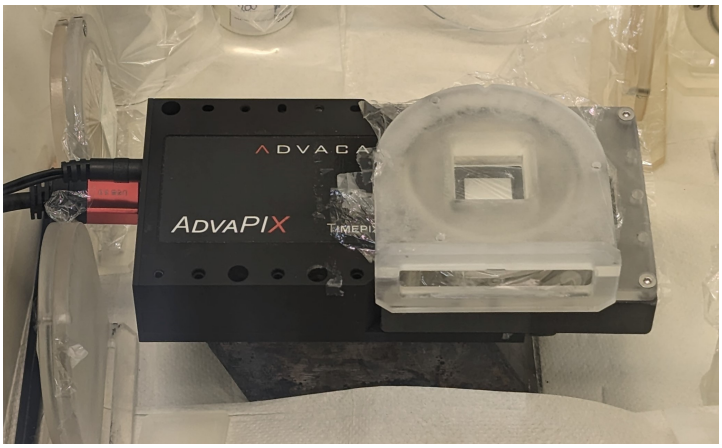

Figure 3.3: The sample holder is placed horizontally on the Timepix detector. This was the configuration of most experiments.

3.2. Determining the correct bias voltage for the Timepix

The experiment is set up as follows: A sample holder, made by the method explained in Section 3.1, with a droplet of 2µL containing 360Bq ^{225}Ac is placed on top of the protective casing of the Timepix directly above the chip. No collimator is used since we are only interested in what happens to the α's with the highest energy. Then, measurements of 60 seconds are made with bias voltages: [10, 15, 20, 25, 30, 35, 40, 45, 50, 55, 60, 70, 80, 100, 150, 200]V. The highest bias voltage for which no volcano effect occurs will be used in all further experiments.

3.3. Calibration of Timepix

3.3.1. Gamma calibration

The first calibration is done by using γ sources as explained in Section 2.3.3. This is done by using well-defined γ-emitters. The chosen nuclides are: ^{57}Co (electron capture), ^{133}Ba (electon capture) and ^{241}Am (α decay). ^{57}Co emits low energy gammas with energies: 14.4keV, 122.1keV and 136.5keV [5], of which only 14.4keV is detectable as single pixel hits as mentioned in 2.3.3 and as is visible in Figure 2.14. ^{133}Ba has a pronounced low energy x-ray peak at 30.973keV. ^{241}Am and its daughters emit a whole range of γ's (and x-rays). The spectra of ^{57}Co, ^{133}Ba and ^{241}Am are shown in Figure 3.4. Their respective activities on the day of measurement are 720kBq, 3.2MBq and 374kBq. A Gaussian was tried to be fitted for the following energies [5][76]:

1. ^{57}Co: 14.4129keV
2. ^{133}Ba: 30.973keV
3. ^{241}Am: 13.81keV, 17.7keV, 26.34keV and 59.5409keV

For ^{57}Co and ^{241}Am these energies were the most distinguishable peaks as also seen in Figures 2.14 and 3.4.

The experiment is set up as follows: The closed source is placed on top of the protective casing of the Timepix above the chip, during each measurement the closed source is shifted over the detector surface to ensure that all pixels have enough measurement data. The measurement times were 143 hours, 22 hours and 220 hours for ^{57}Co, ^{133}Ba and ^{241}Am respectively. The data is then filtered on single-pixel hit gammas and sorted per pixel. Then Gaussian functions are individually fitted over a selection of peaks to find the centre of the peak. All Gaussian fits are checked for correctness by manually redoing fits with large errors (standard error of any parameter > 2) and fitted centres at unexpected positions (depending on the position of other peaks and deviation from the average of all the same peaks from

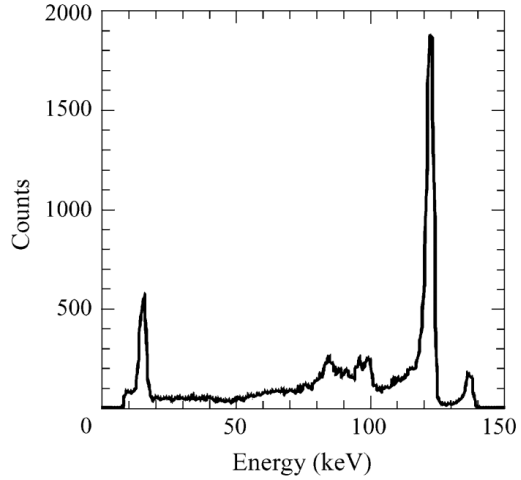

(a) ^{57}Co spectrum acquired by irradiating an In/CdTe/Au detector [77].

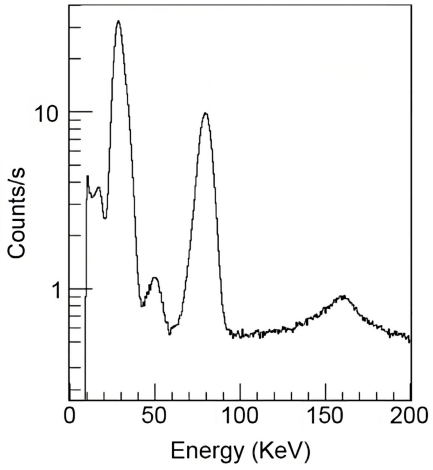

(b) ^{133}Ba spectrum acquired by irradiating a GECAM prototype detector based on $LaBr_3$ scintillators, adapted from [78].

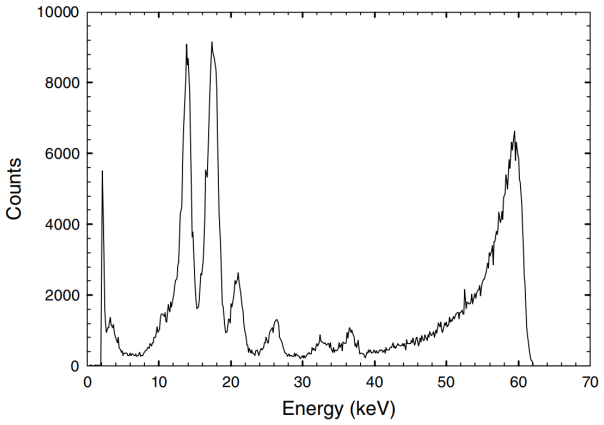

(c) ^{241}Am spectrum acquired by irradiating a CdTe detector [79].

Figure 3.4: The low energy γ spectra of ^{57}Co (left), ^{133}Ba (right) and ^{241}Am (bottom) measured with different detectors.

other pixels). After fitting, ToT values are matched to the energy of incoming radiation for each pixel. Since this relation is linear in the measured range, a linear fit is made for each pixel using the values of the 6 measured peaks. Each data point is weighted with the standard error of the fitted parameter (μ) and thrown out if this error was larger than 3, which means that the error could not be reduced in the previous step. These linear fits are automatically checked for fits with data points far from the linear fit and redone without the outlying data point, of which the condition was that data points should have a maximum deviation of 3keV to the fitted function. Faulty pixels (no response or not able to produce correct fits) are saved to be able to throw away data coinciding with that pixel in the future for data processing. Finally, this results in two correction factors (a, b) for each pixel which makes the response of each pixel more uniform, increasing the overall energy resolution. This calibration is done twice, where for the second time skewed Gaussians were used instead of normal Gaussians whenever this provided a fitted parameter with a lower standard error. Furthermore, the response before and after both γ calibrations will be compared to validate the calibration with the following experiments:

1. Measuring the γ spectrum of ^{241}Am for single-pixel and multi-pixel hits in a setup similar to the γ calibration with a run-time of 1h
2. Measuring the ^{225}Ac α spectrum using the same 2μL droplet setup as in Section 3.2 but with a run-time of 1h and an activity of approximately 360Bq.
3. Measuring the ^{225}Ac α spectrum using a 2μL droplet of 1.2kBq and a 3D-printed plastic collimator on 2 different positions of the detector surface (the sample holder is moved). The 3D-printed plastic collimator had an L/D of 2.5. Here the measurement time of both positions is 22h.

For these measurements, the spectrum will be analysed to check if the energy of the peaks matches the theoretical value and the energy resolution is determined by fitting a (modified) Gaussian to find out if an improvement in energy resolution is attained. The best γ calibration is used in all following experiments.

3.3.2. Alpha calibration

The second calibration, which is the α calibration as also explained in Section 2.3.3, is performed using a ^{241}Am source (α: 5485.56keV (84.8%) & 5442.80keV (13.1%), $t_{1/2}$=432.6y) [5]. In this case, the ^{241}Am source is contained in a smoke detector. The ^{241}Am itself is fused in a thin gold foil and has an activity of approximately 33kBq as is common for these smoke detectors [80][81]. The shape of the source is a circle with a radius of approximately 3mm and is recessed within its container approximately 5mm. The smoke detector is also shown in Figure 3.5a and the ^{241}Am source in detail is shown in Figure 3.5b. The ^{241}Am source is collimated on top of the container with a slab of plastic of 2mm thickness containing a small circular hole of 0.5mm in order to collimate the emitted α-particles (L/D=4), which is shown in Figure 3.6. The smoke detector is then placed on an x-y translation table with a step size of 5μm driven by a Phigets stepper motor and controller [82]. The Timepix detector is placed above it facing down using a metal stand. The approximate distance between the detector chip and the ^{241}Am source is 9mm. The setup (without smoke detector and Timepix) is shown in Figure 3.7. The whole surface of the Timepix is then scanned by moving the smoke detector with the translation table using 52x52 steps of size 275μm (5 pixels) and a waiting time between each step of 210s. The data is then processed where the average measured energy is then determined for each pixel using the two methods mentioned in Section 2.3.3, which are: saving the measured energy of the α-particle in the pixel which coincides with the centre of mass of the blob and the neighbouring pixels in a 7x7 block and saving the measured energy using a weighting factor based on the average Gaussian shape of the blob. This measured energy is then averaged and will be imaged for the whole detector surface. The proposed correction factor is then based on the deviation from the average of the whole detector surface and can be scaled for larger energies. In order to test the improvement of resolution and uniformity of the detector using the measured average energy, the following experiments are performed:

- The α spectrum of ^{241}Am is determined using the same data from the calibration. This is done without γ calibration, with γ calibration and for both methods of α calibration.
- The α spectrum of a droplet of ^{225}Ac on 2 different positions is determined using the same measurement data from the experiment in Section 3.3.1.

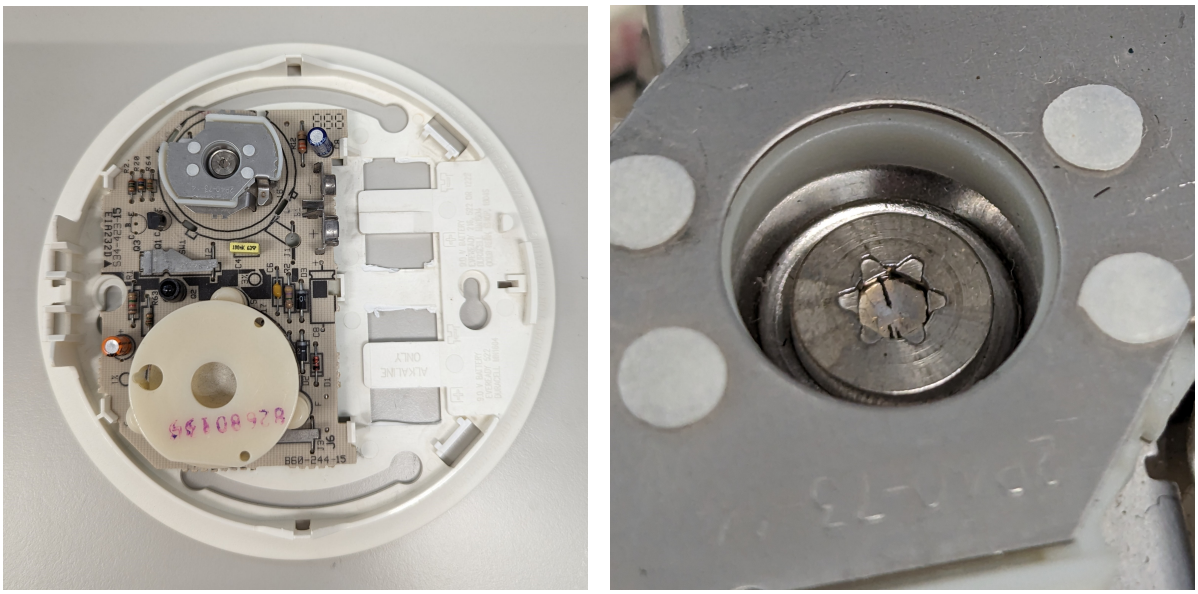

(a) Total view (b) Zoomed on the source

Figure 3.5: The smoke detector, shown in total in (a), containing a small 33kBq ^{241}Am source, which is shown in detail in (b).

Figure 3.6: The ^{241}Am source of the smoke detector with a plastic single-hole collimator (0.5mm), which is indicated with the red arrow.

3.4. Determining the energy resolution using different collimators

In order to find a suitable collimator it needs to be determined what the energy and spatial resolution are of the Timepix combined with the collimator. Two collimators are used for determining the energy resolution:

1. 3D printed plastic collimator: L=2.5mm, D=1mm, L/D=2.5, pitch=1mm
2. Lead-glass collimator : L=500µm, D=10µm, L/D=50, pitch=24.8µm

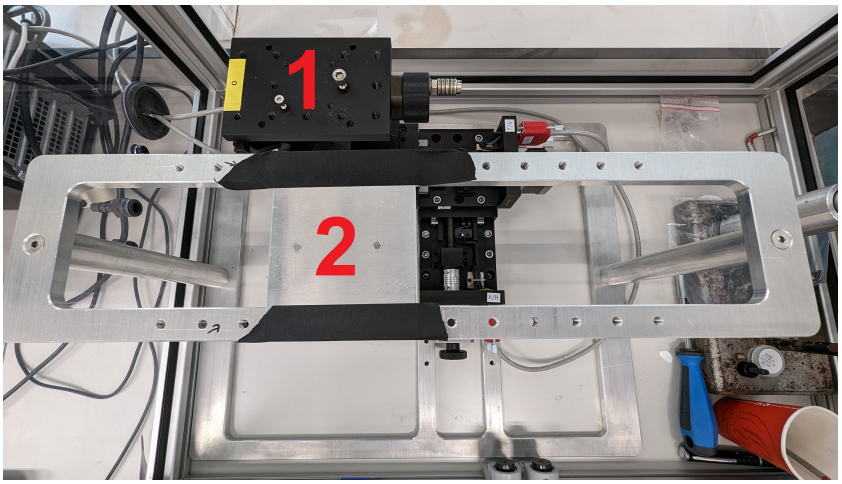

(a) Top view

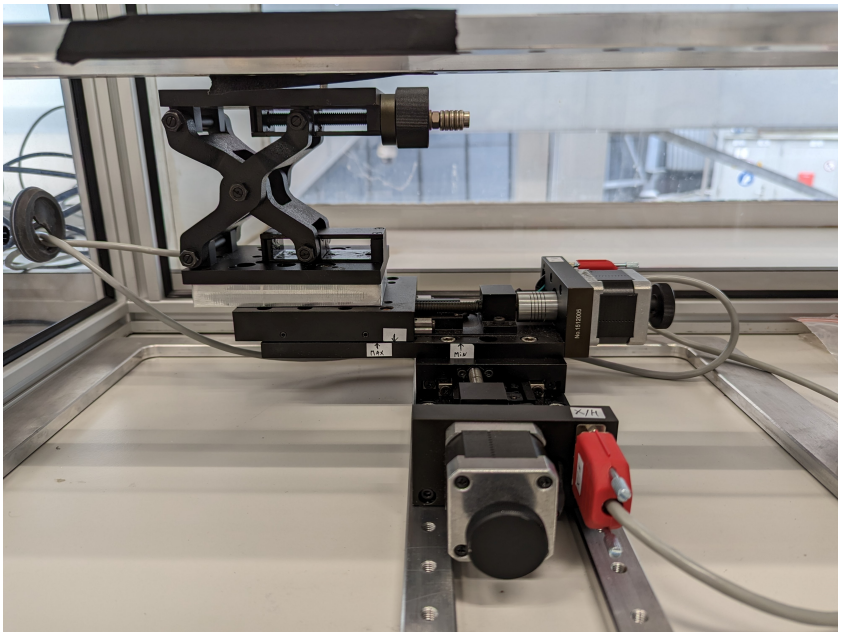

(b) Front view

Figure 3.7: The x-y translation table used in the α calibration. Provided is a top (a) and front view (b). On the top view, the number 1 indicates the position of the smoke detector and the number 2 indicates the position of the Timepix. Both are not present in this figure.

The energy resolution will be determined as follows: A sample holder will be made using the method as explained in 3.1. The sample holder contains on the date of experimentation 20kBq spread out on the surface, by pipetting multiple small droplets, letting them dry and pipetting again repeatedly. Then the collimator is placed on the Timepix and the sample holder on top. A measurement is done for 13 hours for the first collimator and 15 hours for the second collimator. A spectrum will be determined for the data on the whole surface of the detector by using different calibrations and a Gaussian is fitted on the ^{213}Po peak. The energy resolution is then calculated by using the theory from Section 2.6.

The same setup is used to determine the spatial resolution, however, now a cover glass (borosilicate) is used of size 20x26mm and a thickness of 400µm (well above the range of an 8.4MeV α-particle (^{213}Po) in borosilicate glass, R_α=230µm) to create a well-defined edge [21]. The spatial resolution is then again calculated by the same theory in Section 2.6. This time, however, only the first collimator is used. A measurement time of 140 hours was taken with an activity of approximately 300Bq.

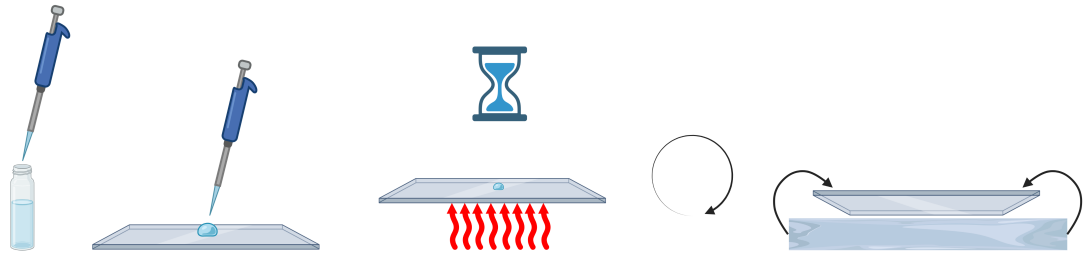

Figure 3.8: The steps to create the sample holder for the Erasmus measurements are shown here schematically. The steps are explained in more detail in the text. This image was created with BioRender.

3.5. Related projects

Some experiments were performed not related to the main research question. These were nevertheless interesting to conduct and used the same Timepix technology and allow to show the versatility of the Timepix.

3.5.1. HPLC fraction of Ac225-PSMA

For this experiment 10kBq ^{225}Ac-PSMA is run through a HPLC to separate the unbound and bound radio-pharmaceutical. A single fraction is taken in which the most ^{225}Ac-PSMA is present (determined beforehand with γ spectroscopy). The following steps were taken to prepare a sample for the Timepix, also shown in Figure 3.8:

1. 10µL is pipetted from the fraction.
2. The solution is pipetted onto a microscopic glass
3. The microscopic glass is placed on a pre-heated heating plate set to ~60°C for about 60 seconds.
4. As the solution is dried, the microscopic glass is flipped and placed on a sheet of 1.8µm Mylar sheet, which was cut slightly larger than the microscopic glass, and taped shut in order to create a closed source.

The sample is then measured by placing it without a collimator on top of the Timepix casing above the chip. 30 continuous measurements were performed each of 60 seconds, which were eventually bundled into 6x5 minute intervals.

3.5.2. Proton beam measurements

For this experiment, the Timepix was placed inside the proton beam at the research bunker of HollandPTC. The proton beam was varied in energy (MeV) and intensity (nA). For each setting, RW3, a water-equivalent phantom material, with various thicknesses was placed in between the proton beam and the Timepix detector to reduce the energy of the protons. Each time the proton beam was turned on for 10 seconds. The setups that were tried are shown in Table 3.1

Energy (MeV)	Intensity (nA)	Thickness of RW3 (mm)	Beam profile
70	2	0, 34, 36, 38, 39, 40	Pencil
120	5	0, 98	Flat Field

Table 3.1: The configurations of the proton beam and attenuation used for proton beam measurements.

Hereafter another experiment was performed where a wafer of Silicon was positioned in a 70Mev 2nA pencil beam at an angle with the Timepix detector positioned at a small distance (16mm and 50mm) from the wafer outside of the proton beam. The irradiation time was again 10 seconds.

4

Results & Discussion

In this chapter, each experiment is divided into a subsection, where the results are first given followed by a discussion. At the end, a summary is given along with a general discussion of this research and some recommendations.

4.1. Results & Discussion of the individual experiments

4.1.1. Finding an appropriate bias voltage

Measurements were conducted for a duration of 60 seconds and a spectrum was determined for each bias voltage. The spectra are shown in Figures 4.1 and 4.2. At the lowest bias voltages, the peaks are indistinct and have low counts. As the bias voltage increases, the peaks become more prominent, higher in intensity, and shift towards higher Time-over-Threshold (ToT) values. When the bias voltage reaches 35V or higher, the highest peaks start to decrease in intensity, making it more challenging to distinguish individual peaks. Furthermore, the united peak shifts towards lower ToT values. For higher energies, there appears to be an increase in the small peak near zero ToT.

Clearly, the lower settings of 10V, 15V, 20V and 25V are not usable for measuring the spectrum of ^{225}Ac. The count rate is low, and the four peaks are not separated. This is because for lower bias voltages the heavy blob patterns of the detected α-particles get broader and have a ToT value in their centre of mass which is very small, due to the weaker acceleration of charge onto the readout chip causing charge to diffuse in the silicon. It also causes the measured ToT to overlap. For larger bias voltages, 30V and 35V, the four alpha peaks of ^{255}Ac are clearly visible, albeit with some overlap due to the statistical spread and the fact that no collimator is used and the whole detector surface is included in this measurement. As the spread of the centres of the peaks is the largest and no volcano effect occurs for these two bias voltages, they seem to be the ideal bias voltages for this particular setup, which is also confirmed by the fact that for larger energies, the volcano effect started to occur. This can be seen by the peaks becoming merged again and decreasing in ToT as the bias voltage increases. This is because the resulting heavy blob patterns become narrower and the centre of the blob increases significantly in ToT value, due to the larger acceleration of charge onto the readout chip, causing the pixel to become over-saturated and distorting the output signal as shown in Figure 5. The effect on the measured shape was also shown in Figure 6, which is from the same experiment. To be on the safe side, a bias voltage of 30V was chosen as the default setting for all following experiments, since for 35V, the last peak (^{213}Po) already seems to be at its maximum value, which is confirmed by the 40V and 45V measurements.

The left peak near zero appears caused by misidentifying γ- or β-particles as α-particles. The data for this experiment was processed using an older version of the data processing code. This code only checks if the detected particle pattern is round, which γ- or β-particles could in particular cases be. It was chosen to leave it like that since later versions of the code used more checks like matching ToT and ToA and holes inside the cluster. If you were to analyse the data with the newest version, the volcano effect would be filtered out and the effect on the spectrum would not be as visible as it is now.

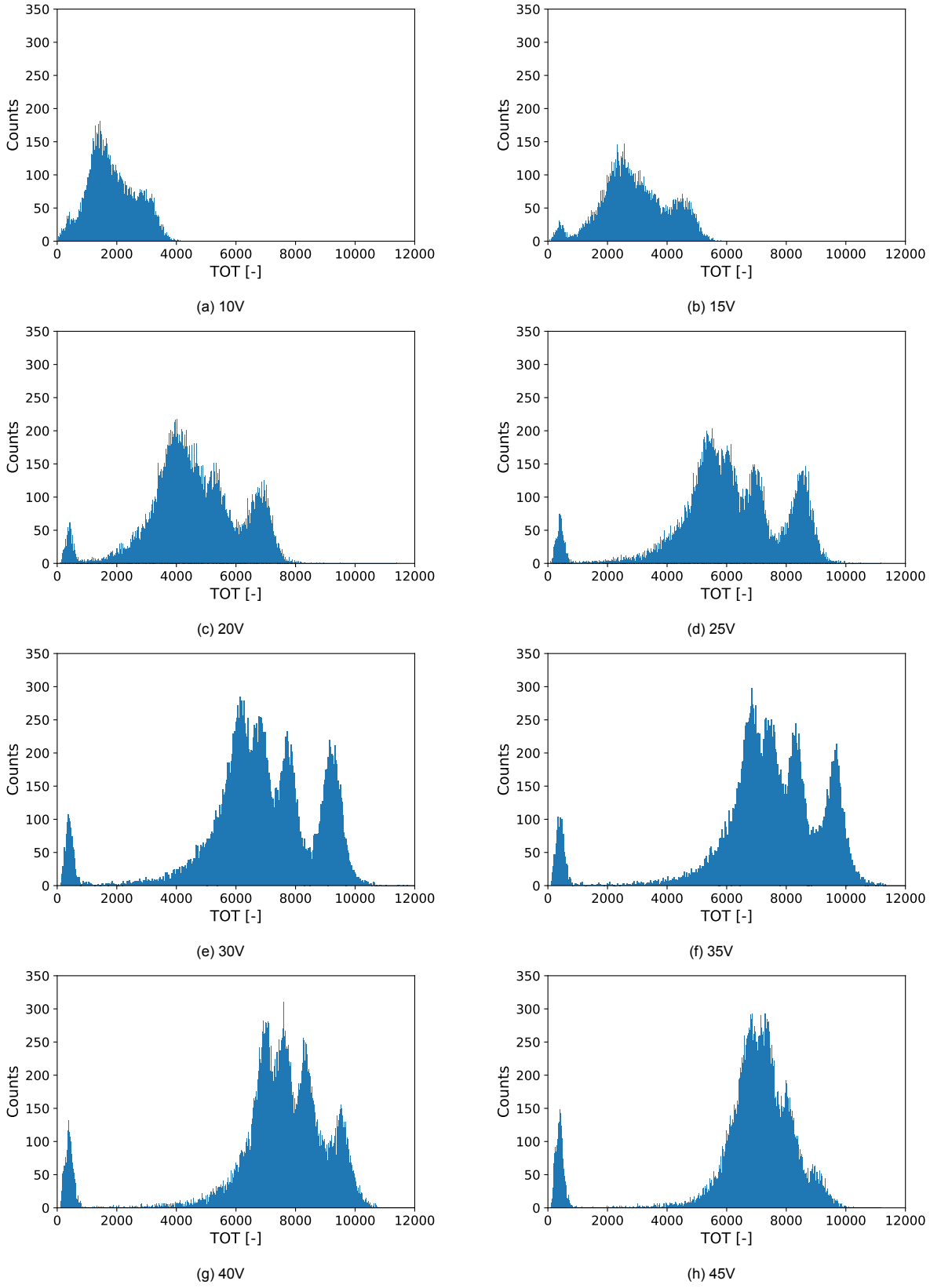

(a) 10V (b) 15V

(c) 20V (d) 25V

(e) 30V (f) 35V

(g) 40V (h) 45V

Figure 4.1: Plots of the α spectrum of a measurement with ^{225}Ac. Each of these measurements was performed with a different bias voltage, which ranged from 10V-45V in steps of 5V, shown in (a)-(h) respectively. The threshold was set to 2.01keV.

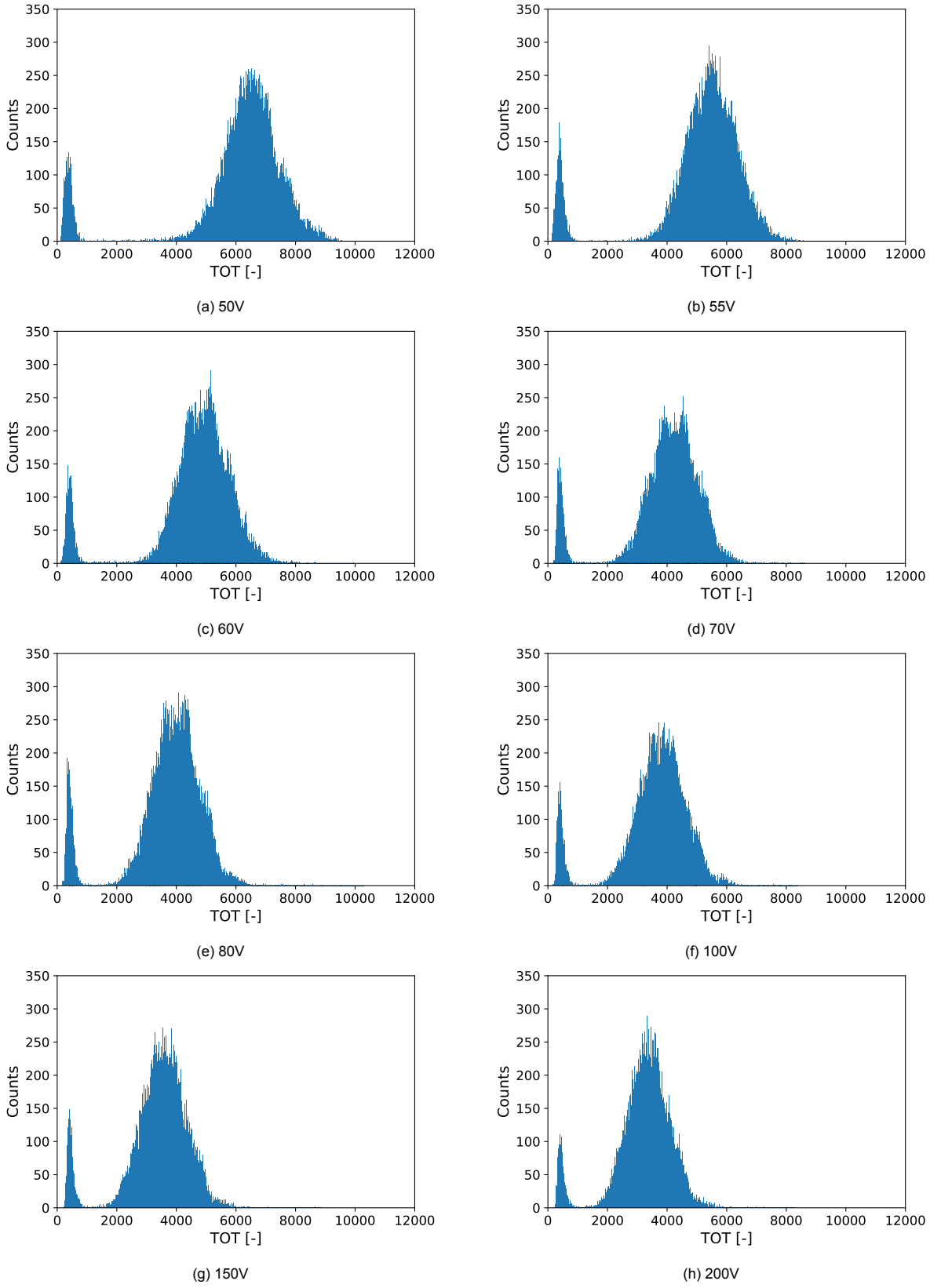

(a) 50V (b) 55V

(c) 60V (d) 70V

(e) 80V (f) 100V

(g) 150V (h) 200V

Figure 4.2: Plots of the α spectrum of a measurement with ^{225}Ac. Each of these measurements was performed with a different bias voltage, which ranged from 50V-200V with various steps in (a)-(h) respectively. The threshold was set to 2.01keV.

4.1.2. Gamma calibration

The Timepix has been calibrated by fitting a total of 6 (skewed) Gaussian functions to pronounced low energy γ peaks detected as single pixel hits on the detector of the following nuclides: ^{57}Co, ^{133}Ba and ^{241}Am. The fitted mean value of the peaks (μ) was matched with the corresponding energy and a linear fit was made for each pixel (256x256). All Gaussian and linear fits were checked for outliers and significant errors and manually redone if required. The calibration was performed twice, as was mentioned before. The first time using normal Gaussians and the second time with skewed Gaussians whenever this provided a lower standard error of the fitted parameter (also referred to as calibration 1 and calibration 2). For the first calibration, 32 pixels were not able to be calibrated due to errors or pixels being dead. This was 62 for the second calibration[1].

First, in Figures 4.3 and 4.4 the single-hit γ spectrum of ^{57}Co, ^{133}Ba and ^{241}Am is shown for four different pixels, together in the resulting linear fit for the energy calculation. In this case, the mean of the peak was found by fitting normal Gaussians. In all three spectra, the peaks were pronounced enough to be fitted. The relation of the ToT value of the mean of the peaks and the corresponding energy seems to be linear for all four pixels. The γ spectra of all three nuclides for a single pixel of the Timepix detector look very similar to the γ spectra found in literature, which are shown in Figure 3.4. The 59.54keV peak of ^{241}Am is much smaller than the other peak, even though it has a probability of 35.9% [5]. This is because the chance of the γ radiation being a single hit reduces for increasing energy, as was also shown in Figure 2.15. Also, the higher energy peaks of ^{57}Co and ^{133}Ba, 122.06keV and 80.997keV, were not visible [5]. This confirms that the 59.54keV peak is around the practical limit for this calibration.

Then both calibrations were tested on multiple measurements. For each case, the non-calibrated and both calibrated spectra are compared. Starting with the single-pixel and multi-pixel hit spectrum of ^{241}Am. Then, the ^{225}Ac droplet measurement. Finally, the ^{225}Ac droplet measurement on two positions of the detector surface with a collimator.

4.1.2.1 Single-/multi-hit Am-241 gamma spectrum

The resulting single-/multi-hit ^{241}Am γ spectra without and with both types of γ calibrations are given in Figure 4.5. For all calculated spectra a (modified) Gaussian fit was made to determine the centre of the measured 59.54keV gamma peak (μ) and to determine the energy resolution, based on the FWHM. These results are given in Table 4.1. For both calibrations, the single-hit spectrum improved significantly in energy resolution. Figure 4.5 shows a clear separation between the most prominent γ peaks of ^{241}Am and the spectrum looks similar to the spectrum measured in literature, also seen in Figure 3.4. For all cases, the peaks in the multi-hit spectrum were broader and less separated. The energy resolution for low energy γ peaks was improved from 24.0±0.4% to 4.02±0.02% in the single-hit case and improved from 21.9±0.3% to 4.2±0.1% in the multi-hit case. In none of the calibrations, neither single-hit nor multi-hit, was the fitted centre position of the 59.54keV within a standard error of the fitted parameter. The first and second calibrations were similar in results.

Table 4.1: Results of the γ calibration verification with the γ spectrum of ^{241}Am. Here the fitted centre position of the 59.54keV γ peak is shown and the energy resolution. For the no calibration case, the fitted centre is not given, since this does not correspond to an energy value.

	Single-hit			Multi-hit		
	No Calibration	Calibration 1	Calibration 2	No Calibration	Calibration 1	Calibration 2
μ [keV]	N/a	59.41±0.04	59.64±0.01	N/a	59.44±0.02	59.82±0.02
E_{res} [%]	24.0±0.4	4.1±0.2	4.02±0.04	21.9±0.3	4.23±0.09	4.2±0.1

[1] From this moment a lot of discussion will be about energy resolution. In order to prevent misunderstandings: A higher or better resolution means that the FWHM/E is **lower** and a lower or worse resolution means that the FWHM/E is **higher**.

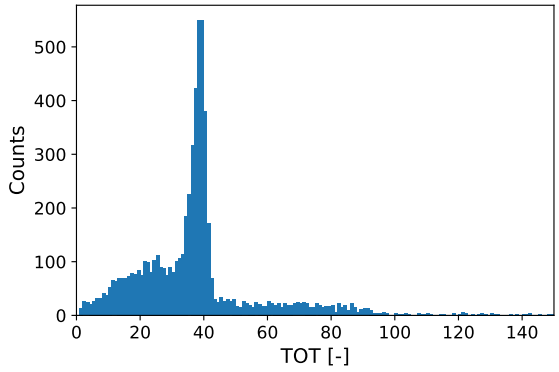

(a) Measured single-hit gamma spectrum of ^{57}Co using a single pixel (20,150) of the Timepix detector.

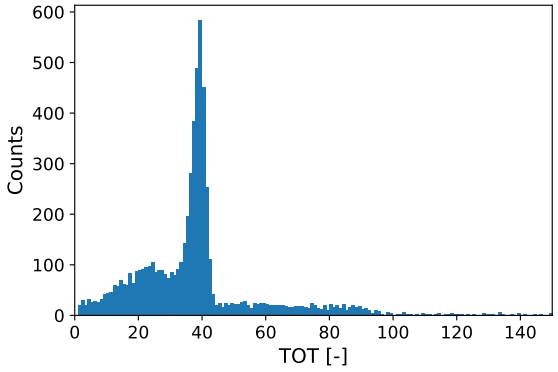

(b) Measured single-hit gamma spectrum of ^{57}Co using a single pixel (100,50) of the Timepix detector.

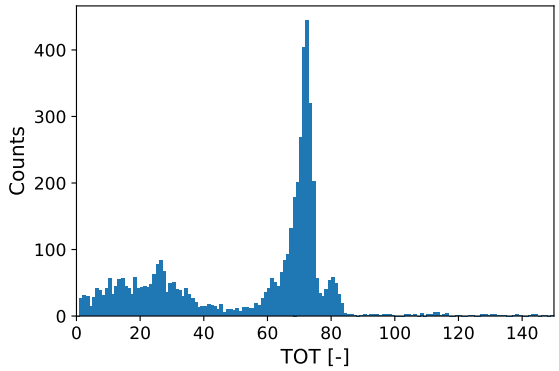

(c) Measured single-hit gamma spectrum of ^{133}Ba using a single pixel (20,150) of the Timepix detector.

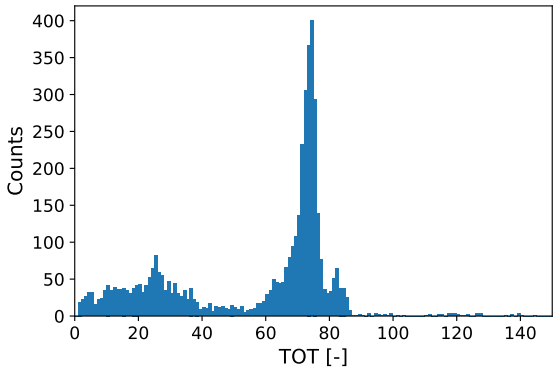

(d) Measured single-hit gamma spectrum of ^{133}Ba using a single pixel (100,50) of the Timepix detector.

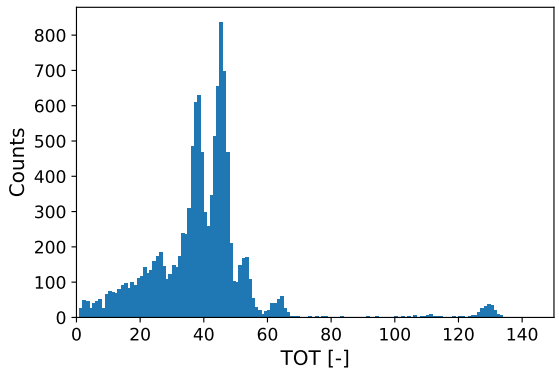

(e) Measured single-hit gamma spectrum of ^{241}Am using a single pixel (20,150) of the Timepix detector.

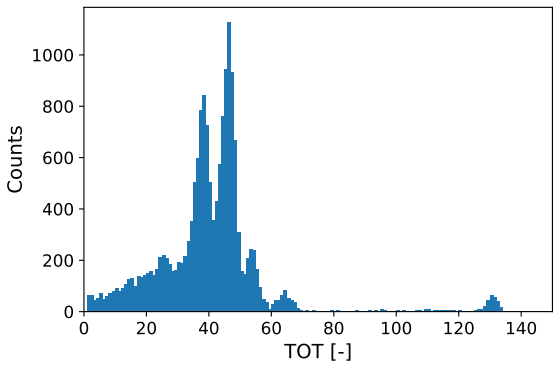

(f) Measured single-hit gamma spectrum of ^{241}Am using a single pixel (100,50) of the Timepix detector.

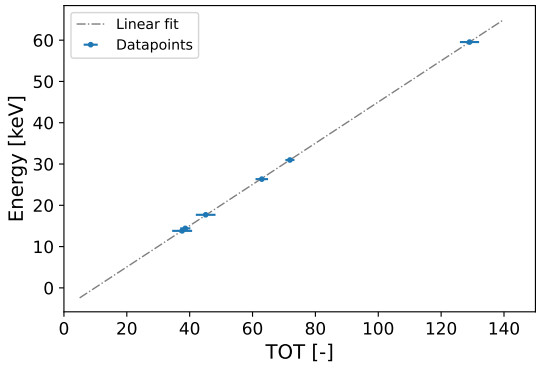

(g) Resulting linear fit of the single-hit spectra and corresponding peak energies of a single pixel (20,150) of the Timepix detector.

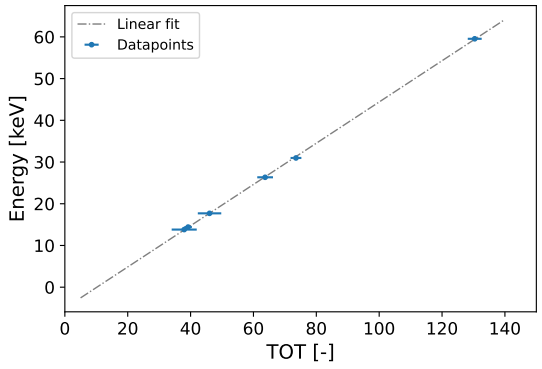

(h) Resulting linear fit of the single-hit spectra and corresponding peak energies of a single pixel (100,50) of the Timepix detector.

Figure 4.3: These plots show the measured single-hit spectra of different nuclides (top 3 rows) for a single pixel (L:(20,150), R:(100,50)). At the bottom, the resulting linear fit is shown of the energies and measured ToT value for the respective pixel, which is the calibration curve of that pixel. The threshold was set to 2.01keV and the bias voltage to 30V.

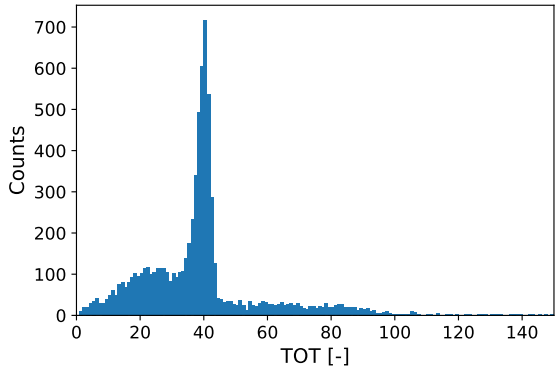

(a) Measured single-hit gamma spectrum of ^{57}Co using a single pixel (150,80) of the Timepix detector.

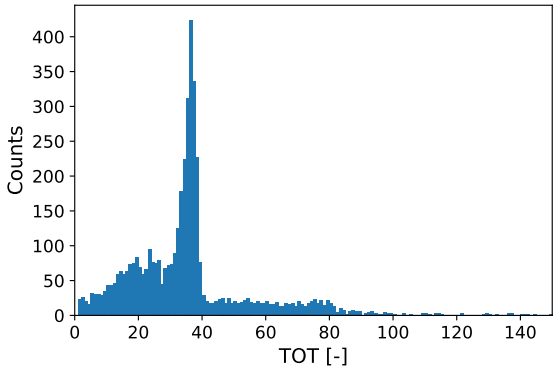

(b) Measured single-hit gamma spectrum of ^{57}Co using a single pixel (200,25) of the Timepix detector.

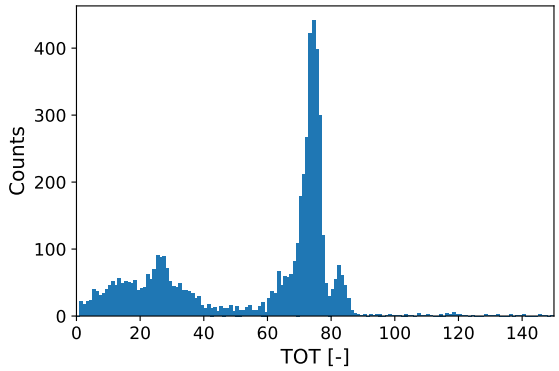

(c) Measured single-hit gamma spectrum of ^{133}Ba using a single pixel (150,80) of the Timepix detector.

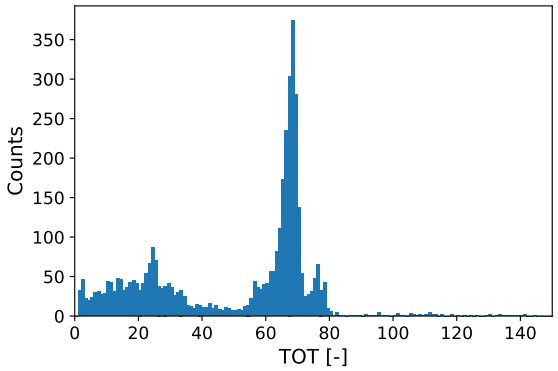

(d) Measured single-hit gamma spectrum of ^{133}Ba using a single pixel (200,25) of the Timepix detector.

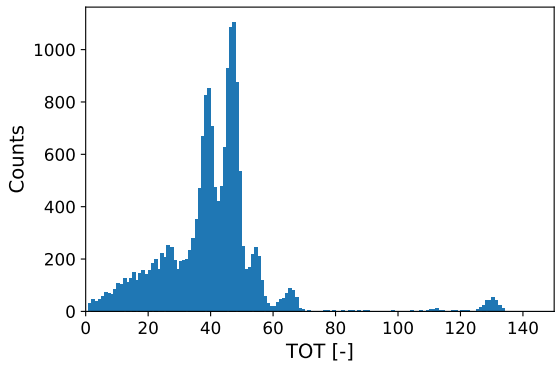

(e) Measured single-hit gamma spectrum of ^{241}Am using a single pixel (150,80) of the Timepix detector.

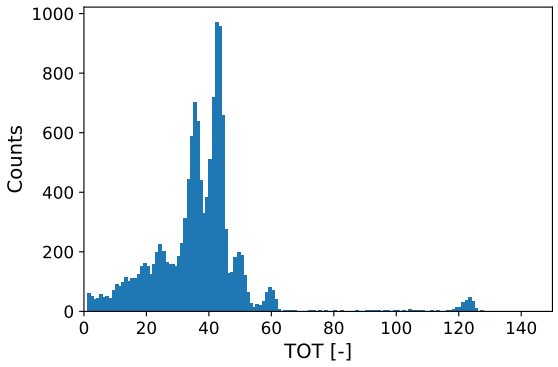

(f) Measured single-hit gamma spectrum of ^{241}Am using a single pixel (200,25) of the Timepix detector.

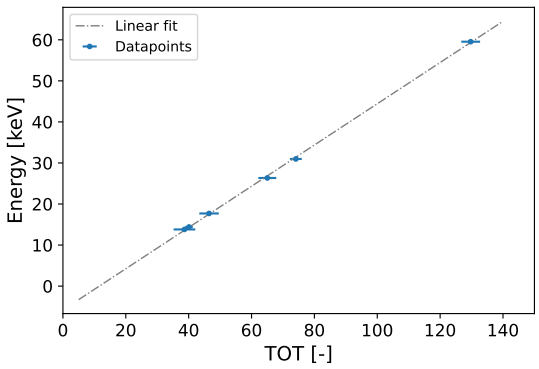

(g) Resulting linear fit of the single-hit spectra and corresponding peak energies of a single pixel (150,80) of the Timepix detector.

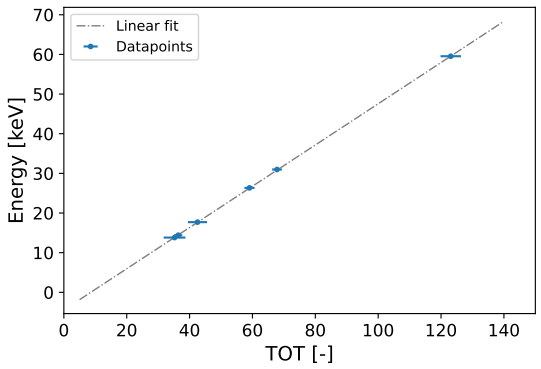

(h) Resulting linear fit of the single-hit spectra and corresponding peak energies of a single pixel (200,25) of the Timepix detector.

Figure 4.4: These plots show the measured single-hit spectra of different nuclides (top 3 rows) for a single pixel (L:(150,80), R:(200,25)). At the bottom, the resulting linear fit is shown of the energies and measured ToT value for the respective pixel, which is the calibration curve of that pixel. The threshold was set to 2.01keV and the bias voltage to 30V.

Even though there is a slight deviation in the centre position of the measured 59.54keV peak, the spectrum overall is very similar to literature and the measured energy and energy resolution are a huge improvement over the non-calibrated case. The broadening of the spectrum in the multi-hit case is most likely caused by larger variations in the measured charge, due to induced charge carriers in the silicon leaking or diffusing into neighbouring pixels, which is not detected since the energy is below the energy threshold (2.01keV). This variation is larger due to the fact that there are more neighbouring pixels for a multi-pixel detection. For low energy γ radiation, this phenomenon is more drastic, since the energy is near the threshold level. It is expected that the severity of this reduces if the measured energy per pixel increases. The measured energy resolution for multi-hit γ-radiation is probably slightly worse than the calculated result in Table 4.1. This is because this was based on the definition of the FWHM defined by the parameters μ and σ. However, for the fits, an exponentially modified Gaussian was fitted, where the FWHM would be much larger. If the FWHM was determined by its definition (Full-Width at Half Maximum) the energy resolution reduces for the multi-hit cases to approximately 10% for both cases, which is still a large improvement.

4.1.2.2 Small single Ac-225 droplet

The second verification is the 1-hour measurement of the 2µL droplet containing 360Bq of ^{225}Ac. In this case, no collimator was used. To achieve the same effect as a collimator, a mask of the detector surface was taken. Only pixels within a radius of 20 pixels from the centre of the measured droplet were taken to calculate the spectrum. Figure 4.6 shows the surface of the Timepix detector with measured α-particles and the effect of the mask. Figure 4.7 shows the effect of the mask on the calculated spectrum. Finally, in Figure 4.8 the calculated spectra are shown of the data without γ calibration and both types of γ calibrations. The results of the measured ^{213}Po α peak position and energy resolutions are given in Table 4.2.

Table 4.2: Results of the γ calibration verification with the α spectrum of a small uncollimated droplet of ^{225}Ac. Here the fitted centre position of the 8376keV α peak and the energy resolution is shown. For the no calibration case, the fitted centre is not given, since this does not correspond to an energy value.

	No Calibration	Calibration 1	Calibration 2
μ [keV]	N/a	4537.1±0.7	4551.6±0.8
E_{res} [%]	6.13±0.06	4.46±0.04	4.51±0.04

First of all, in all calculated spectra of the measurement of ^{225}Ac four α peaks are found, similar in height. In Figure 4.7 the effect of the mask on the spectrum is shown and the peaks are more separated and more defined, similar to the effect of a collimator. Furthermore, the energy resolution of the calibrations was found to be 4.46±0.04% and 4.51±0.04% in calibrations 1 and 2 respectively. This is an improvement from the case where no calibration was used, which was 6.13±0.06%. The found energy value for the ^{213}Po peak was around 4.5MeV for both calibration cases. This value is lower than the 8.4MeV found in literature for the α energy of ^{213}Po [5].

The found spectrum confirms that it is possible to measure α-particles emitted by ^{225}Ac with the Timepix3 detector since the four most common α-particles are visible in the spectrum, albeit with a lower than expected measured energy. From left to right: ^{225}Ac (5.8MeV), ^{221}Fr (6.3MeV), ^{217}At (7.0MeV) and ^{213}Po (8.4MeV) [5]. All four nuclides are in equilibrium, as was also predicted in Figure A.2. The determined energy resolution was better than the 5-10% found in literature for α-particles with energies above 1.5MeV [11]. This is a small improvement in energy resolution, though this was not the only goal of the calibration, which was also to make the response of the whole detector surface more uniform and to relate the ToT value, measured by the Timepix3, to energy. The uniformity of the detector surface is tested in the next validation. When comparing the measured centre of the ^{213}Po α peak to the true value of 8.4MeV, it was in both cases about 4MeV lower, which is quite significant. The α-particle loses

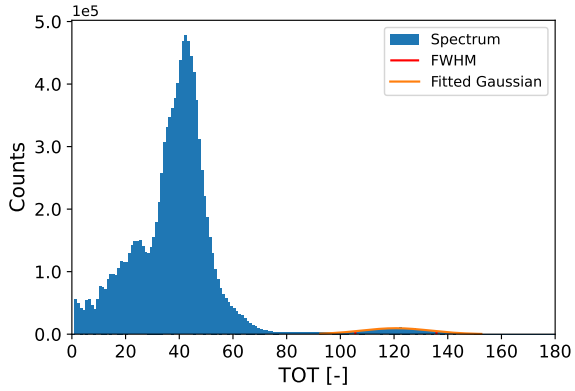

(a) The uncalibrated single-hit gamma spectrum of ^{241}Am.

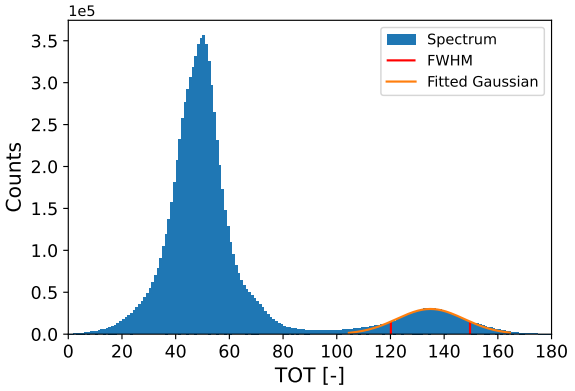

(b) The uncalibrated multi-hit gamma spectrum of ^{241}Am.

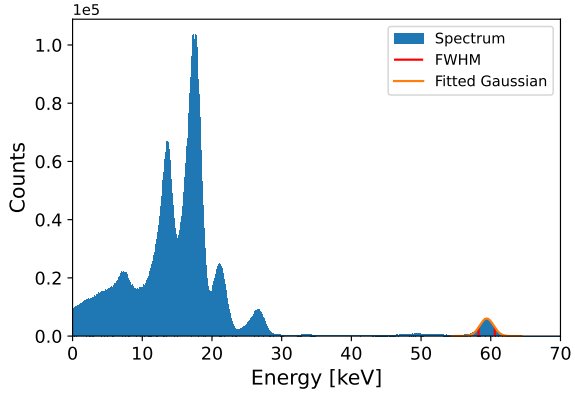

(c) The calibrated (first calibration) single-hit gamma spectrum of ^{241}Am.

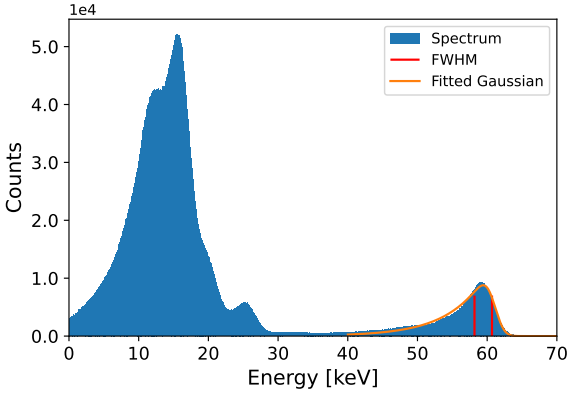

(d) The calibrated (first calibration) multi-hit gamma spectrum of ^{241}Am.

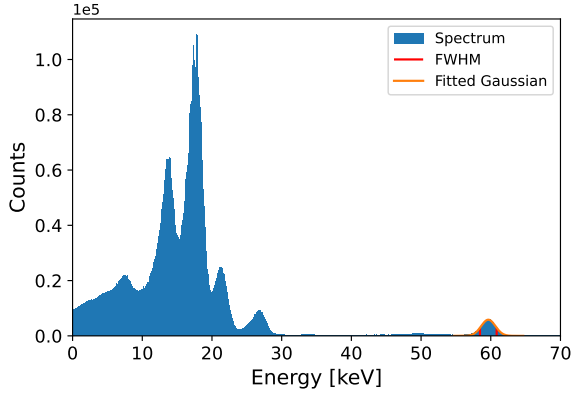

(e) The calibrated (second calibration) single-hit gamma spectrum of ^{241}Am.

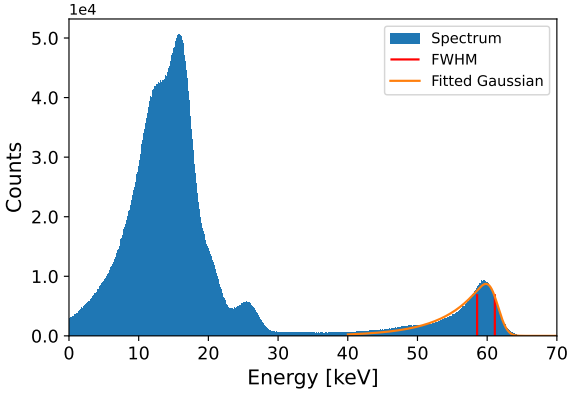

(f) The calibrated (second calibration) multi-hit gamma spectrum of ^{241}Am.

Figure 4.5: These sub-figures show different calculated spectra of the same 1-hour measurement of the γ spectrum of ^{241}Am using the whole surface of the Timepix3 detector (not homogeneously). For each spectrum, a (modified) Gaussian is fitted together with the FWHM, based on equation 2.6. On the left the single-hit spectra are shown and on the right the multi-hit spectra. From top to bottom, uncalibrated, calibration 1 and calibration 2 are shown. The threshold was set to 2.01keV and the bias voltage to 30V.

approximately 140keV when passing through 1.8µm Mylar, 250keV when passing through 4mm air and 150keV when passing through Mylar again until it reaches the detector surface [21]. This does not add up to the found value and is an indication that the measured α energy is an underestimation of the true energy when using γ calibration. It could be that the extrapolation of low energy γ's (tens of keV) to higher energy α's (thousands of keV) is too big a step and errors introduced by the γ calibration are thereby magnified. However, it is still possible to distinguish the different nuclides at lower measured energy. Again both calibrations yielded very similar results.

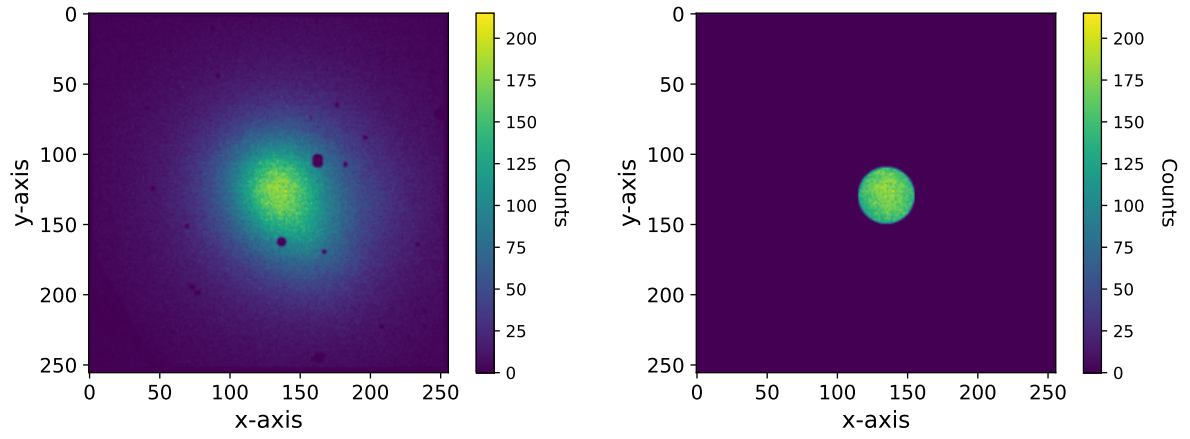

(a) Without a mask.

(b) With a mask.

Figure 4.6: Image of the detector surface showing measured α-particles from an uncollimated small droplet (2µL) of ^{225}Ac. Here the effect of the mask is demonstrated and only counts within 20 pixels of the centre are used. (a) shows the image without the mask and (b) shows the image with the mask. The black dots in the figure on the left are due to faulty pixels, which are pixels that are dead or of which no calibration could be made.

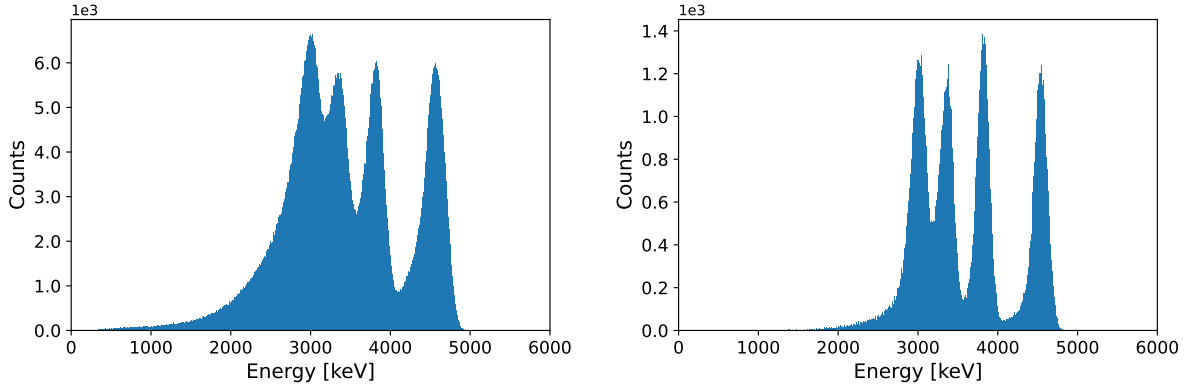

(a) Without a mask.

(b) With a mask.

Figure 4.7: α spectrum of an uncollimated small droplet (2µL) of ^{225}Ac showing the effect of masking the centre of the measured droplet. On the left (a) the spectrum is shown without the mask and on the right (b) the spectrum is shown with the mask. This spectrum was made with the first γ calibration (calibration 1). The threshold was set to 2.01keV and the bias voltage to 30V.

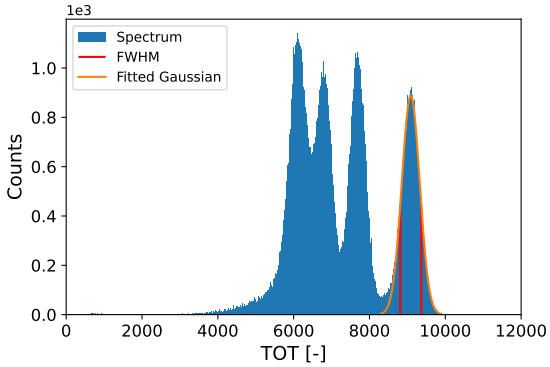

(a) No calibration

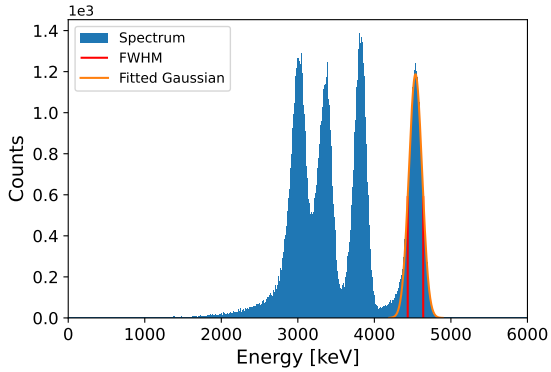

(b) Calibration 1

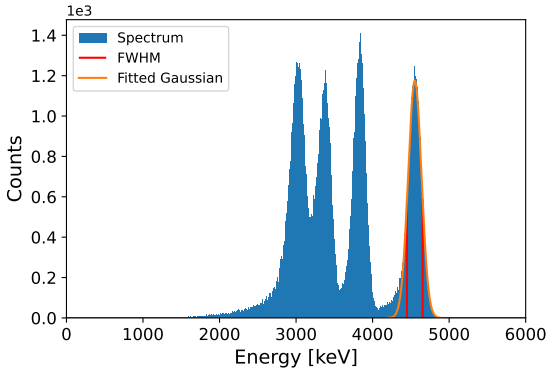

(c) Calibration 2

Figure 4.8: α spectrum of an uncollimated small droplet (2µL) of ^{225}Ac using different types of γ calibrations. In (a) the spectrum is uncalibrated, in (b) the first γ calibration is used and in (c) the second. The threshold was set to 2.01keV and the bias voltage to 30V.

4.1.2.3 Small Ac-225 droplet on two different positions

For the last validation the same droplet of ^{225}Ac was measured at two different positions of the detector surface collimated with an L/D of 2.5. Again the image, with and without a mask, is shown in Figure 4.9. This time the mask was chosen with a radius of 50 pixels, which is larger than the previous time since this time a collimator was used and the whole image can be used. Figures 4.10, 4.11 and 4.12 each show four graphs for each case (no calibration, calibration 1 and 2). The first two show the calculated spectra for each droplet separately, the third shows the combined spectrum and the last one shows the spectra of the two droplets calculated separately in the same figure. For each case the centre position and energy resolution of the ^{213}Po α peak was determined for both droplets separately and combined. These results are shown in Table 4.3.

Table 4.3: Results of the γ calibration verification with the α spectrum of a collimated (L/D=2.5) small droplet (2µL) of ^{225}Ac measured at two different positions. Here the fitted centre position of the 8376keV α peak and the energy resolution is shown for the two individual droplets and combined.

	No Calibration			Calibration 1			Calibration 2		
	Left	Right	Combined	Left	Right	Combined	Left	Right	Combined
μ [keV]	N/a	N/a	N/a	4522.8±0.8	4355±1	4428±2	4538±1	4368±1	4441±2
E_{res} [%]	6.35±0.04	7.07±0.06	6.70±0.05	5.65±0.05	4.27±0.06	7.5±0.1	5.72±0.06	4.29±0.07	7.5±0.1

In all spectra, four distinct α peaks were found similar in height. For both the left and right droplets the energy resolution improved with γ calibration. It went from 6.35±0.04% to 5.65±0.05% and 5.72±0.06% for calibrations 1 and 2 respectively and from 7.07±0.06% to 4.27±0.06% and 4.29±0.07%. This improvement in energy resolution is also visible in the calculated spectra, where the broadness of the α peaks reduced and the separation increased. However, for both calibrations, the peaks of both droplets shifted in centre position, reducing the energy resolution when the droplets were combined. In the combined case the energy resolution decreased from 6.70±0.05% to 7.5±0.1% and 7.5±0.1%. Again both calibrations were similar in results.

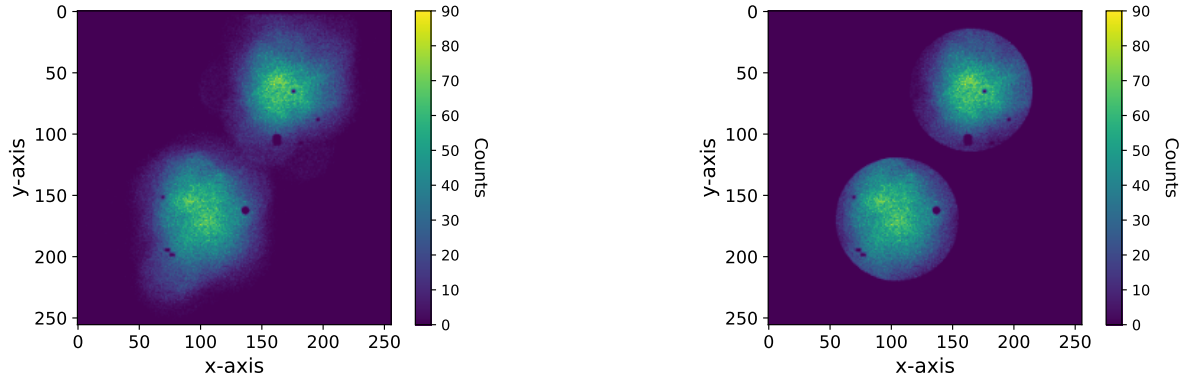

(a) No mask (b) Masked

Figure 4.9: Image of the detector surface showing measured α-particles from a collimated (L/D=2.5) small droplet (2µL) of ^{225}Ac on two different positions. Here the effect of the mask is demonstrated and only counts within 50 pixels of the centre are used. (a) shows the image without the mask and (b) shows the image with the mask. The black dots in the figure on the left are due to faulty pixels, which are pixels that are dead or of which no calibration could be made.

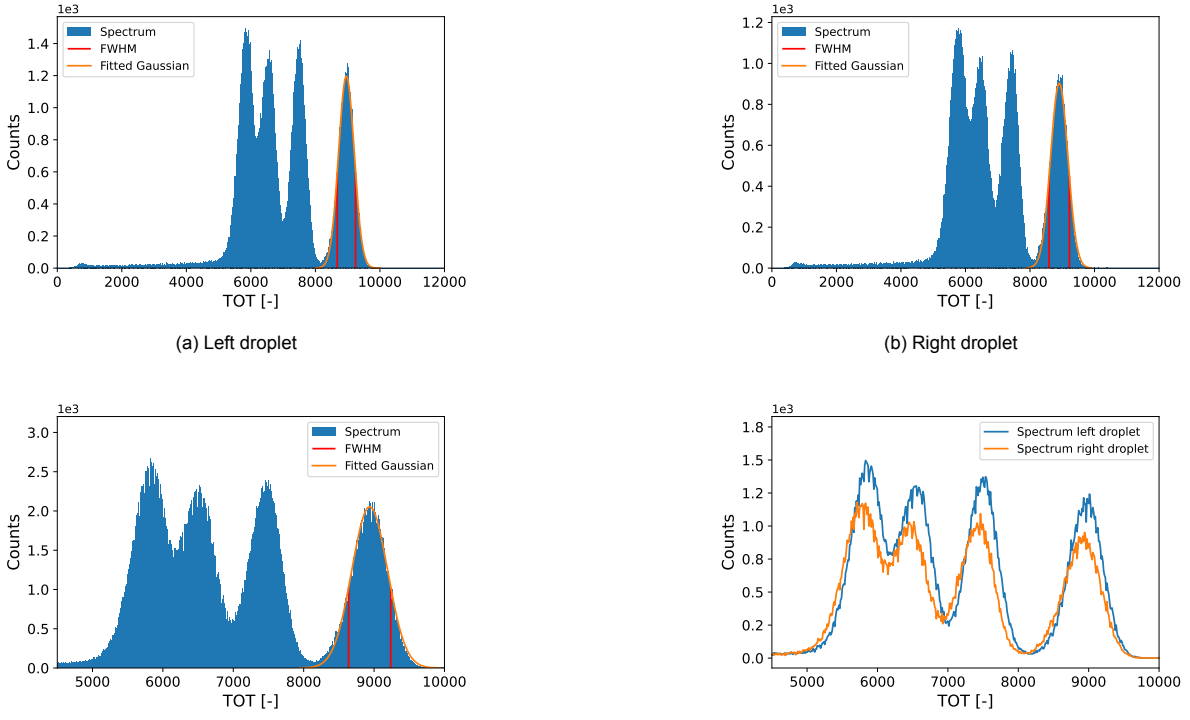

(a) Left droplet (b) Right droplet

(c) Droplets combined (d) Droplets separate

Figure 4.10: The resulting α spectra for a collimated (L/D=2.5) small droplet (2µL) of ^{225}Ac on two different positions without calibration. (a) and (b) show the spectra of the left and right droplets, respectively. These spectra are combined in (c) and shown on top of each other in (d). The threshold was set to 2.01keV and the bias voltage to 30V.

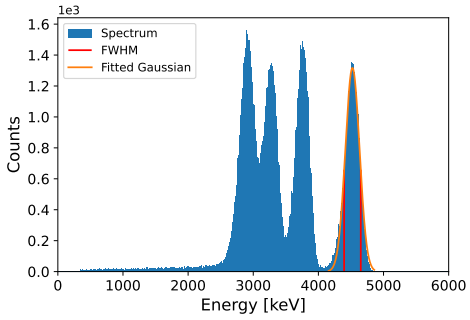

(a) Left droplet

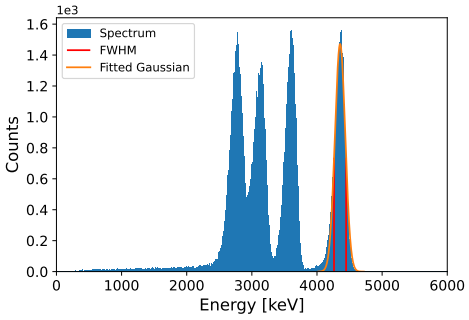

(b) Right droplet

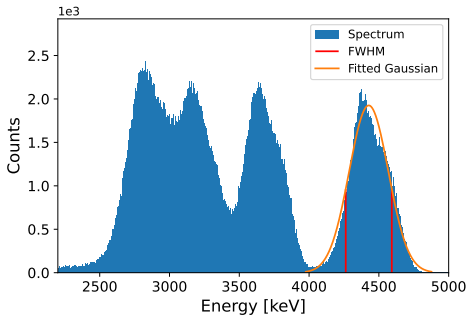

(c) Droplets combined

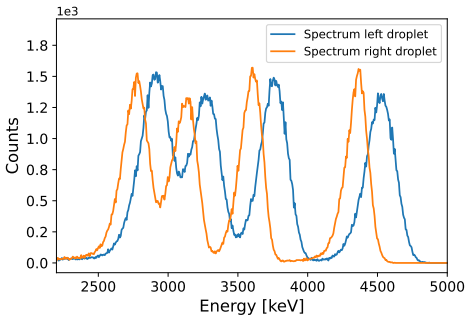

(d) Droplets separate

Figure 4.11: The resulting α spectra for a collimated (L/D=2.5) small droplet (2µL) of ^{225}Ac on two different positions with γ calibration 1. (a) and (b) show the spectra of the left and right droplets, respectively. These spectra are combined in (c) and shown on top of each other in (d). The threshold was set to 2.01keV and the bias voltage to 30V.

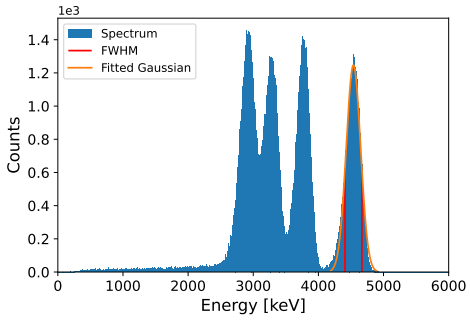

(a) Left droplet

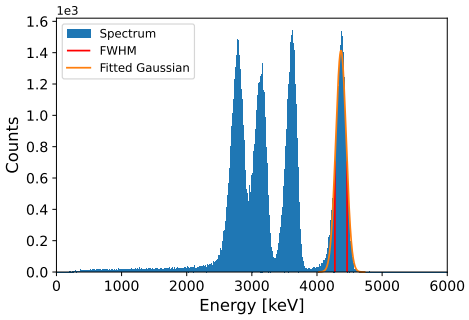

(b) Right droplet

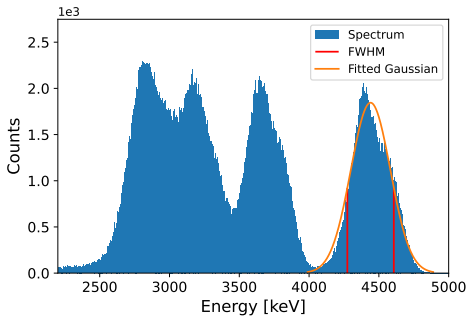

(c) Droplets combined

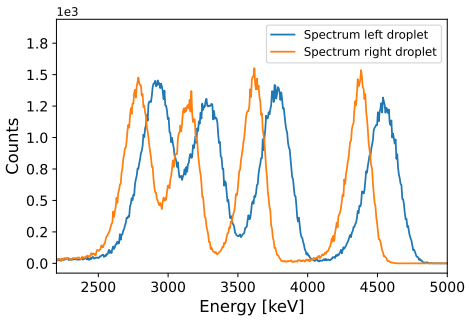

(d) Droplets separate

Figure 4.12: The resulting α spectra for a collimated (L/D=2.5) small droplet (2µL) of ^{225}Ac on two different positions with γ calibration 2. (a) and (b) show the spectra of the left and right droplets, respectively. These spectra are combined in (c) and shown on top of each other in (d). The threshold was set to 2.01keV and the bias voltage to 30V.

The decrease in energy resolution when combining the two droplets is caused by the shift in peak positions after calibration. This effect is demonstrated clearly in the fourth image of Figures 4.11 and 4.12. This diminished the improvement in resolution gained by the γ calibration, though is still within the 5-10% found in literature. This raised the question if the γ calibration was performed correctly. Not only could it be that the γ calibration was performed incorrectly, but the Timepix detector was also placed in the neutron beam at the TU Delft Reactor Institute and also in the proton beam at HollandPTC in Delft, potentially causing damage to the Timepix chip. This was the reason why the γ calibration was performed a second time, using better fitting functions and an improved processing code. However, as can be seen from all previous validations, both calibrations gave almost identical results. This leads to the conclusion that the γ calibration was performed correctly and no damage was done to the Timepix detector in the meantime. This could indeed mean that small errors produced by the γ calibration are magnified due to the large extrapolation. However, the best result attained for a small droplet was an energy resolution of 4.27±0.06% achieved with a relatively rough 3D-printed plastic collimator and the energy resolution locally was in all cases much better. Therefore, it is still possible to measure the α spectrum with a high energy resolution on a local scale. Using a more finely grated collimator might even improve this resolution further. This could still have some applications, however, for this research the goal was to use the Timepix to measure a distribution of nuclides, requiring the whole detector surface to be usable. Hence, in order to measure the α spectrum with high resolution the γ calibration is going to be used and improved on with an α calibration in the next experiment. Finally, the decision was made to use the first γ calibration to improve on and to use in further experiments. The results were very similar, with the second calibration having slightly better energy resolutions. However, the second calibration has twice the amount of unusable pixels, which is very unfavourable when making images with the Timepix.

4.1.3. Alpha calibration

4.1.3.1 Calibration with Am-241 and test on its alpha spectrum

The α spectrum of ^{241}Am was determined using a collimated (L/D=4) source, which was translated over the whole detector surface. From this the average response for the α peak of ^{241}Am was determined for each of the pixels of the detector surface before and after γ calibration, which is given in Figure 4.13. Also, the determined peak values for each pixel using the two α calibration methods, using averaging small sections and based on the average blob shape, are given in the same figure.[2] The average blob shape, the weighting factor, was determined by averaging all measured α 's and is given in Figure 4.14. Finally, the determined spectrum before and after γ calibration and for both methods of α calibration are given in Figure 4.15. For simplicity, the energy to calibrate the spectrum to was taken as 1800keV, which was close to the average measured α energy of ^{241}Am. The results of the fitted peak centre and determined energy resolution are given in Table 4.4.

In Figure 4.13 the average pixel response shows a distinct pattern over the detector surface. The pattern is visible and similar in all cases. This time, the γ calibration only increased the energy resolution slightly compared to processing without calibration, from 19.76±0.05% to 19.61±0.1%. Both α calibrations increased the energy resolution significantly compared to the previous options to 11.85±0.05% and 11.97±0.05%. The centre of the peaks is also close to the set value of 1800keV after calibration, 1802.9±0.3keV and 1803.1±0.3keV respectively.

The average pixel response on the detector surface clearly demonstrates that there is a difference in response on the surface. In the uncalibrated case, it causes a deviation of approximately 27%, which causes the decrease in energy resolution due to non-uniformity of detected energy response as seen in earlier results. Even though the local resolution increased with the γ calibration, this still variation in response on the detector surface is still present, but clearly not caused by this calibration method. This effect only seems to become visible for higher energies, since the γ spectrum of ^{241}Am looked normal. The detector surface response of both methods of α calibration look very similar and more blurry that the previous responses. This is due to the fact that both approaches are a method of averaging, which

[2] A reminder: The 'based on average' method is the method where a spectrum is determined based on a 5x5 square on the detector chip and the α peak is fitted and the centre value is saved to those 5x5 pixels. The 'based on Gaussian' method also used a 5x5 square but saved the fitted value with weights based on the average blob shape shown in Figure 4.14.

Table 4.4: Results of the α calibration with ^{241}Am. Here the fitted centre position of the measured 5485keV α peak and the energy resolution is shown for different calibrations [5].

	No Calibration	γ Calibration	α Calibration	
			Based on Average	Based on Gaussian
μ [keV]	N/a	1733.5±0.7	1802.9±0.3	1803.1±0.3
E_{res} [%]	19.76±0.05	19.61±0.1	11.85±0.05	11.97±0.05

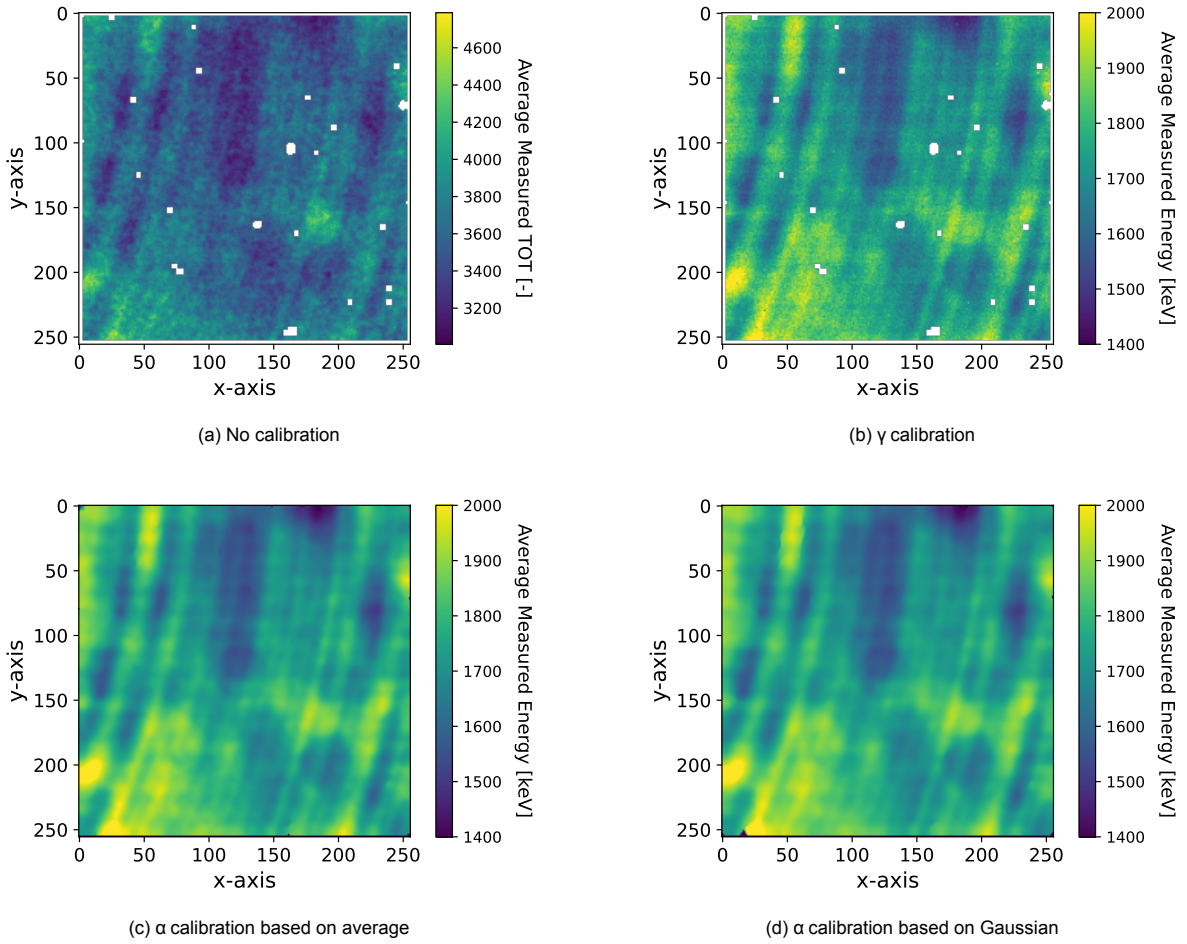

(a) No calibration

(b) γ calibration

(c) α calibration based on average

(d) α calibration based on Gaussian

Figure 4.13: Average detector responses for the measured α spectrum of ^{241}Am for different calibration types. Without calibration is shown in (a), the previously chosen γ calibration in (b) and both α calibrations are shown in (c) and (d), which are the average method and the Gaussian method, respectively. The threshold was set to 2.01keV and the bias voltage to 30V.

was essential due to the low amount of α hits. The faulty pixels are not present in these responses also due to the fact that the surface is averaged, however, this does not matter since the faulty pixels are filtered out in the processing code. Both α calibration methods were then tested and improved the energy resolution significantly. This is mainly due to the fact that all pixels are now corrected and shift the spectrum to the same position (centre at 1800keV). There was no clear better option when comparing both. Unfortunately, the resolution was still quite poor, though this can result from the overall setup used. In order to test the α calibration it is tested on ^{225}Ac data from a previous experiment, which will be shown hereafter.

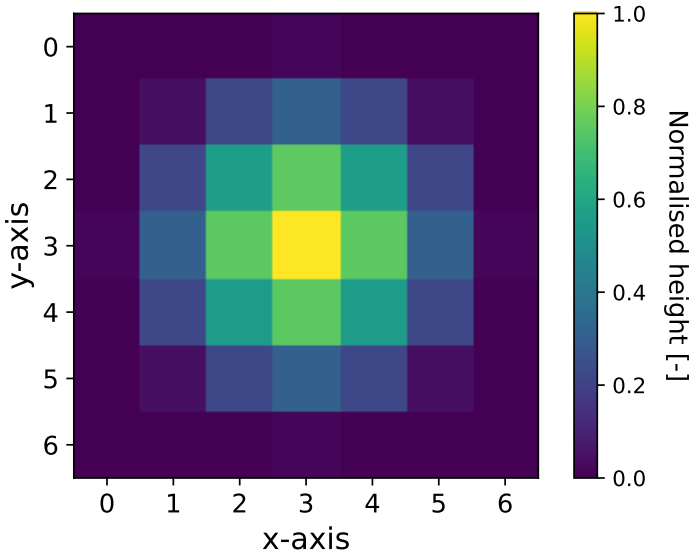

Figure 4.14: The average measured cluster shape for the ^{241}Am calibration measurement. This average shape was determined by averaging all measured clusters. This was done with a threshold of 2.01keV and a bias voltage of 30V. No calibration was used.

4.1.3.2 Small Ac-225 droplet on different positions with alpha calibration

Both α calibration methods were tested on the same experiment data as in section 3.3.1: a collimated (L/D=2.5) small droplet (2µL) of ^{225}Ac on two different positions of the detector surface. Again for both methods, four figures are made: the spectra of the individual droplets, the combined spectrum and the spectra overlapping in one single figure. It is shown for the averaging and Gaussian method in Figures 4.16 and 4.17 respectively. A summary of the results (^{213}Po peak position and energy resolution) is given in Table 4.5.

Table 4.5: Results of the α calibration verification with the α spectrum of a collimated (L/D=2.5) small droplet (2µL) of ^{225}Ac measured at two different positions. Here the fitted centre position of the 8376keV α peak and the energy resolution is shown for the two individual droplets and combined.

	α Calibration Based on Average			α Calibration Based on Gaussian		
	Left	Right	Combined	Left	Right	Combined
μ [keV]	4438±2	4421±1	4425±1	4437±2	4419±1	4424±1
E_{res} [%]	7.3±0.2	5.01±0.05	6.52±0.05	7.2±0.2	4.96±0.06	6.45±0.05

The left and right peak positions of both α calibration methods are closer together than with the γ calibration. The distance with the γ calibration between the peaks was approximately 170keV and was now reduced to 17keV and 18keV for the average and Gaussian methods respectively. For both methods, the resolution of the individual droplets decreased, however, when combined, the resolution improved from 7.5±0.1% to 6.52±0.05% and 6.45±0.05%, which is also better than the uncalibrated case, which was 6.70±0.05%. For both methods, a distortion in the Gaussian shape of the ^{213}Po peak occurred in the left droplet.

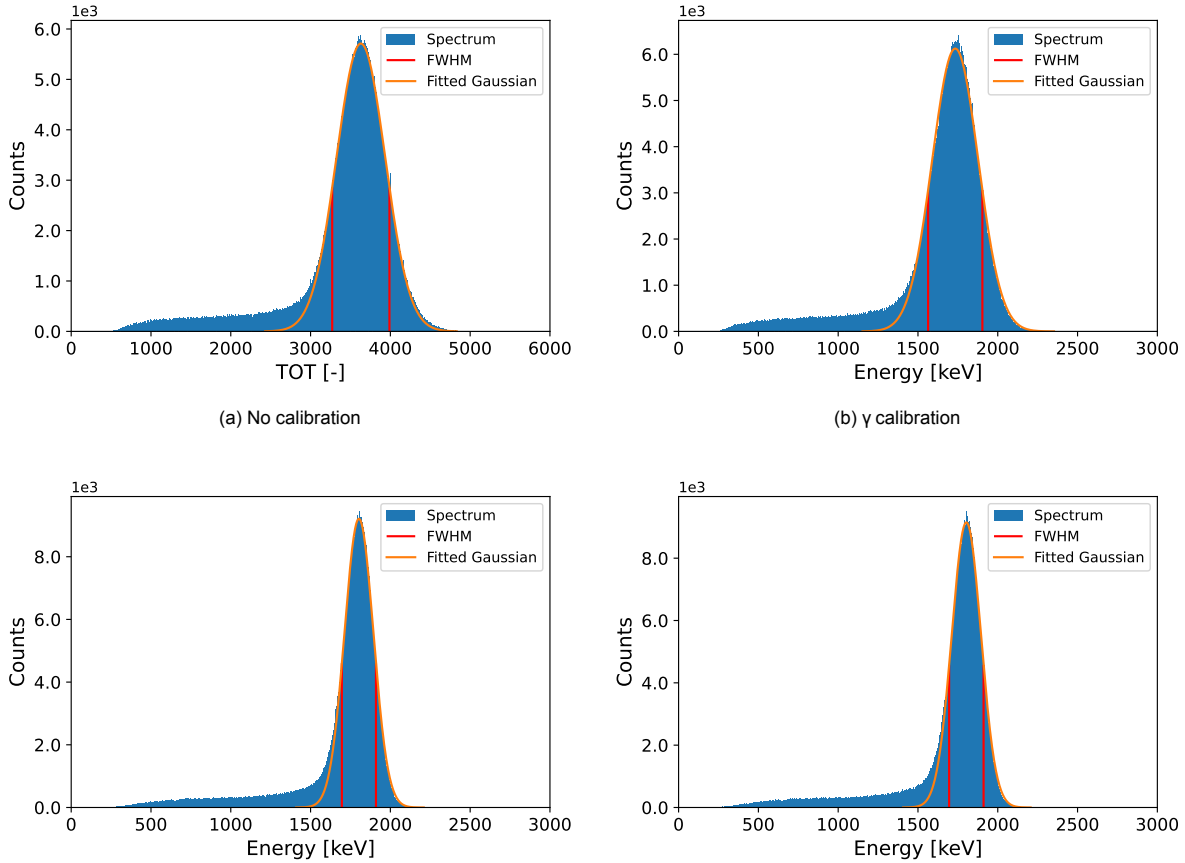

(a) No calibration

(b) γ calibration

(c) α calibration based on average

(d) α calibration based on Gaussian

Figure 4.15: α spectra of a collimated (L/D=4) 33kBq ^{241}Am source for different calibrations. In (a) the spectrum is uncalibrated, in (b) the previously chosen γ calibration is used and both α calibrations are shown in (c) and (d), which are the average method and the Gaussian method, respectively. The threshold was set to 2.01keV and the bias voltage to 30V.

Overall, the α calibration results are good, though not perfect. The α calibration did do what it was supposed to do, homogenising the detector response for α-particles. This is indicated by the spectrum being shifted in energy and resulting in a higher energy resolution. Therefore, it improved the energy resolution when doing a measurement on different positions of the detector and allows for measurements using the whole detector surface. However, this is at a cost of resolution on the local scale, since the resolution on the individual droplets decreased. It even distorted the peaks of the left droplet slightly. Therefore, it should always be considered for each experiment if the γ or α calibration is used. Between the two α calibration methods the choice was made to use the Gaussian weighting method since this had a better energy resolution when combining both droplets. This method will be used for all the following experiments. The next experiment will determine if the α calibrations indeed improve the resolution of the α spectrum when using the whole detector surface.

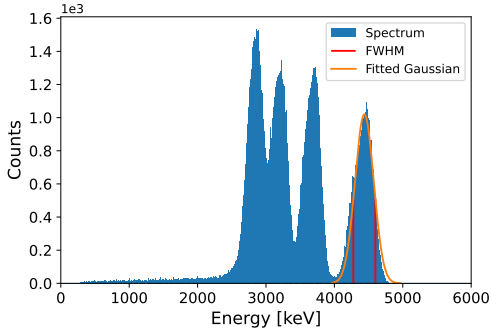

(a) Left droplet

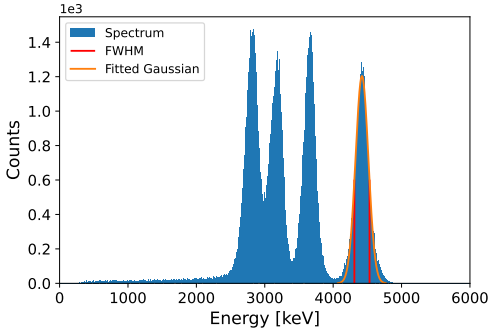

(b) Right droplet

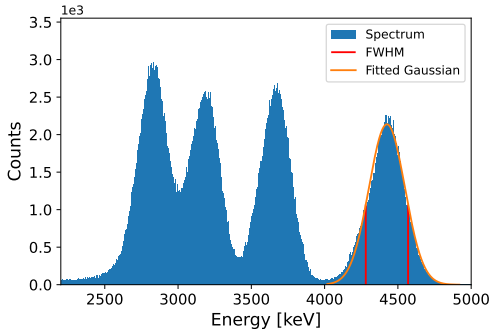

(c) Combined droplets

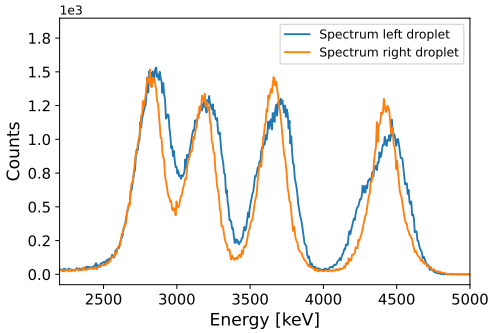

(d) Separate droplets

Figure 4.16: The resulting α spectra for a collimated (L/D=2.5) small droplet (2µL) of ^{225}Ac on two different positions with the α calibration based on averaging. (a) and (b) show the spectra of the left and right droplets, respectively. These spectra are combined in (c) and shown on top of each other in (d). The threshold was set to 2.01keV and the bias voltage to 30V.

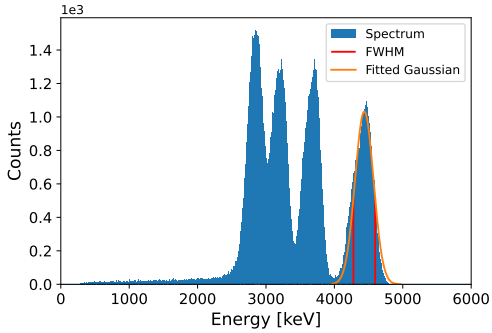

(a) Left droplet

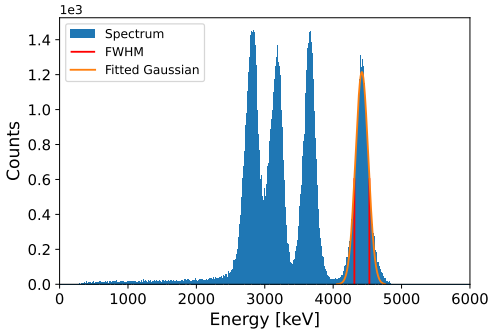

(b) Right droplet

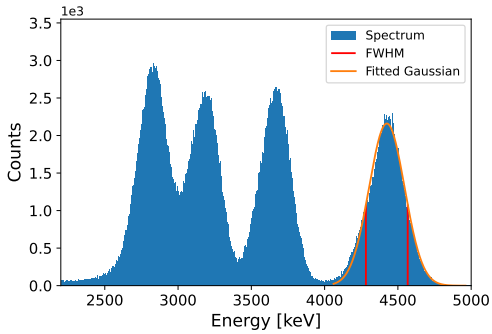

(c) Combined droplets

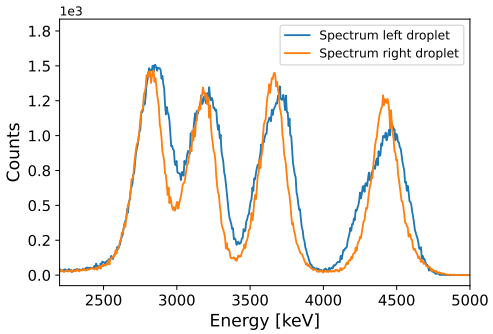

(d) Separate droplets

Figure 4.17: The resulting α spectra for a collimated (L/D=2.5) small droplet (2µL) of ^{225}Ac on two different positions with the α calibration based on the Gaussian. (a) and (b) show the spectra of the left and right droplets, respectively. These spectra are combined in (c) and shown on top of each other in (d). The threshold was set to 2.01keV and the bias voltage to 30V.

4.1.4. Energy resolution of different Collimators using the whole detector surface

The measurements using the plastic collimator and the lead-glass collimator were processed without calibration, with the γ calibration and with the α calibration. The resulting spectra are given in Figures 4.18 and 4.19. The energy resolution could not be determined for all cases, due to deformations of the Gaussian peak or peaks being indistinguishable. For some, an estimate could be made based on the width at full maximum by determining it manually. These results are given in Table 4.6.

Table 4.6: Results of the whole surface ^{225}Ac α measurement using different collimators, plastic (L/D=2.5) and lead-glass (L/D=50), and different calibrations. Here the fitted centre position of the 8376keV α peak and the energy resolution is shown. (Notations: c.n.b.d. = could not be determined, *=approximation.)

	Plastic Collimator			Lead-glass Collimator		
	No calibration	γ calibration	α calibration	No calibration	γ calibration	α calibration
E_{res} [%]	15.7±0.3	11.9*	9.6±0.1	c.n.b.d.	13.5*	12.6±0.4

For both the plastic collimator and the lead-glass collimator the resolution of the spectrum increased each time for each type of calibration. When using no calibration the peaks of the α spectrum are broad and difficult to distinguish. After performing the γ calibration the resolution increased, though a splitting of the peaks was observed. In both cases a Gaussian could therefore not be fitted, thus an estimation was made for the energy resolution. Finally, the α calibration removed the splitting of the peaks and made the response of the detector surface more uniform, increasing the energy resolution once again in both cases. In all cases of the lead-glass collimator, the Gaussian peaks were very broadly tailed and a large peak at around 500keV was observed. The best-obtained resolution in this experiment was when using the plastic collimator in combination with the α calibration, which was 9.6±0.1%.

This experiment highlights the significance of prior calibration steps. Without calibration, the detector cannot generate an α spectrum of ^{225}Ac that accurately distinguishes all four α peaks when utilising the entire detector surface and a collimator. Performing the γ calibration substantially enhances the resolution, but it also raises the previously discussed issue of non-uniform detector response, resulting in spectrum displacement at different positions on the detector surface. Consequently, the α calibration was necessary to address this problem, albeit at the expense of energy resolution. This becomes evident from the narrower split peaks achieved through the γ calibration compared to the α calibration. When fitting a Gaussian to the second small ^{213}Po peak, the resolution obtained was 6.99±0.04% for the plastic collimator and 5.1±0.5% for the lead-glass collimator. These values are significantly better than the resolution obtained through the α calibration. This indicates that further improvements can still be made to the calibration process. While the plastic collimator exhibited well-defined Gaussian peaks, the lead-glass collimator showed Gaussian peaks with broad tails. Several factors could contribute to this phenomenon. It is possible that α-particles, due to the small walls (approximately 20µm), are not completely stopped since their projected range in ρ=8g/cm^3 Pb-transparent glass is 16.75 µm [20]. However, the small angles at which the α-particles traverse the collimator walls result in a much greater vertical distance travelled through the material than the α distance in lead-glass. It is also possible that α-particles graze the edge of the collimator wall, though this is a very small fraction and could not cause such broadening of peaks. Another possibility is energy loss due to small-angle scattering, particularly Rutherford scattering, which is dominant for low energies, high Z materials, and small angles. It is possible that when an α-particle loses energy after travelling a short distance in the material, it is scattered back passing through the collimator holes. However, the probability of this happening without being counteracted by low-angle scattering of other nuclides in the collimator material is extremely low [83]. It is also plausible that α-particles exhibit interactions when encountering a different medium, although this cannot be concluded based on this single experiment and further experiments are necessary to investigate this phenomenon. The prominent low-energy peak observed in the lead-glass collimator spectrum is caused by β-particles emitted by the daughters of ^{225}Ac, which easily traverse through the

collimator. The processing code still makes some errors by misidentifying β-particles as α-particles, a scenario that is only visible in this case due to the overwhelming number of β-particles compared to practically shielded α-particles. Therefore, these errors become more apparent. It was confirmed that the peak was indeed caused by β-particles, by using the same setup and shielding the α-particles with a 1mm thick slab of plastic. The resulting β-spectrum was similar. Although not problematic in normal situations, these errors should still be rectified by determining why these particles are being identified as α-particles. In their current state of calibration and setup, neither collimator is suitable for imaging ^{225}Ac and its daughter nuclides in tissue samples since not all α peaks can be fully distinguished in terms of energy. In the case of the plastic collimator, only the peaks of ^{225}Ac and ^{221}Fr overlap, which may still provide some information about the distribution. However, it should be noted that in a 5µm tissue slice, there is energy loss, leading to peak broadening. Consequently leading to a spectrum where all peaks overlap, thus an improvement in energy resolution is recommended. If the energy resolution can be extended to reach 5%, as observed in local measurements with the γ calibration, or even lower through improved calibration or the use of a finer collimator that does not induce the Gaussian peak tailing seen for lead-glass, it should certainly be possible to image α emitters in tissue slices.

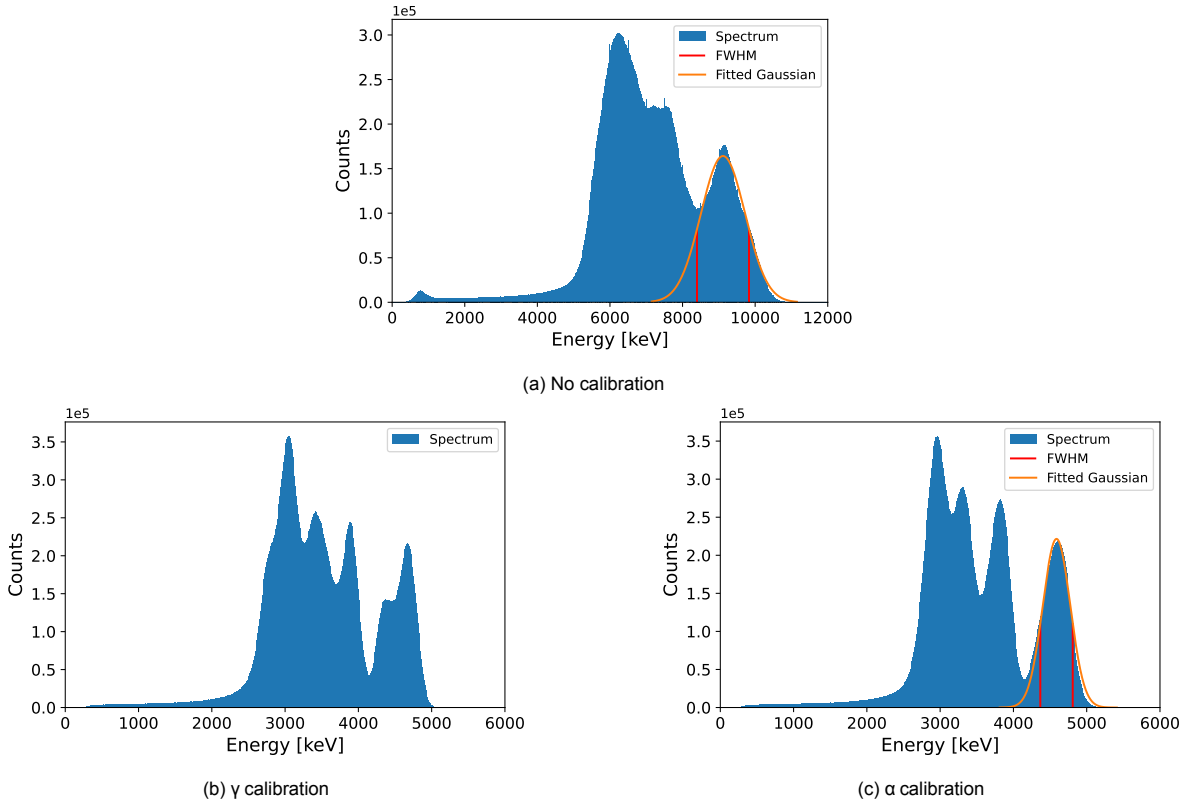

Figure 4.18: The resulting α spectra for the whole surface measurement of ^{225}Ac using the plastic collimator (L/D=2.5). Here the different calibrations are compared. (a) shows the spectrum without calibration, (b) with the γ calibration and (c) with the α calibration. The threshold was set to 2.01keV and the bias voltage to 30V.

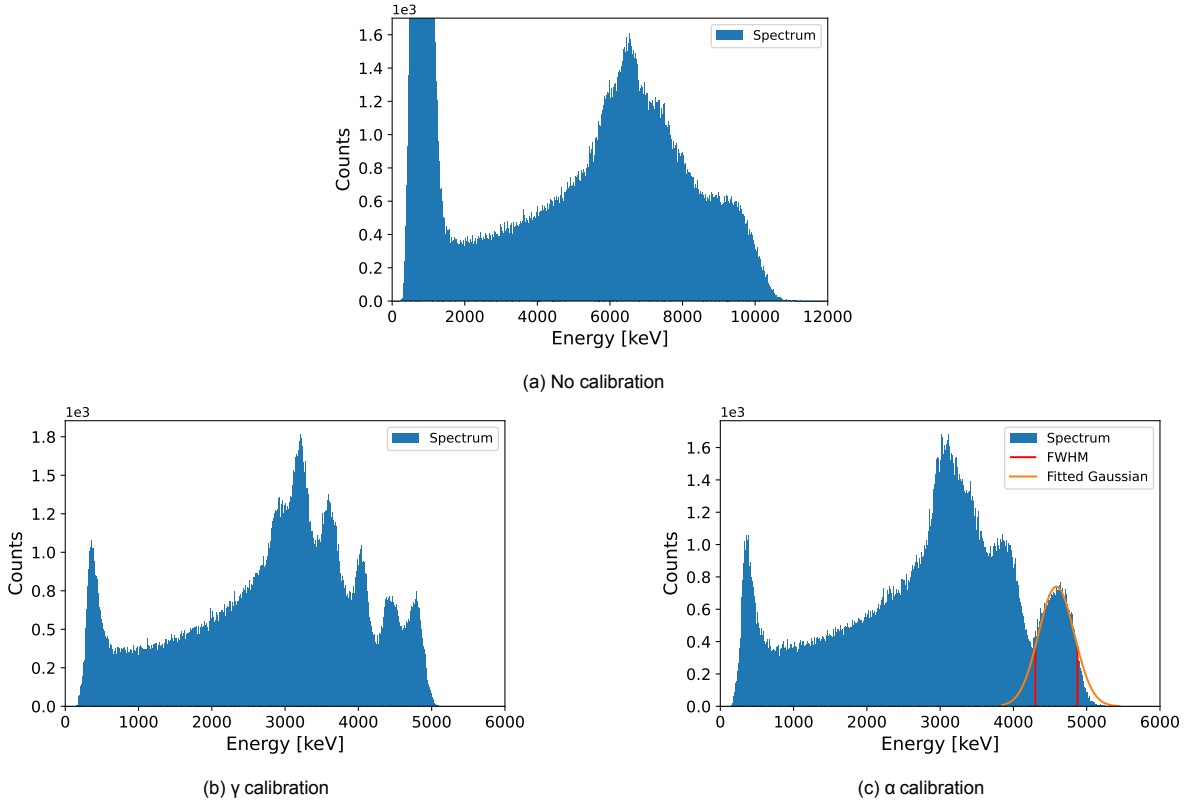

Figure 4.19: The resulting α spectra for the whole surface measurement of ^{225}Ac using the lead-glass collimator (L/D=50). Here the different calibrations are compared. (a) shows the spectrum without calibration, (b) with the γ calibration and (c) with the α calibration. The threshold was set to 2.01keV and the bias voltage to 30V.

4.1.5. Spatial resolution of plastic collimator

The data of the spatial resolution measurement with the plastic collimator (L/D=2.5) was processed using the α calibration. A single collimator hole was taken for the determination of the spatial resolution, which is shown in Figure 4.20. A perpendicular line of width 10µm was defined and moved with steps of 10µm. From this, the LSF was determined, which is shown in Figure 4.21. For the plastic collimator with holes of 1mm and an L/D ratio of 2.5, the determined spatial resolution was: 310±10µm.

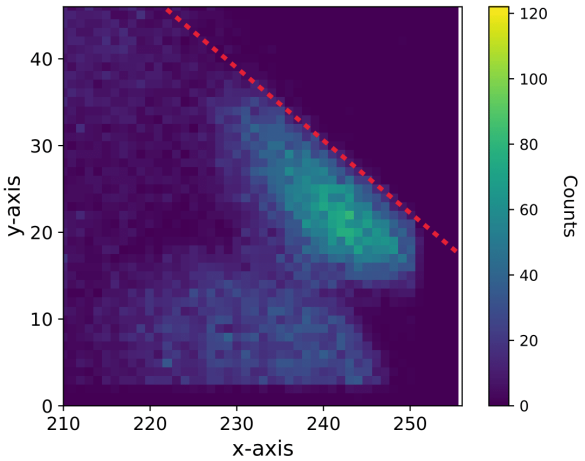

Figure 4.20: A zoomed image from the Timepix detector measuring ^{225}Ac with a plastic collimator (L/D=2.5) and a sharply defined edge from a thick microscopic glass. The direction of the edge is indicated with the red dashed line.

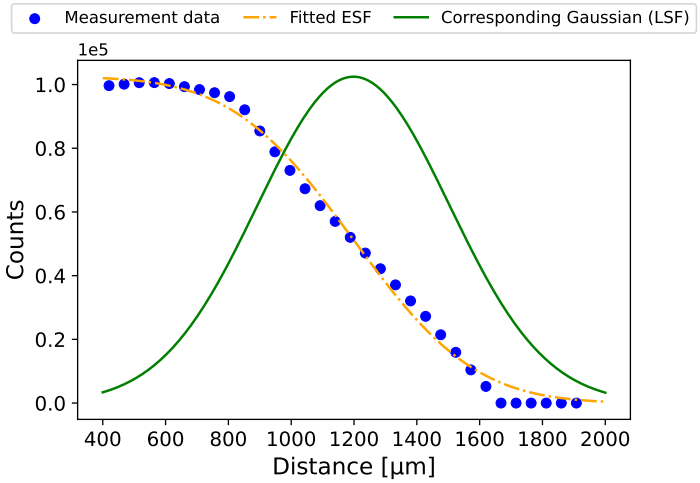

Figure 4.21: The resulting counts at different distances from the well-defined edge of the microscopic glass using a plastic collimator with an L/D of 2.5. The 0 distance point was arbitrarily chosen before the edge. The edge spread function (ESF) is fitted and a line spread function (LSF) is derived.

The resolution of 310±10µm is quite good for the rough holes of the plastic collimator, although it might not be good enough if the goal is to measure tissue samples. The L/D ratio should therefore be increased. Also, it was quite difficult to find a region where a proper ESF could be fitted, due to the non-homogeneity of the sample. This caused a non-stable start of the ESF, which can also be seen in 4.21. Ideally, a larger section should be taken.

4.1.6. HPLC measurement Ac225-PSMA

The measurement data was processed using the α calibration. Figure 4.22 shows the measured α spectrum of a cumulative of 5 minutes at 5-minute intervals. At each time interval, a Gaussian fit was made on the ^{213}Po peak to determine the amount of α-particles emitted by ^{213}Po. This is shown in Figure 4.23.

Even though the spectrum is not of a high resolution and low in counts, the spectrum at intervals clearly shows that the ^{213}Po peak is much smaller than the rest of the peaks and that it increases in intensity as time passes. This is also visible in Figure 4.23, where the growth appears to be linear. The peak of ^{217}At also appears to slowly increase in size.

Considering that the preparation of the sample took around 5 minutes. This behaviour is expected in a situation where ^{225}Ac is separated from its daughters as it is very similar to the simulated situation in section A.2, where both ^{221}Fr and ^{217}At increase to around 50% of the ^{225}Ac activity in 5 minutes and slowly reach equilibrium around 20 minutes. In the experimental data, the peak of ^{225}Ac also appears to slightly increase, which is probably due to the fact that ^{225}Ac and ^{221}Fr are overlapping and ^{221}Fr is increasing in activity. The growth of ^{213}Po is linear in the experiment, which is also the case for the simulation when measuring on this timescale. The low resolution was due to the fact that the droplet of the sample was moving due to the high temperature of the pre-heated glass plate. This spread in activity was also observed in the image made from the data. A second measurement with a smaller droplet and lower pre-heat temperature would increase the resolution of the spectrum and would be beneficial for characterising the behaviour of the nuclides. These results indicate that it could be possible to separate ^{225}Ac-PSMA from the daughters also linked to PSMA.

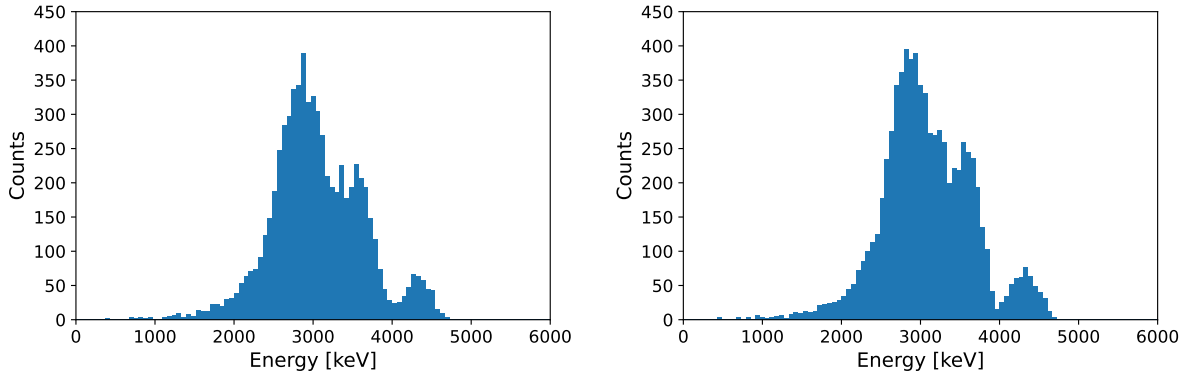

(a) 0-5 minutes

(b) 5-10 minutes

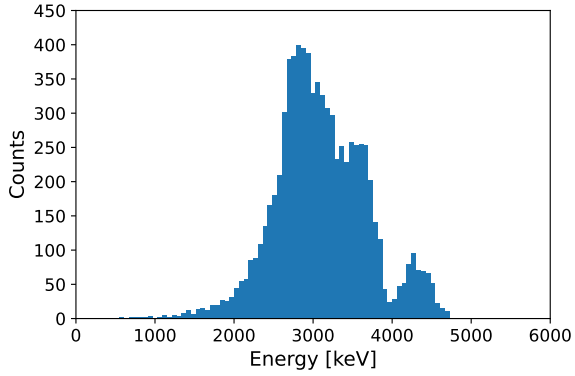

(c) 10-15 minutes

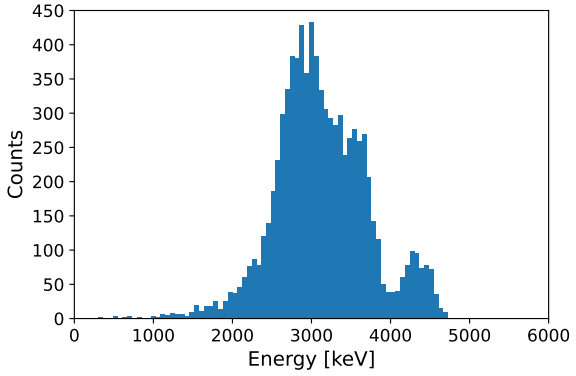

(d) 15-20 minutes

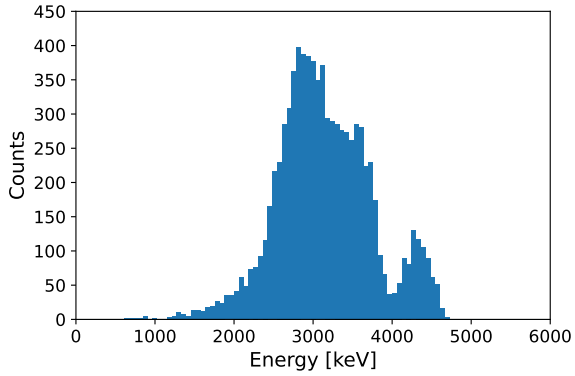

(e) 20-25minutes

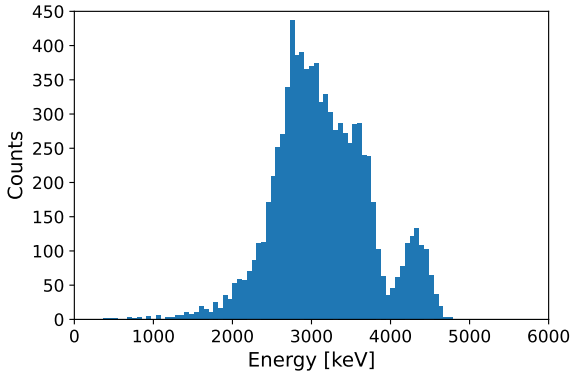

(f) 25-30 minutes

Figure 4.22: The measured α spectra of the HPLC fraction measurement containing ^{225}Ac and daughters at different integrated 5-minute time intervals, shown in (a)-(f), respectively. In this case, the α calibration was used, the threshold was set to 2.01keV and the bias voltage to 30V.

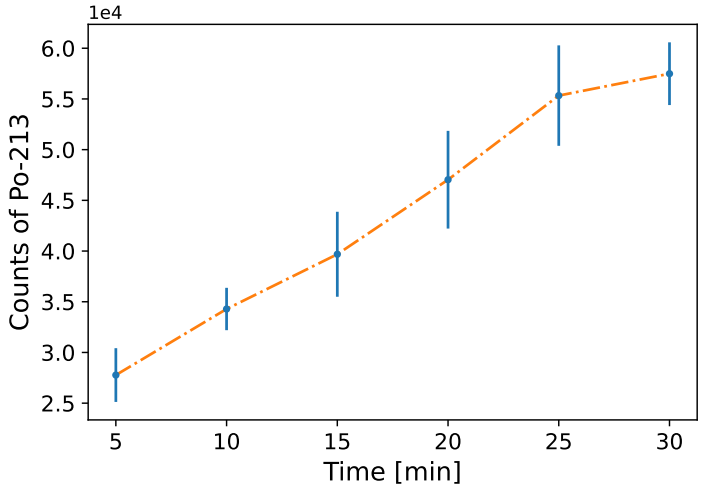

Figure 4.23: Fitted ^{213}Po peak over different 5-minute integrated intervals from the HPLC fraction measurement.

4.1.7. HPTC proton beam measurements

The measurements were processed using the α calibration and all types of detected radiation were included in the resulting spectra. The results are shown in Figures 4.24 and 4.25 for the 70MeV (pencil beam) and 120Mev (flat field beam) measurements respectively. The resulting spectra of the measurements with the Silicon wafer are shown in Figure 4.26.

For the measurements with the 70MeV protons, the following observations were made from the spectra:

- 0mm RW3: Two peaks are visible around 20keV and 60keV.
- 34mm RW3: A high peak around 0keV and a small broad bump at 430keV.
- 36mm RW3: A high peak around 0keV and a small broad bump at 430keV.
- 38mm RW3: Only a high peak around 0kev.
- 39mm RW3: A high peak around 0keV, a peak around 70keV and a small broad bump at 2000keV (not visible in Figure 4.24, but shown in Figure A.3).
- 40mm RW3: Two peaks visible at 20keV and 60keV.

For the measurements with the 120MeV protons, the following observations were made from the spectra:

- 0mm RW3: Two peaks are visible around 20keV and 230keV.
- 98mm RW3: Only a high peak around 0kev.

Finally, for the measurements with 70MeV on a Silicon wafer and the Timepix detector at two different distances from the wafer, the following observations were made from the spectra:

- 16mm: Two peaks are visible around 20keV and 520keV.
- 50mm: A high peak around 0keV is visible with some bumps in the data for higher energies, which are not distinguishable as peaks.

Many of the conducted experiments resulted in an overflow of the Timepix detector, which seemed to have an impact on the results in a way that is not yet fully understood. However, several observations were made regarding this overflow. Firstly, it was noted that the data appeared to be improperly sorted based on the Time of Arrival, thereby making the processing more challenging. Additionally, it was observed that certain pixel data might have been omitted during these overflow instances, consequently influencing the overall particle energy. This occurrence could potentially account for the significant peak observed at 0 keV in certain measurements. The first setup used a pencil beam geometry at 2nA,

which was the lowest possible intensity. Consequently, the second setup was configured with a flat field geometry. Unfortunately, the Timepix also encountered an overflow in this setup. Therefore, at the moment, the Timepix3 is not suitable for beam verification. Its successor, the Timepix4, might be more suitable for these types of measurements, as it is expected to have a processing ability of 720Mhits/s instead of 80Mhits/s [84].

Furthermore, the 20keV visible in some of the measurements might have been noise due to secondary particles or the small energy deposition of very high energy protons, due to the fact that the 20keV peak is only visible in measurements with 0mm RW3. However, these measurements are with different energies and the 0mm RW3 measurement for 70MeV protons also has a very pronounced 60keV peak, which is not visible in other measurements. This 20keV peak was also not visible in the background measurement. Therefore, it is probably due to the creation of secondary particles.

For the 70MeV measurement, the deposited energy due to protons was initially very low, increasing in energy for thicker RW3 and peaking at 2000keV for 39mm RW3. The energy diminished again for 40mm RW3, accompanied by a much lower count of detected particles. Interestingly, no peak was visible for 38mm RW3. This absence might be the result of the overflow or could be due to the energy deposition being too high, causing the volcano effect. In general, the observed effect in energy and intensity is comparable to scanning through the proton energies and changing the linear energy transfer. This effect is shown figuratively in Figure 4.27.

In the 120MeV measurement, two peaks were again observed at 0mm RW3. However, this time the second peak had higher energy than the one observed at 0mm RW3 for 70MeV protons. This is unexpected since a proton should deposit less energy at higher energies. It might be again due to the overflow of the Timepix, which might have a lesser effect in a flat field beam. However, at this point, no definitive conclusions can be drawn from the energy spectra of the measurements due to the overflow.

The Silicon wafer measurements suggest a similar phenomenon. When the Timepix was placed at 16mm, an overflow occurred, most likely because the Timepix was positioned inside the proton beam. At 50mm, the measurement was nominal, and a broad peak around 520keV became visible. This peak could be attributed to scattered protons or a very small part of the Timepix still being in the proton beam but producing counts below the maximal processing rate. The spectrum looks similar to protons measured under an angle with the Timepix from literature, shown in Figure A.4 [85].

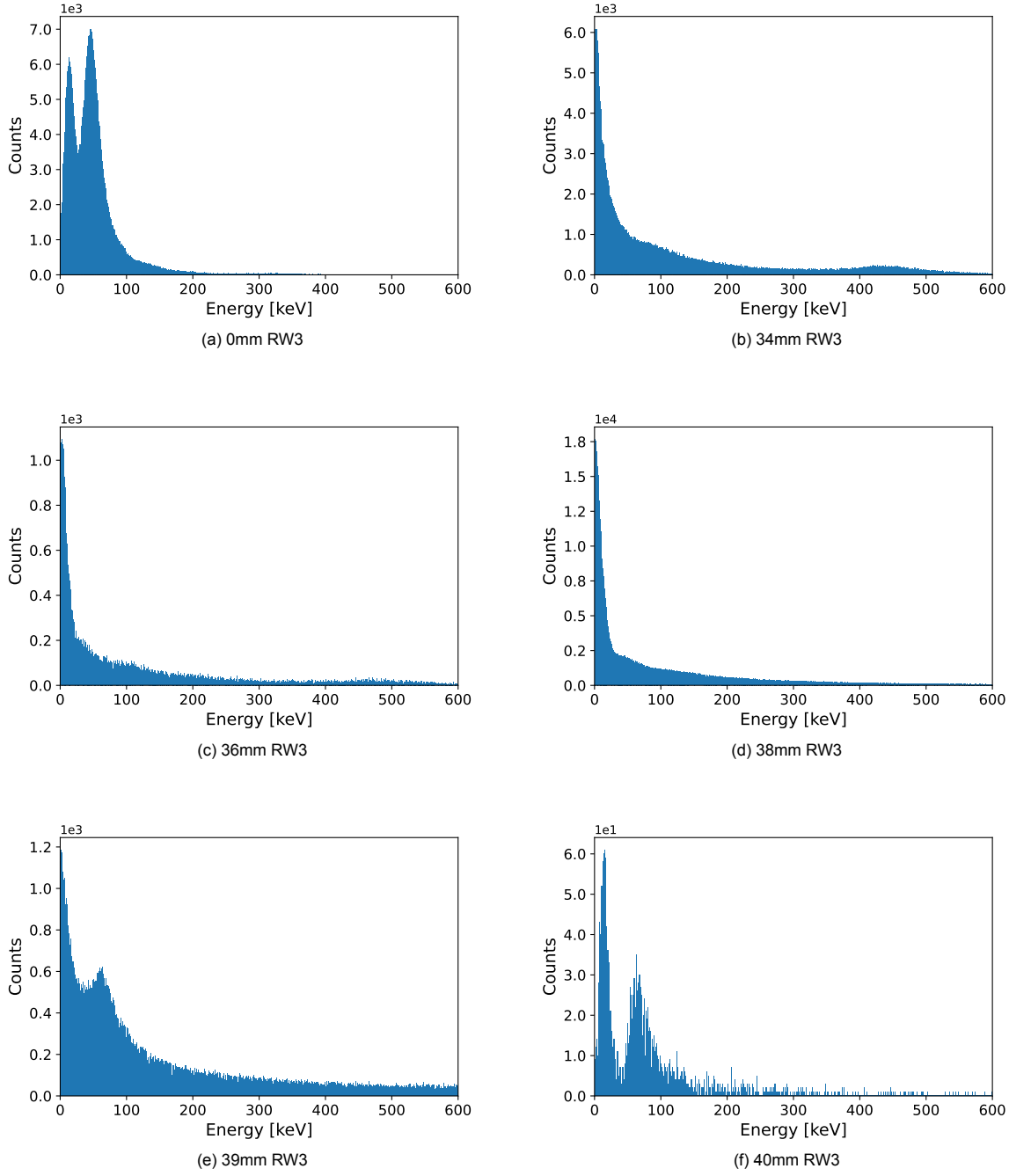

Figure 4.24: Measured energy spectrum of the 70MeV proton beam measurement with 2nA intensity and pencil beam geometry for different thicknesses of RW3, shown in (a)-(f), where the proton beam was aimed at the Timepix chip. The α calibration was used, the threshold was set to 2.01keV and the bias voltage to 30V.

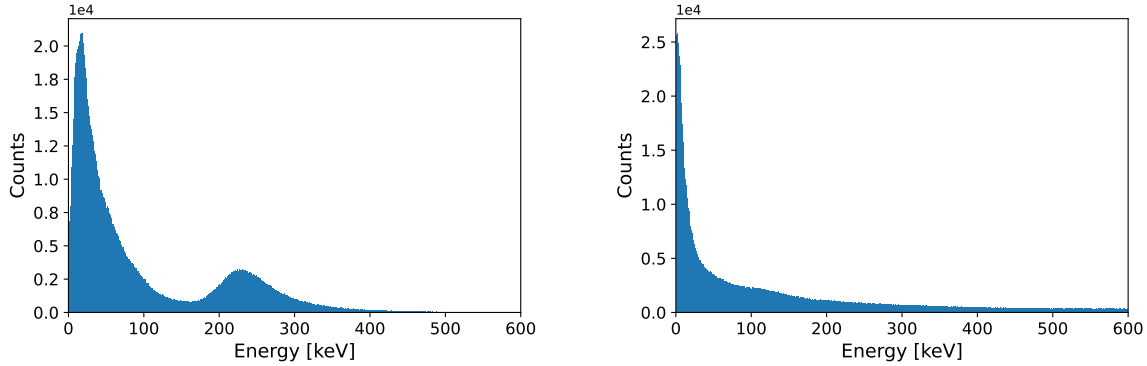

(a) 0mm RW3 (b) 98mm RW3

Figure 4.25: Measured energy spectrum of the 120MeV proton beam measurement with 5nA intensity and broad beam geometry for different thicknesses of RW3, shown in (a) and (b), where the proton beam was aimed at the Timepix chip. The α calibration was used, the threshold was set to 2.01keV and the bias voltage to 30V.

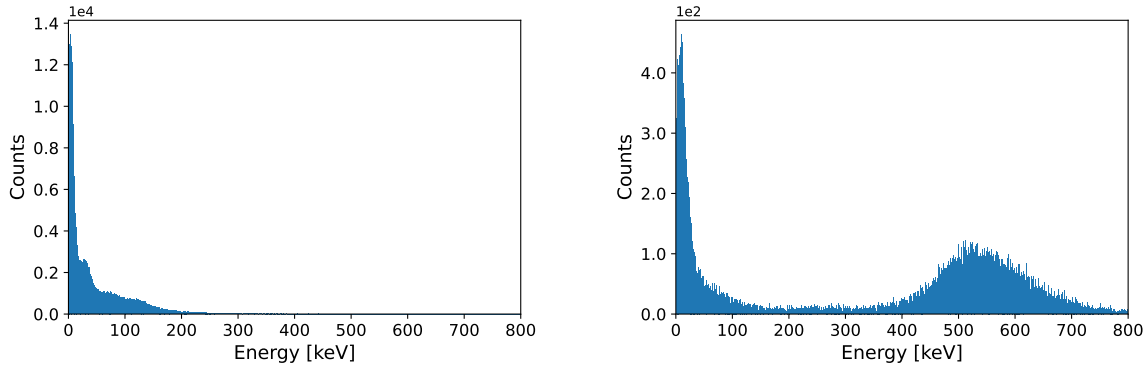

(a) 16mm (b) 50mm

Figure 4.26: Measured energy spectrum of the 70MeV proton beam measurement with 2nA intensity and pencil beam geometry where the proton beam was aimed at a Si wafer and the Timepix at different distances from the wafer, shown in (a) and (b). The α calibration was used, the threshold was set to 2.01keV and the bias voltage to 30V.

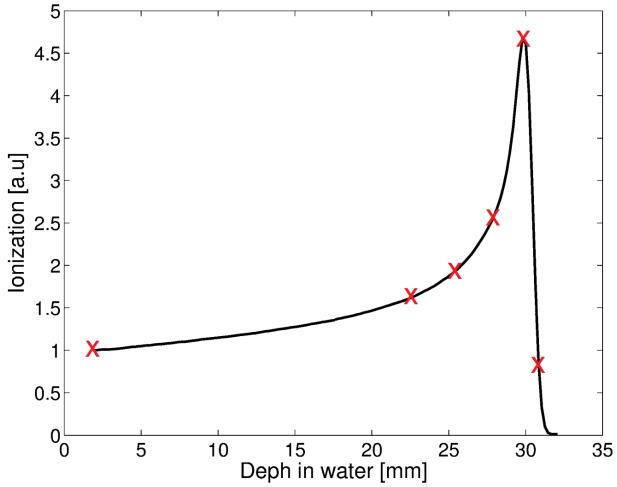

Figure 4.27: The Bragg curve of 62MeV protons in water where the result of different thicknesses of RW3 is shown with red crosses schematically, indicating different stopping powers at different depths of RW3 [86].

4.2. Discussion & Recommendations

4.2.1. General discussion

Initially, the Timepix was not calibrated and the optimal bias voltage setting was unknown. The bias voltage is crucial in measuring high-energy heavy charged particles as it prevents the volcano effect, which distorts the measured particles. Therefore, this was the first experiment which was performed. In this experiment the spectrum of a droplet of ^{225}Ac was measured at different bias voltages. At lower bias voltages, the count rate was low, and it was not possible to distinguish the α peaks of ^{225}Ac and its daughters. As the bias voltages increased, the volcano effect started to occur, resulting in a blurry and unusable spectrum. Eventually, there was a range of suitable bias voltages, of which 30V was chosen due to it being the single highest voltage setting before the volcano effect occurred.

Then the Timepix needed to be calibrated. For each pixel hit, it produced values that indicated how long the received signal was above a set threshold level. Not only did this not fully correspond to physical energy values, but the pixels themselves were also biased and not uniform in response. This was due to the pixels being individually amplified. Traditionally, the Timepix can be calibrated per pixel by using low-energy γ sources, which have a single-pixel response. For this research, ^{57}Co, ^{133}Ba, and ^{241}Am calibration sources were used. For these, six γ peaks could be fitted with a Gaussian. This calibration was performed twice for validity and to confirm no damage was done to the Timepix since some unwanted effects occurred during the γ calibration. Both γ calibration methods were tested in different situations: the ^{241}Am γ spectrum, the ^{225}Ac droplet, and the two identical ^{225}Ac droplets in different positions. The improvement that the γ calibration made was quite significant. In the case of the ^{241}Am γ spectrum, the energy resolution improved from 24.0±0.4% to 4.1±0.2% in the single-hit case and from 21.9±0.3% to 4.23±0.09%. Therefore, the Timepix is able to measure low-energy γ with high resolution. Then it was tested on an ^{225}Ac droplet to measure the α spectrum. Here it was clear that the Timepix is able to image α-particles and determine their energy spectrum, as four α peaks were visible, as expected. Unfortunately, the measured energy was about half of the expected energy. However, this does not influence the ability to measure the ^{225}Ac α spectrum and distinguish the nuclides. The improvement in energy was less significant, though still impressive, going from 6.13±0.06% to 4.46±0.04%. Finally, when measuring the two identical droplets of ^{225}Ac in different positions on the detector surface, the results showed that the γ calibration was not fully successful in homogenising the detector response. The two droplets had translated peak positions, making the combined energy resolution worse than without calibration. It even showed that without calibration, the peak positions of both droplets were the same. However, this might have been a coincidence. Nevertheless, the γ calibration was able to produce a very high-resolution α spectrum at a local scale but was not suitable at this stage to measure the spectrum for the whole detector surface. It was also concluded that both γ calibrations were identical, and these errors were not caused by damage to the Timepix or errors in the calibration method. It might simply be that the calibration, even though supposedly linear in this region, cannot be extended to such high energies (100x) as errors in the calibration are also magnified. Therefore, a second calibration method was developed using α-particles to be used on top of the γ calibration.

This calibration was based on measuring α-particles from ^{241}Am, which was a smoke detector source collimated with an L/D of 4 and a hole diameter of 0.5mm. This was done to make the source as homogeneous as possible. It was then translated over the detector surface using a translation table. The calibration method itself relied on determining the variation of response for the same α-particle energy of the whole detector surface. The responses were determined by averaging small sections or using the average blob shape, which turned out to be a symmetric 2D Gaussian, as a weighting factor to distribute the measured energy to neighbouring pixels. This was due to the fact that the α-particle patterns were not the size of single pixels but delivered their energy to multiple pixels in a cluster and because the number of hits was quite low. From the calibration, it became clear that there was indeed a variation on the chip since the average measured energy caused a pattern with a variation of approximately 27% on the chip instead of being homogeneous, which was not caused by the γ calibration since the pattern was the same when using the unprocessed data. It was also clear that the γ calibration was not able to correct this variation because the pattern was still apparent. Using the information about the variation in energy of each of the pixels for alpha particles, a correction could be made by scaling this variation based on the measured energy value and adding it to the measured value. It was again tested

on a few test cases: the ^{241}Am α spectrum and again the small droplet (2µL) of ^{225}Ac on two different positions. When measuring the α spectrum of ^{241}Am there was a clear improvement from 19.61±0.1% (γ calibration) to 11.97±0.05% in energy resolution and the average measured energy (1803.1±0.3keV) became close to the target energy, which was 1800keV. This was due to the fact that at each position on the detector surface, the response was much more homogeneous due to the α calibration. It was noted that the resulting energy resolution was still on the low side, about 7% higher than previously achieved, though this may be the result of the overall setup. Then a more practical situation was tested, which was previously also tested with only the γ calibration in order to test if the α calibration has helped. This was the small droplet (2µL) of ^{225}Ac on two different positions. Here it was observed that the measured centre positions of the ^{213}Po energy value were now the same for both left and right droplets, which increased the energy resolution when combined slightly from 7.5±0.1% (γ calibration) to 6.45±0.05. This is also lower than the uncalibrated combined case, 6.70±0.05%. Unfortunately, the energy resolution of the droplets separately decreased slightly. This is a necessary trade-off to improve whole surface resolution, though it indicates that there is still some room for improvement. The α calibration was then tested in a situation which might be similar to measuring a tissue sample, which is a whole surface ^{225}Ac measurement. This was done using two different collimators in order to also determine which is a more suitable method for imaging α emitting nuclides. Here a full comparison was made for using no calibration, γ calibration and finally α calibration. These results made the importance of each of the performed calibrations very clear. Each step of calibration increased the overall energy resolution for both collimators. The increase was from 15.7±0.3% (no calibration) to 9.6±0.1% (α calibration) in the case of the plastic collimator. For the lead-glass collimator, a resolution could not be determined when not using a calibration. When using the γ calibration it was estimated to be 13.5% and it increased to 12.6±0.4% when using the α calibration. It was noted that the peaks were split in both cases when using a γ calibration, which was corrected when using the α calibration. However, when determining the energy resolution of one of the smaller peaks it was much better than the α calibration: 6.99±0.04% and 5.1±0.5% for the plastic collimator and lead-glass collimator respectively. Therefore, it was concluded that again a higher resolution seems to be possible when all peaks are perfectly centred after α calibration, which is not yet the case. The spectrum with the lead-glass collimator had a large-tailed peak of which the origin cause is not yet known. The walls might be too thin or scattering occurs at such small angles, though further research is necessary. Both collimators at this stage of calibration were not suitable for imaging and correctly identifying ^{225}Ac and its daughters. Further improvement of the calibration or different collimators was suggested. Still, other applications are possible at this stage, which are later discussed.

Finally, the spatial resolution of the Timepix detector was determined. This could only be done for the rough plastic collimator with an L/D ratio of 2.5. This was due to the fact that the ^{225}Ac had decayed from 30kBq to 300Bq. The spread of ^{225}Ac on the sample holder was not homogeneous since multiple small droplets were used to create a large spread of ^{225}Ac. This made determining the spatial resolution more difficult. However, when zoomed in to a single collimator hole the spatial resolution was determined to be 310±10µm. This itself is quite good for the 1mm holes of the collimator. For the initial application, imaging tissue samples with ^{225}Ac might not be sufficient. Other research found better spatial resolutions, which are easily achievable by using collimators with higher L/D ratios [10].

Being able to determine the α spectrum of a sample, the Timepix is an ideal candidate to perform experiments with ^{225}Ac. Currently, the radio-pharmaceutical ^{225}Ac-PSMA is tested on purity by separating labelled PSMA and unbound nuclides using an HPLC and measuring the γ count of ^{221}Fr. This is currently done with an equilibrium of ^{225}Ac and ^{221}Fr, which is achieved after around 30 minutes, and it also does not give direct information about the different nuclides in the resulting sample [13]. It was tested which nuclides were present in the resulting fraction from the HPLC with the highest remaining γ count. The results showed that initially only ^{225}Ac, ^{221}Fr some ^{217}At and a small amount of ^{213}Po was present. The spectra were not of very high resolution due to the droplet spreading on the sample holder caused by too much pre-heating, however, the results were clear enough to determine the amount of ^{213}Po over time. A graph was made showing the amount of ^{213}Po over 30 minutes in 5-minute intervals, which showed a linear increase and a doubling in the amount of activity of ^{213}Po in 30 minutes. These observations were very similar to a simulation of the activities of the different nuclides in a situation where no daughters are initially present. Therefore, it seems that the HPLC is able to not only separate

based on unbound and bound nuclides but also to separate the different nuclides. The Timepix could also be used for other experiments with the radio-pharmaceutical or quality assessment.

Finally, the Timepix was used for experiments with the proton beam from HollandPTC. These experiments were conducted to see if the Timepix3 is able to determine the shape and energy of the proton beam in order to do beam verification. The Timepix was placed inside the proton beam with different beam geometries, energies and intensities moderated by different thicknesses of RW3 slabs. It was also placed next to the beam hitting a Si wafer to image scattering of protons or secondary particles. Unfortunately, the Timepix encountered overflows in practically every situation due to proton intensities being too high. This caused errors in the measurement including unsorted ToA data and split ToT information. The processing code was also not able to fully distinguish different particles due to new geometries and the before-mentioned issues with the data. The data was therefore processed with no distinction between particles. Even though the data was very noisy and contained errors, there seemed to be a pattern in measured energy corresponding to scanning the Bragg curve. Also in the measurement of the Si wafer with the Timepix at a 5cm distance, an energy peak was observed which was similar to literature where protons were measured under an angle. Therefore, it seems that the Timepix3 is not able to do beam verification, though its successor the Timepix4 might be. The Timepix3 is currently able to measure the scattering of protons since the intensity is much lower, which was seen in the Si wafer experiment.

4.2.2. Recommendations

Now some recommendations will be given on what might be improved or what might be done for further research. First the improvements.

Even though the γ calibration seems to have been performed successfully, yielding a high energy resolution locally, there were still errors that needed to be resolved with the α calibration. Additionally, some pixels could not be calibrated. To improve the calibration process, a greater number of hits from the nuclides should be gathered to improve the spectrum that will be fitted. Furthermore, in this research, only six peaks were fitted, which can be improved by incorporating more low-energy γ-emitting nuclides or by utilising X-ray fluorescence (XRF). These measures should enhance the accuracy of the fitted centre positions of the γ peaks and the resulting linear fit. Increasing the count rate also reduces the number of pixels that cannot be calibrated, bringing it closer to the number of truly dead pixels, estimated to be around 20.

Hopefully, an improved γ calibration will reduce the errors encountered when measuring the energy of α-particles and further enhance the resolution. However, an α calibration is still expected to be necessary. In this research, the α calibration was performed in a quite short time, as it was performed in the last two weeks of experimentation, and certain compromises were made. The only available α source was the ^{241}Am source found in a smoke detector. Consequently, the calibration was based on the deviation of this single α energy. Undoubtedly, it would be much more desirable to have different sources, such as ^{244}Cm, ^{238}Pu, or ^{239}Pu, in order to create a varying correction factor [5]. Additionally, conducting the calibration in a vacuum would result in better-defined Gaussian peaks, as there would be no energy loss. The measurement time (1 week) was relatively short, combined with the activity of the source, to obtain sufficient counts in each pixel. Therefore, a collimator with a low L/D ratio was chosen, which led to less defined energy peaks of the α-particles. Even after making these compromises, the count rate per pixel was very low, making it difficult to accurately fit Gaussian curves to the energy peaks. Thus, it is recommended to increase the source activity or measurement time and use a collimator with a higher L/D ratio. Implementing these recommendations should result in a better calibration and improved resolution for different α energies. Lastly, 52x52 steps were taken with the translation table. Although finer steps could be taken, the spread in α-particles was already larger than 5 pixels, making it unnecessary. However, implementing finer steps would not be too difficult.

An attempt was made to calibrate the Timepix with ^{225}Ac, which emits multiple well-defined α-particles and is an ideal candidate for alpha calibration. However, during the calibration process, it became clear that there was a slight deviation in the measured energy on the sample holder, which was not caused by the detector. It appears that the emitted energy on the sample holder is not uniform and

the ^{225}Ac calibration was stopped. This also raises the question of whether the sample holders used for experimentation were suitable in this particular situation. Ideally, a sample made of electroplated ^{225}Ac would be preferable, although it is a more challenging goal to achieve. Electroplating involves the deposition of a very thin and evenly distributed layer of ^{225}Ac and its daughter nuclides [87]. Such a sample could be utilised for calibration purposes, and other experiments could also benefit from it.

In terms of further research, the following suggestions are proposed:

1. Improve both calibrations as mentioned earlier, potentially with ^{225}Ac.
2. Test different materials and L/D ratios for collimators to determine the optimal setup for imaging the distribution of ^{225}Ac and its daughters in tissue samples. In this research, only two collimators were tested for energy resolution. This could potentially also answer the question of the origin of the tailed α peaks, measured in the lead-glass collimator experiment.
3. Determine spatial resolution by using different collimators with a more homogeneously distributed source, such as electroplating, compared to the non-homogeneous distribution of ^{225}Ac used in the current study. Previous research achieved a spatial resolution of 10µm using an older version of the Timepix, which should be achievable with the Timepix3 and is ideal for imaging nuclide distributions in tissue samples [10].
4. Image two different α-emitting nuclides that are not mixed to assess the Timepix's ability to accurately distinguish between different nuclides. For instance, coat two microscopic glasses (or electroplate a metal) with different nuclides and position them close to each other to examine their distinguishability. Other experiments mixing different nuclides in a controlled manner are also possible.
5. In order to mimic the transmission of α-particles from a tissue sample. Layers of Mylar could be placed on the sample holder with ^{225}Ac in between each layer (dried). This could give a good indication of the resulting spectrum from a tissue sample.
6. Repeat the experiment at Erasmus with HPLC fractions, expanding the study to different fractions and improving the setup to determine the composition of different nuclides in each fraction.
7. Use the Timepix for research and development at the proton beam facility. While not primarily for beam verification at this stage, the Timepix can be valuable for imaging secondary particles or proton scattering and serve other purposes.

5

Conclusion

5.1. Main research

The main goal of this research was to assess the ability of the Timepix3 detector to image the distribution of ^{225}Ac and its daughter nuclides in a tissue sample treated with Targeted Alpha Therapy. To achieve this, a data analysis code was developed to process the output data from the Timepix and extract information regarding the type, energy, and position of detected particles. The code for this data analysis is provided in Appendix A.5.

Next, the ideal bias voltage needed to be determined. Lower bias voltages rendered the measured energies indistinguishable, while higher voltages introduced the volcano effect, distorting the measured energy. After measuring ^{225}Ac using different bias voltages, the ideal bias voltage was found to be 30V.

Two calibration steps were then performed. The first calibration was the γ calibration. This method used low energy γ radiation, which induces single-pixel hits on the detector surface allowing for per-pixel calibration. This is necessary since each of the Timepix pixels is individually amplified and needs to be homogenised in order to increase the energy resolution of the whole detector surface. Three different sources were used ^{57}Co, ^{133}Ba and ^{241}Am of which six γ peaks were fitted. Notably, the best energy resolution of 4.46±0.04% was achieved when measuring a 2µL droplet of 360Bq ^{225}Ac without a collimator. In this situation, the energy resolution was determined by measuring the FWHM of the ^{213}Po α peak, which is the most distant from the other α peaks. The energy resolution was found to be 4.46±0.04%. This is better than the 5-10% found in literature and the 14% in previous research [11][10]. The measured energy, however, was significantly lower than the theoretical value, though when characterised, this can be corrected. Unfortunately, this energy resolution was only achieved on a local scale since the response of the detector was still not uniform everywhere. This non-uniformity was determined by measuring the same droplet of ^{225}Ac at two different positions. Since the γ calibration itself was executed correctly, as validated by performing it twice, a second calibration was required to address the response deviation observed. This second calibration was the α calibration.

An α calibration was performed using a ^{241}Am α source. It was collimated with a plastic collimator with an L/D ratio of 4 to create a tiny source. This source was then scanned over the surface of the Timepix detector in order to measure identical energies at each pixel position. Based on the average measured energy a correction factor was created for each pixel. This α calibration increased the energy resolution from 7.5±0.1% to 6.45±0.05%. More importantly, the α calibration was successful in homogenising the detector response in order to use the whole detector surface. This was shown by measuring a spread-out source of ^{225}Ac using two different collimators. A plastic collimator and a lead-glass collimator with L/D ratios of 2.5 and 50 respectively. The lead-glass collimator was not able to create a usable spectrum of ^{225}Ac due to the tailing of the Gaussian peaks of which the true cause is not yet known. However, the plastic collimator was able to create an α spectrum of ^{225}Ac with a resolution of 9.6±0.1%. It was noted that the α calibration was successful, though at a cost of energy resolution since the resolution was significantly lower than the best-achieved resolution of 4.46±0.04%. There are still some

improvements to be made to increase the energy resolution for the whole detector to that resolution.

For the plastic collimator, the spatial resolution was determined using the same setup as the energy resolution measurement. Even though it was difficult due to the non-homogeneous spreading of ^{225}Ac on the sample holder, a spatial resolution of 310±10µm was attained.

Is the Timepix3 detector able to image the distribution of ^{225}Ac and daughter nuclides in a tissue sample treated with Targeted Alpha Therapy? When considering the energy resolution at this stage of calibration together with the used collimators, it would not be possible to properly distinguish the nuclides. However, when the calibration is improved in order to increase the energy resolution on the whole surface together with a better collimator, the resolution could increase above 4.46±0.04% and be sufficient for these types of measurements. When using the plastic collimator a spatial resolution of 310±10µm was attained, which is already very good considering the collimator holes were 1mm, though also not yet sufficient. Increasing the L/D ratio would improve the spatial resolution further, to sub-pixel resolution [10]. If these improvements are made, the Timepix3 detector would certainly be able to be used to image the distribution of ^{225}Ac and daughter nuclides.

5.2. Related side projects

Then, two other types of research were conducted using the Timepix detector. The first one investigated if the Timepix is suitable for measurements with the radio-pharmaceutical ^{225}Ac-PSMA, as it has the advantage of being able to quickly measure α particles. An experiment was performed to measure a fraction of PSMA labelled with ^{225}Ac from an HPLC to identify the number of different nuclides in the sample. The measurement showed that initially, there was very little ^{213}Po present in the fraction, which linearly increased over time, doubling in number within 30 minutes. This behaviour was compared to a simulation where initially only ^{225}Ac was present, and it was found to be comparable. Therefore, it was concluded that the HPLC is able to separate compounds labelled with different nuclides, and the Timepix could be an interesting tool for direct measurements on α emitting radio-pharmaceutical samples, instead of indirect measurements like γ spectroscopy.

Finally, multiple experiments were conducted with the proton beam at HPTC to investigate if the Timepix could be used for beam verification and imaging secondaries. Unfortunately, in multiple measurements with different beam geometries and intensities, the Timepix was in overflow, resulting in distortion of measurement data. However, it was observed that within the data, certain patterns could be recognised. When attenuating the proton beam with RW3 material, the deposited energy in the Timepix detector increased and abruptly stopped after a certain thickness of RW3, corresponding to different points on the Bragg curve. Furthermore, when measuring the proton beam hitting a Si wafer, scattered protons were successfully detected. At this stage, the Timepix3 detector would not be suitable for beam verification, but it could be used for imaging scattered protons or secondaries. The successor, the Timepix4, might be more suitable for beam verification.

Bibliography

[1] H. Sung et al. “Global Cancer Statistics 2020: GLOBOCAN Estimates of Incidence and Mortality Worldwide for 36 Cancers in 185 Countries”. In: *CA: A Cancer Journal for Clinicians* 71.3 (2021), pp. 209–249. DOI: https://doi.org/10.3322/caac.21660.

[2] L. Sapio and S. Naviglio. “Innovation through Tradition: The Current Challenges in Cancer Treatment”. In: *Int. J. Mol. Sci.* 23.10 (May 2022). DOI: 10.3390/ijms23105296.

[3] K. Young-Seung and M. W. Brechbiel. “An overview of targeted alpha therapy”. In: *Tumor Biology* 33.3 (June 2012), pp. 573–590. ISSN: 1423-0380. DOI: 10.1007/s13277-011-0286-y.

[4] A. Morgenstern et al. “An Overview of Targeted Alpha Therapy with ^{225}Actinium and ^{213}Bismuth”. In: *Current Radiopharmaceuticals* 11.3 (Oct. 2018), pp. 200–208. DOI: https://doi.org/10.2174/1874471011666180502104524.

[5] *Live Chart of Nuclides*. URL: https://www-nds.iaea.org/relnsd/vcharthtml/VChartHTML.html.

[6] *Processes*. [Online; accessed 31. May 2023]. May 2023. URL: https://www.mdpi.com/journal/processes/special_issues/Alpha_Therapy.

[7] M. Roscher, G. Bakos, and M. Benešová. “Atomic Nanogenerators in Targeted Alpha Therapies: Curie’s Legacy in Modern Cancer Management”. In: *Pharmaceuticals* 13.4 (2020). ISSN: 1424-8247. DOI: 10.3390/ph13040076.

[8] J. Fitzsimmons and R. Atcher. “Synthesis and evaluation of a water-soluble polymer to reduce Ac-225 daughter migration”. In: *Journal of Labelled Compounds and Radiopharmaceuticals* 50.2 (2007), pp. 147–153. DOI: 10.1002/jlcr.1143.

[9] *Hybrid Pixel Detectors*. Oct. 2022. URL: https://www.amscins.com/learn-more/technology/.

[10] J. W. J. Hoefsloot. “A performance study to the spatial and energy resolution of a hybrid pixel detector for alpha imaging applications”. PhD thesis. Technical University of Delft, 2022.

[11] A. Tamburrino et al. “Timepix3 detector for measuring radon decay products”. In: *Journal of Instrumentation* 17.06 (June 2022), P06009. DOI: 10.1088/1748-0221/17/06/p06009.

[12] P. A. J. Mendelaar et al. “Defining the dimensions of circulating tumor cells in a large series of breast, prostate, colon, and bladder cancer patients”. In: *Molecular Oncology* 15.1 (2021), pp. 116–125. DOI: https://doi.org/10.1002/1878-0261.12802.

[13] E. L. Hooijman et al. “Development of [225Ac]Ac-PSMA-I&T for Targeted Alpha Therapy According to GMP Guidelines for Treatment of mCRPC”. In: *Pharmaceutics* 13.5 (May 2021), p. 715. ISSN: 1999-4923. DOI: 10.3390/pharmaceutics13050715.

[14] V. Olansk et al. “Proton radiography with the pixel detector Timepix”. In: *Acta Polytechnica CTU Proceedings* 4 (Dec. 2016), pp. 56–61. ISSN: 2336-5382. DOI: 10.14311/AP.2016.4.0056.

[15] P. Stasica et al. “Single proton LET characterization with the Timepix detector and artificial intelligence for advanced proton therapy treatment planning”. In: *Physics in Medicine and Biology* (Apr. 2023). ISSN: 1361-6560. DOI: 10.1088/1361-6560/acc9f8. eprint: 37011632.

[16] R. Nabha et al. “A novel method to assess the incident angle and the LET of protons using a compact single-layer Timepix detector”. In: *Radiation Physics and Chemistry* 199 (Oct. 2022), p. 110349. ISSN: 0969-806X. DOI: 10.1016/j.radphyschem.2022.110349.

[17] J. K. Shultis and R. E Faw. *Fundamentals of nuclear science and engineering*. en. 3rd ed. London, England: CRC Press, Nov. 2016.

[18] A. Eckardt. “Geschwindigkeitsverlust von H-Kanalstrahlen beim Durchgang durch feste Körper”. In: *Annalen der Physik* 397.3 (1930), pp. 401–428. DOI: 10.1002/andp.19303970304.

[19] G. F. Knoll. *Radiation Detection and Measurement*. en. 4th ed. Chichester, England: John Wiley & Sons, Aug. 2010.

[20] J. F. Ziegler, M. D. Ziegler, and J. P. Biersack. “SRIM – The stopping and range of ions in matter (2010)”. In: *Nuclear Instruments and Methods in Physics Research Section B: Beam Interactions with Materials and Atoms* 268.11-12 (June 2010), pp. 1818–1823. DOI: 10.1016/j.nimb.2010.02.091.

[21] S. Seltzer. *Stopping-Powers and Range Tables for Electrons, Protons, and Helium Ions, NIST Standard Reference Database 124*. en. 1993. DOI: 10.18434/T4NC7P.

[22] A. Brown and H. Suit. “The centenary of the discovery of the Bragg peak”. In: *Radiotherapy and Oncology* 73.3 (2004), pp. 265–268. ISSN: 0167-8140. DOI: https://doi.org/10.1016/j.radonc.2004.09.008.

[23] J. H. Lawrence et al. “Alpha and Proton Heavy Particles and the Bragg Peak in Therapy”. In: *Trans. Am. Clin. Climatol. Assoc.* 75 (1964), p. 111. URL: https://www-ncbi-nlm-nih-gov.tudelft.idm.oclc.org/pmc/articles/PMC2279335/.

[24] *Density of Paper, standard in 285 units of density*. [Online; accessed 17. Apr. 2023]. Apr. 2023. URL: https://www.aqua-calc.com/page/density-table/substance/paper-coma-and-blank-standard.

[25] J. C. Johnson and S. Thaul. “Principles of Radiation Protection”. In: *An Evaluation of Radiation Exposure Guidance for Military Operations: Interim Report*. National Academies Press (US), 1997. URL: https://www.ncbi.nlm.nih.gov/books/NBK233830.

[26] L. He et al. “Metastatic castration-resistant prostate cancer: Academic insights and perspectives through bibliometric analysis”. In: *Medicine* 99.15 (Apr. 2020), e19760. DOI: 10.1097/md.0000000000019760.

[27] Mayo Clinic. *Stage 4 prostate cancer*. May 2020. URL: https://www.mayoclinic.org/diseases-conditions/stage-4-prostate-cancer/diagnosis-treatment/drc-20377972.

[28] A. King. “Could immunotherapy finally break through in prostate cancer?” In: *Nature* 609.7927 (Sept. 2022), S42–S44. DOI: 10.1038/d41586-022-02861-y.

[29] D. J. Maggs. “Chapter 3 - Ocular Pharmacology and Therapeutics”. In: *Slatter’s Fundamentals of Veterinary Ophthalmology (Fourth Edition)*. Ed. by D. J. Maggs, P. E. Miller, and R. Ofri. Fourth Edition. Saint Louis: W.B. Saunders, 2008, pp. 33–61. ISBN: 978-0-7216-0561-6. DOI: https://doi.org/10.1016/B978-072160561-6.50006-X.

[30] O. Sartor et al. “Lutetium-177–PSMA-617 for Metastatic Castration-Resistant Prostate Cancer”. In: *New England Journal of Medicine* 385.12 (Sept. 2021), pp. 1091–1103. DOI: 10.1056/nejmoa2107322.

[31] R. M. de Kruijff, H. T. Wolterbeek, and A. G. Denkova. “A Critical Review of Alpha Radionuclide Therapy—How to Deal with Recoiling Daughters?” In: *Pharmaceuticals* 8.2 (2015), pp. 321–336. ISSN: 1424-8247. DOI: 10.3390/ph8020321.

[32] R.M. de Kruijff et al. “Improved ^{225}Ac daughter retention in $InPO_4$ containing polymersomes”. In: *Applied Radiation and Isotopes* 128 (2017), pp. 183–189. ISSN: 0969-8043. DOI: https://doi.org/10.1016/j.apradiso.2017.07.030.

[33] C. Kratochwil et al. “^{225}Ac-PSMA-617 for PSMA-Targeted α-Radiation Therapy of Metastatic Castration-Resistant Prostate Cancer”. In: *Journal of Nuclear Medicine* 57.12 (2016), pp. 1941–1944. ISSN: 0161-5505. DOI: 10.2967/jnumed.116.178673.

[34] B. Feuerecker et al. “Activity and Adverse Events of Actinium-225-PSMA-617 in Advanced Metastatic Castration-resistant Prostate Cancer After Failure of Lutetium-177-PSMA”. In: *European Urology* 79.3 (2021), pp. 343–350. ISSN: 0302-2838. DOI: https://doi.org/10.1016/j.eururo.2020.11.013.

[35] J. Ma et al. “Efficacy and Safety of ^{225}Ac-PSMA-617-Targeted Alpha Therapy in Metastatic Castration-Resistant Prostate Cancer: A Systematic Review and Meta-Analysis”. In: *Frontiers in Oncology* 12 (Feb. 2022). DOI: 10.3389/fonc.2022.796657.

[36] M. J. Zacherl et al. “First Clinical Results for PSMA-Targeted α-Therapy Using ^{225}Ac-PSMA-I&T in Advanced-mCRPC Patients”. In: *Journal of Nuclear Medicine* 62.5 (Oct. 2020), pp. 669–674. DOI: 10.2967/jnumed.120.251017.

[37] C. Kratochwil, U. Haberkorn, and F. L. Giesel. “225Ac-PSMA-617 for Therapy of Prostate Cancer”. In: *Seminars in Nuclear Medicine* 50.2 (Mar. 2020), pp. 133–140. DOI: 10.1053/j.semnuclmed.2020.02.004.

[38] B. Feuerecker et al. “Safety and Efficacy of Ac-225-PSMA-617 in mCRPC after Failure of Lu-177-PSMA”. In: *Journal of Medical Imaging and Radiation Sciences* 50.4 (Dec. 2019), S90. DOI: 10.1016/j.jmir.2019.11.071.

[39] A. K. H. Robertson et al. “Ac decay chain: feasibility studies”. In: *Phys Med Biol* 62.11 (June 2017), pp. 4406–4420.

[40] M. Ljungberg and P. H. Pretorius. “SPECT/CT: an update on technological developments and clinical applications”. In: *The British Journal of Radiology* 91.1081 (Jan. 2018), p. 20160402. DOI: 10.1259/bjr.20160402.

[41] G. Suliman et al. “Half-lives of 221Fr, 217At, 213Bi, 213Po and 209Pb from the 225Ac decay series”. In: *Applied Radiation and Isotopes* 77 (2013), pp. 32–37. ISSN: 0969-8043. DOI: https://doi.org/10.1016/j.apradiso.2013.02.008.

[42] R. R. Wick, M. J. Atkinson, and E. A. Nekolla. “Incidence of leukaemia and other malignant diseases following injections of the short-lived α-emitter ^{224}Ra into man”. In: *Radiation and Environmental Biophysics* 48.3 (Aug. 2009), pp. 287–294. ISSN: 1432-2099. DOI: 10.1007/s00411-009-0227-y.

[43] M. R. McDevitt et al. “Tumor Therapy with Targeted Atomic Nanogenerators”. In: *Science* 294.5546 (Nov. 2001), pp. 1537–1540. DOI: 10.1126/science.1064126.

[44] S. Sofou et al. “Enhanced Retention of the α-Particle-Emitting Daughters of Actinium-225 by Liposome Carriers”. In: *Bioconjugate Chemistry* 18.6 (2007). PMID: 17935286, pp. 2061–2067. DOI: 10.1021/bc070075t.

[45] T. Poikela et al. “Timepix3: A 65K channel hybrid pixel readout chip with simultaneous ToA/ToT and sparse readout”. In: *Journal of Instrumentation* 9 (May 2014), p. C05013. DOI: 10.1088/1748-0221/9/05/C05013.

[46] A. Sopczak. “Luminosity Measurements at the LHC at CERN Using Medipix, Timepix and Timepix3 Devices”. In: *Physics* 3.3 (Aug. 2021), pp. 579–654. DOI: 10.3390/physics3030037.

[47] C. Ponchut and M. Ruat. “Energy calibration of a CdTe X-ray pixel sensor hybridized to a Timepix chip”. In: 8.01 (Jan. 2013), p. C01005. DOI: 10.1088/1748-0221/8/01/C01005.

[48] M. Kroupa et al. “Techniques for precise energy calibration of particle pixel detectors”. In: *Review of Scientific Instruments* 88.3 (Mar. 2017), p. 033301. DOI: 10.1063/1.4978281.

[49] L. D. Cabrera Gonzalez et al. “Study of charge sharing effect and energy resolution of the Timepix hybrid detector based on gallium arsenide compensated with chromium”. In: *Nucleus (La Habana)* (2018), pp. 30–36.

[50] C. Granja et al. “Resolving power of pixel detector Timepix for wide-range electron, proton and ion detection”. In: *Nuclear Instruments and Methods in Physics Research Section A: Accelerators, Spectrometers, Detectors and Associated Equipment* 908 (Nov. 2018), pp. 60–71. ISSN: 0168-9002. DOI: 10.1016/j.nima.2018.08.014.

[51] J. Bouchami et al. “Measurement of pattern recognition efficiency of tracks generated by ionizing radiation in a Medipix2 device”. In: *Nuclear Instruments and Methods in Physics Research Section A: Accelerators, Spectrometers, Detectors and Associated Equipment* 633 (May 2011), S187–S189. DOI: 10.1016/j.nima.2010.06.163.

[52] J. Jakubek. “Precise energy calibration of pixel detector working in time-over-threshold mode”. In: *Nuclear Instruments and Methods in Physics Research Section A: Accelerators, Spectrometers, Detectors and Associated Equipment* 633 (2011). 11th International Workshop on Radiation Imaging Detectors (IWORID), S262–S266. ISSN: 0168-9002. DOI: https://doi.org/10.1016/j.nima.2010.06.183.

[53] M. Kroupa et al. “Energy resolution and power consumption of Timepix detector for different detector settings and saturation of front-end electronics”. In: *Journal of Instrumentation* 9.05 (May 2014), pp. C05008–C05008. DOI: 10.1088/1748-0221/9/05/c05008.

[54] S. M. Abu Al Azm et al. “Response of Timepix detector with GaAs:Cr and Si sensor to heavy ions”. In: *ArXiv* (June 2017). DOI: 10.48550/arXiv.1706.03245.

[55] S. P. George et al. “Very high energy calibration of silicon Timepix detectors”. In: *Journal of Instrumentation* 13.11 (Nov. 2018), P11014–P11014. DOI: 10.1088/1748-0221/13/11/p11014.

[56] M. Sommer et al. “High-energy per-pixel calibration of timepix pixel detector with laboratory alpha source”. In: *Nuclear Instruments and Methods in Physics Research Section A: Accelerators, Spectrometers, Detectors and Associated Equipment* 1022 (2022), p. 165957. ISSN: 0168-9002. DOI: https://doi.org/10.1016/j.nima.2021.165957.

[57] ADVACAM s.r.o. *User Manual - Timepix3*. English. ADVACAM. 2020.

[58] D. Turecek et al. “Energy calibration of pixel detector working in Time-Over-Threshold mode using test pulses”. In: *2011 IEEE Nuclear Science Symposium Conference Record*. IEEE, Oct. 2011. DOI: 10.1109/nssmic.2011.6154668.

[59] M. Holik et al. “Alpha calibration of the Timepix pixel detector exploiting energy information gained from a common electrode signal”. In: *Journal of Instrumentation* 14.06 (June 2019), pp. C06022–C06022. DOI: 10.1088/1748-0221/14/06/c06022.

[60] ADVACAM s.r.o. *Calibration protocol for Timepix3 detectors - Internal technical report*. English. ADVACAM. 2020. 19 pp.

[61] A. Rathi. Jan. 2023.

[62] E. D. Bosne. “Timepix and FitPix detection system for RBS/C materials analysis”. PhD thesis. 2013.

[63] *Gamma camera - Radiology Cafe*. [Online; accessed 30. Jan. 2023]. Oct. 2021. URL: https://www.radiologycafe.com/frcr-physics-notes/molecular-imaging/gamma-camera.

[64] J. A. Sorenson and M. E. Phelps. *Physics in Nuclear Medicine*. 4th ed. London, England: W.B. Saunders, Apr. 2012.

[65] International Atomic Energy Agency and D L Bailey, eds. *Nuclear medicine physics*. Vienna, Austria: IAEA, Mar. 2015.

[66] J. Ryu et al. “Experimental characterization of alpha spectrometer for optimization of operational parameters affecting energy resolution and detection efficiency”. In: *J. Radioanal. Nucl. Chem.* 329.2 (Aug. 2021), pp. 959–967. ISSN: 1588-2780. DOI: 10.1007/s10967-021-07821-w.

[67] Q. Chen et al. “Label-free photoacoustic imaging of the cardio-cerebrovascular development in the embryonic zebrafish”. In: *Biomed. Opt. Express* 8.4 (Apr. 2017), pp. 2359–2367. ISSN: 2156-7085. DOI: 10.1364/BOE.8.002359.

[68] S. W. Smith. *The scientist and engineer’s guide to digital signal processing*. California Technical Pub, Dec. 1997.

[69] N. Gillings et al. “EANM guideline on the validation of analytical methods for radiopharmaceuticals”. In: *EJNMMI Radiopharmacy and Chemistry* 5.1 (Feb. 2020). DOI: 10.1186/s41181-019-0086-z.

[70] *Conversation with Erik de Blois*. Personal Communication. 2023.

[71] X. Tian et al. “The evolution of proton beam therapy: Current and future status”. In: *Molecular and Clinical Oncology* 8.1 (Jan. 2018), p. 15. DOI: 10.3892/mco.2017.1499.

[72] E. Sengbusch et al. “Maximum proton kinetic energy and patient-generated neutron fluence considerations in proton beam arc delivery radiation therapy”. en. In: *Med. Phys.* 36.2 (Feb. 2009), pp. 364–372.

[73] T. Mitin and A. L. Zietman. “Promise and Pitfalls of Heavy-Particle Therapy”. In: *Journal of Clinical Oncology* 32.26 (Sept. 2014), pp. 2855–2863. DOI: 10.1200/jco.2014.55.1945.

[74] A.-C. Knopf and A. Lomax. “In vivo proton range verification: a review”. In: *Physics in Medicine & Biology* 58.15 (July 2013), R131. ISSN: 0031-9155. DOI: 10.1088/0031-9155/58/15/R131.

[75] T. Toet. *Sample Holder*. Photograph. 2023.

[76] D. Demir, M. Erolu, and A. Turucu. “Studying of characteristics of the HPGe detector for radioactivity measurements”. In: *Journal of Instrumentation* 8.10 (Oct. 2013), P10027. ISSN: 1748-0221. DOI: 10.1088/1748-0221/8/10/P10027.

[77] T. Aoki et al. “Transport Properties of CdTe X/ γ-Ray Detectors With p-n Junction”. In: *IEEE Transactions on Nuclear Science* 58.1 (Dec. 2010), pp. 354–358. ISSN: 1558-1578. DOI: 10.1109/TNS.2010.2090173.

[78] Z. Dali et al. “Energy response of GECAM X and gamma-ray detector prototype”. In: (Apr. 2018).

[79] E. Caroli et al. “A focal plane detector design for a wide-band Laue-lens telescope”. In: *Experimental Astronomy* 20.1 (Dec. 2005), pp. 341–351. ISSN: 1572-9508. DOI: 10.1007/s10686-006-9047-0.

[80] *Regeling goedgekeurde ionisatie-rookmelders 2004*. May 2004.

[81] *Environmental Assessment of Ionization Chamber Smoke Detectors Containing Am-241 (NUREG / CR-1156)*. [Online; accessed 2. May 2023]. Mar. 2021. URL: https://www.nrc.gov/reading-rm/doc-collections/nuregs/contract/cr1156/index.html.

[82] M. Thijs. *X-Y Stage in Python / Spyder*. Reactor Instituut Delft. 2023.

[83] J. Daintith, ed. *A dictionary of physics*. en. 6th ed. London, England: Oxford University Press, Feb. 2009. ISBN: 9780199233991.

[84] X. Llopart et al. “Timepix4, a large area pixel detector readout chip which can be tiled on 4 sides providing sub-200 ps timestamp binning”. In: *J. Instrum.* 17.01 (Jan. 2022), p. C01044. ISSN: 1748-0221. DOI: 10.1088/1748-0221/17/01/C01044.

[85] *A novel method to assess the incident angle and the LET of protons using a compact single-layer Timepix detector*. [Online; accessed 25. May 2023]. Oct. 2022. DOI: 10.1016/j.radphyschem.2022.110349.

[86] G. A. P. Cirrone et al. “A 62-MeV proton beam for the treatment of ocular melanoma at Laboratori Nazionali del Sud-INFN”. In: *IEEE Transactions on Nuclear Science* 51.3 (2004), pp. 860–865. DOI: 10.1109/TNS.2004.829535.

[87] J. G. Mwakisege, G. Schweitzer, and S. Mirzadeh. “Synthesis and Stability of Actinium-225 Endohedral Fullerenes, 225Ac@C60”. In: *ACS Omega* (Oct. 2020). DOI: 10.1021/acsomega.0c01659.

[88] H. Bateman. “The solution of a system of differential equations occurring in the theory of radioactive transformations”. In: *Proceedings of the Cambridge Philosophical Society* 15 (1910). URL: https://www.biodiversitylibrary.org/item/97262#page/483/mode/1up.

A

Appendix

A.1. Activity of Ac-225 and Fr-225

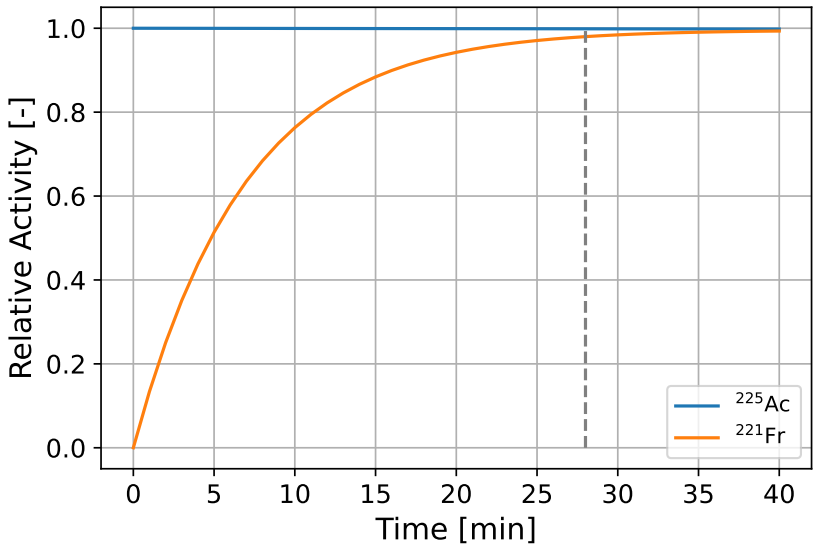

Figure A.1: Simulated activity of ^{225}Ac and its daughter ^{221}Fr, with a dashed vertical line at 6 half-life times of the daughter indicating equilibrium. In this case no ^{221}Fr was initially present.

A.2. Activity of Ac-225 and daughters using the Bateman equations

In order to show the growth of the daughters in an initial situation of pure ^{225}Ac and that the daughters will indeed eventually reach equilibrium, the activities are simulated using the Bateman Equations, which are as follows [88]:

$$A_n(t) = N_1(0)\left(\prod_{j=1}^{n}\lambda_j\right)\sum_{i=1}^{n}\left(\frac{e^{-\lambda_i t}}{\prod_{m=1,m\neq i}^{n}(\lambda_m-\lambda_i)}\right). \tag{A.1}$$

For this equation, it is assumed that initially there is only ^{225}Ac present, which is indicated by $N_1(0)$. $A_n(t)$ describes the activity of nuclide n and λ_n is the decay constant of nuclide n. For simplicity, the decay chain is taken with the only possible path being: $^{225}\text{Ac} \xrightarrow{\alpha} {}^{221}\text{Fr} \xrightarrow{\alpha} {}^{217}\text{At} \xrightarrow{\alpha} {}^{213}\text{Bi} \xrightarrow{\beta} {}^{213}\text{Po} \xrightarrow{\alpha}$. This results in the following behaviour, shown in Figure A.2.

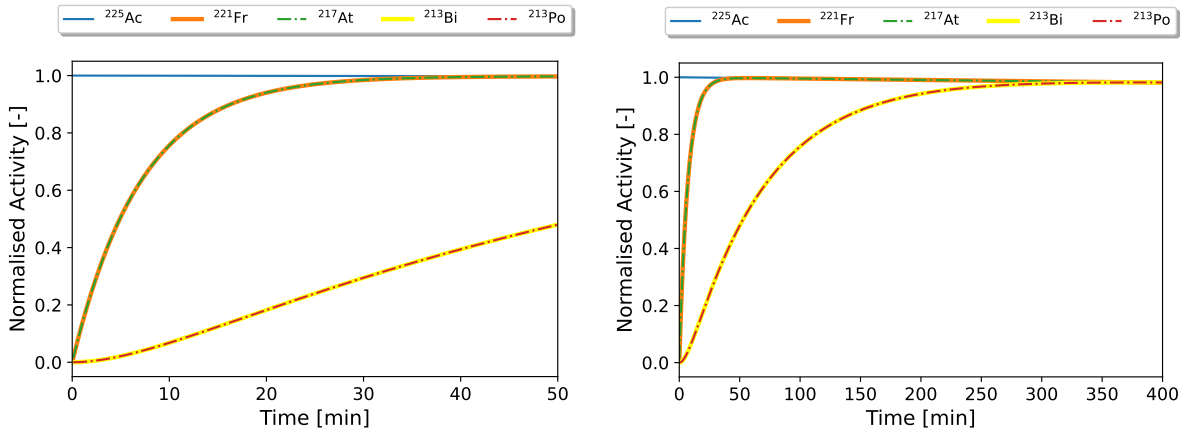

Figure A.2: Simulated activity of ^{225}Ac and daughters in a situation where only ^{225}Ac is initially present using the Bateman equations for different timescales.

A.3. 70MeV 2nA 39mm RW3 extended spectrum

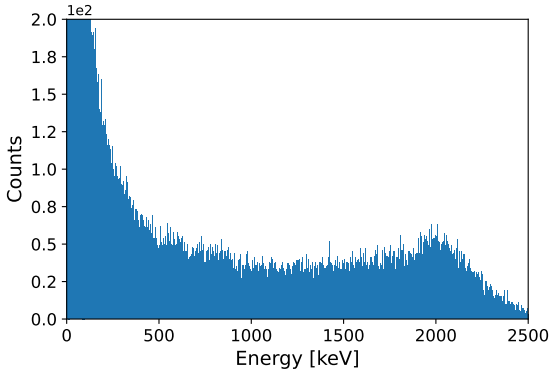

Figure A.3: Measured energy spectrum of the 70MeV proton beam measurement with 2nA intensity, pencil beam geometry and 39mm RW3 where the proton beam was aimed at the Timepix chip. Here the x-axis is extended further. The Timepix was set with a threshold of 2.01keV and a bias voltage of 30V

A.4. Protons measured from Silicon wafer compared to literature

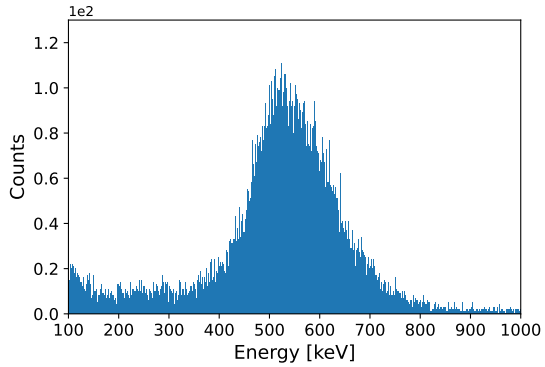

(a) Measured energy spectrum of the 70MeV proton beam measurement with 2nA intensity and pencil beam geometry where the proton beam was aimed at a Si wafer and the Timepix at 50mm distances from the wafer. Here the peak around 520keV is focussed. The Timepix was set with a threshold of 2.01keV and a bias voltage of 30V.

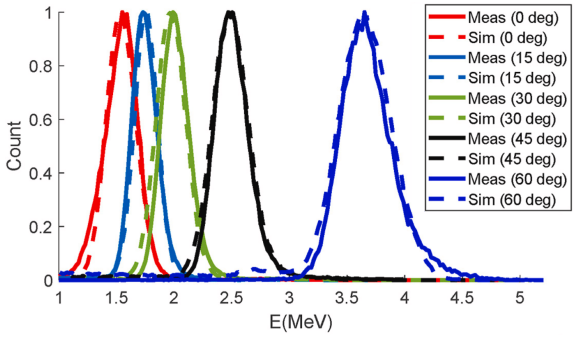

(b) Measured and simulated deposited energy spectra for a 500µm Si MINI-PIX detector [85]. Here 31MeV protons are shown at different incidences.

Figure A.4: Comparison between the measured scattered protons from the Si wafer experiment and literature.

A.5. Data analysis code: single

```
"""
@authors: Erik van Lieshout, Tanja Yagoubova
"""
import numpy as np
import matplotlib.pyplot as plt
import pandas as pd
import time
import cv2
import os
from scipy.ndimage import label, center_of_mass
import glob

#This is the code to process .t3pa datafiles from the Timepix3 detector.
#This variant processes datafiles one by one, there is also a code that uses
#multiprocessing to fully utilise all processing power of the CPU by processing multiple
#at the same time.

#It requires 4 .npy files, numpy arrays, which are the a and b calibration values,
#the faulty indexes and the alpha calibration values.

#The code outputs three .npy files into a folder called 'verwerkt', which are the
#alpha, beta/gamma and single hit measurements. Each np array contains the values of
#center of mass y,x values and energy of each detection.

#There are some settings to play with, which are currently fine for measuring Ac225
#and probably more situations.

#This is a setting to remove alphas, which are mistaken as betas from the beta spectrum.
#Here you can set the maximum expected energy value of betas in keV
max_expected_beta_E = 60000 #Now set very high so no betas are removed

#Set particle pixel size to exclude small pixels in alpha analysis
pixel_thr = 10

#Here you can indicate if you want an alpha calibration or not
alpha_calib = True

#This is the difference in ToA value where the code will later split particles with
time_diff = 5000
```

```
40
41 #This setting defines the minimal roundness for a cluster to be identified as an alpha
       particle, max 1.
42 minimal_roundness = 0.6
43
44
45 #Which files to load:
46 # absolute path to search all text files inside a specific folder
47 #The * symbol is used to indicate that text can be variable:
48 #example: files in folder: a00.t3pa, a11.t3pa, a49.t3pa.
49 #Using r'a*.t3pa' will place all these files in a list.
50 #This is mostly used when you have multiple t3pa files with measurement number.
51 #A single specific filename can also be used
52 path = r'*.t3pa'
53 files = glob.glob(path)
54 if len(files) == 0:
55     print("No files specified")
56 else:
57     print('List of files to be processed:',files)
58
59 if not os.path.exists('verwerkt'):
60    # Create verwerkt folder if it does not exist
61    os.makedirs('verwerkt')
62
63 #load necessary .npy files
64 a_cal = np.load('a_matrix.npy') #256,256 a coefficients
65 b_cal = np.load('b_matrix.npy') #256,256 b coefficients
66 faulty_index_matrix = np.load('faulty_matrix.npy') #256,256 True/False for faulty pixels.
       True == Faulty pixel
67 alpha_calib_arr = np.load('alpha_calib.npy') #avg measured energy of am241 per pixel
       determined by the alpha calibration
68 alpha_calib_avg = np.average(alpha_calib_arr) #avg measured energy of am241 of whole surface
69
70 size = 256 #pixels per direction
71
72 #setup a matrix that defines the borders. It is 256x256 and is True for the borders.
73 #it is used as a mask to check if a particle coincides with the border, which is then
       excluded.
74 borders = np.tile(True,(size,size))
75 borders[1:(size-1),1:(size-1)] = False
76
77 #Setup a matrix that returns the index. It is used multiple times, since it provides
78 #a fast way to retrieve index values when using masks
79 #such that: indices[20,50]=[20,50]
80 x = np.arange(0, size, 1,dtype=int) #or np.shape(particle_matrix)[1]
81 y = np.arange(0, size, 1,dtype=int) #or np.shape(particle_matrix)[0]
82 x_arr = np.tile(x,(size,1)) #or np.shape(particle_matrix)[0]
83 y_arr = np.tile(y,(size,1)).T #or np.shape(particle_matrix)[1]
84 indices = np.dstack((y_arr,x_arr))
85
86
87
88 def apply_calibration(a_cal,b_cal,arr,mask):
89     #This is the pixel calibration based on single pixel hit gammas
90     #The resulting calibration was of the form y=ax+b
91         #The function defines a region (the mask) and gives the values of the particle
92         #Using this, the calibration values are extracted from the matrix and the calculation
               is done efficiently.
93     a_cal,b_cal = a_cal[mask], b_cal[mask]
94     arr[mask] = a_cal*arr[mask] + b_cal
95     return arr
96
97 def apply_alpha_calib(alpha_calib_arr,alpha_calib_avg,x,y,E_val):
98     #This is an extra calibration step to uniform the response for alphas
99     #There is only one datapoint, which is on average 1731keV==alpha_calib_avg
100    #The calib_arr are measured values per pixel, which will result in an deviation from the
           average
101    #Since there is only one datapoint, it is assumed that the deviation increases as much as
           the measured value
102    #increases.
103    #it will only be performed on alphas
```

```
    ratio = E_val/alpha_calib_avg
    deviation = (alpha_calib_arr[y,x]-alpha_calib_avg)
    return E_val - deviation*ratio


for datafile in files:
    print("Now at file : {}".format(datafile))
    load_time = time.time()
    df = pd.read_csv(datafile, sep='\t')
    #Datafile is converted to numpy array. Importing with pd, then to np is much faster
    #Only these four columns are used
    data= df[['Matrix Index','ToA','ToT','FToA']].to_numpy(dtype=np.int32)
    print( "Opening took", round(time.time() - load_time,5), "s to run")

    start_time = time.time()

    #Here matrix index is converted into (x,y) data.

    rows, columns = data[:,0]//size, data[:,0]%size
    data[:,0] = columns
    data = np.insert(data, 0, rows, axis = 1)
    #Columns are now: 'x','y','ToA','ToT','FToA'

    #Correct ToA values with FToA values and removing FToA column
    #calculate accurate times with FToA with: toa=toa*25-ftoa*25/16
    data[:,2] = data[:,2]*25 - data[:,4]*25/16
    #then remove ftoa column
    data = np.delete(data, 4, 1)
    #Columns are now: 'x','y','ToA','ToT'
        #Note: Even though it is a FToA, it will be referenced to as ToA due to code already
            been build on ToA


    #Here empty arrays are created to hold particle data
    alphas_all = np.empty((0,3))
    betas_gammas_all = np.empty((0,3))
    single_hit_all = np.empty((0,3))


    #Here the ToA difference of all lines in the dataset will be calculated
    difference = np.diff(data[:,2])
    #if the time difference is greater than a chosen threshold, the line of data belongs to a
        different particle
    #the code will split the dataset based on large time differences.
    difference[abs(difference)<time_diff] = 0
    particles_all = np.split(data,np.where(difference)[0]+1)

    #it is still possible that 2 particles were detected at the same time, later on there
        will also be
    #a split of data based on position.
    for i in range(len(particles_all)): #loop over all the time splitted particles

        #Here the ToA and ToT data of a time splitted particle is placed in a 256x256 array.
        particle = particles_all[i]  #particle matrix of the same time, can be multiple
            particles
        particle_TOT_matrix = np.zeros((size,size)) #create a matrix that holds (uncalibrated
            ) TOT values
        particle_TOA_matrix = np.zeros((size,size)) #create a matrix that holds (uncalibrated
            ) TOA values
        row, column = particle[:,0], particle[:,1] #calculate the row index #calculate the
            column index
        particle_TOT_matrix[row,column] = particle[:,3]  #create an image of the single
            particle with tot
        particle_TOA_matrix[row,column] = particle[:,2]  #create an image of the single
            particle with tot


        # This can be used to image the particle
        # plt.imshow(particle_matrix)
        # plt.show()
        # time.sleep(0.5)
```

```
166
167         #Here a structure is used. What is does, is it will merge touching pixels based on
                the given structure.
168             #In this case the structure is a 3x3 block with 1's (True's). This means that
                     all pixels (horizontal, vertical, diagonal)
169             #touching the pixel will be merged.
170             #This way if there were 2 particles at the same time, they are now split
                    based on position.
171         #split the particles based on touching indices
172         structure = np.array(([[1,1,1],[1,1,1],[1,1,1]]), dtype=np.int32)
173         labeled, ncomponents = label(particle_TOT_matrix, structure)
174
175
176         for k in range(1,ncomponents+1):
177             particle_stored = False #This variable is used to indicate if a particle is
                    identified and a loop will be stopped.
178             indexparticle = indices[labeled==k] #Here the indices of the labelled particle
                    are retreived.
179             new = np.zeros((size,size)) #A 2d array that holds the TOT value of a single
                    particle. This array will be used to do shape analysis and calculations
180             new[indexparticle[:,0],indexparticle[:,1]]=particle_TOT_matrix[indexparticle
                    [:,0],indexparticle[:,1]] #Here ToT values are inserted based on the index
181
182             #masking pixels that are contained in the particle:
183             new[new<1] = 0 #Due to calibation errors there might be values that are very low
                    or negative, those are removed
184             mask = new>0 #This defines the positions of non zero elements, in order to
                    efficiently apply the calibration
185
186             #check for faulty pixels by checking overlapping mask for particle and faulty
                    pixel mask:
187             #if overlap nothing happend, no overlap: continue with algorithm
188                     #I realise that a dead pixel wont give an overlap, however, the code
                            works anyways and this is most likely
189                     #due to the fact that holes are also filtered out later on.\
190                     #However, a beter method would be to set the neighbouring pixels of
                            the faulty pixels also to True in the Faulty pixel array.
191             if np.sum(mask & faulty_index_matrix)==0:
192
193                 #Calibration of TOT values only for the area with particle:
194                 new = apply_calibration(a_cal, b_cal, new, mask)
195
196                 # plt.xlim(indexparticle[0,1]-10,indexparticle[0,1]+10)
197                 # plt.ylim(indexparticle[0,0]-10,indexparticle[0,0]+10)
198                 # plt.imshow(new)
199                 # plt.colorbar()
200                 # plt.show()
201                 # time.sleep(0.5)
202
203                             #Center of mass is used to define more accurately the center
                                    position of the incomming particle (especially for alphas
                                    )
204                 com = center_of_mass(new) #TOT
205                             #Round the COM values to be used as indices
206                 comy_round, comx_round = round(com[0]), round(com[1])
207                 com_row, com_column = com #TOT
208                             #Also get the maximum value of the particle (this to later on
                                    test if the COM==Max value for symmetry for alphas)
209                 max_row, max_column = indices[new==np.max(new)][0] #TOT
210                 E_sum = new.sum() #The sum of the calibrated ToT values is the energy
211
212                             #Here cv2 is used to create an black and white image, this is
                                    used to retrieve shape information.
213                 img = new.astype(np.uint8)
214                 ret, thresh = cv2.threshold(img, 0.5, 255, 0)  # get a black and white image
215                 contours, hierarchy = cv2.findContours(thresh,  cv2.RETR_EXTERNAL, cv2.
                        CHAIN_APPROX_NONE)[-2:] #find the contours of the particle using cv2
216
217
218                             #now a series of checks are done to check if the particle is
                                    an alpha_calib
```

```
219
220                 if len(contours)>0:
221                     cnt = contours[0]
222                     area = cv2.contourArea(cnt)
223                     perimeter = cv2.arcLength(cnt,True)
224                     if perimeter>0 and len(indexparticle)>pixel_thr: #Filter based on if the
                            particle is larger than the set minimal particle length
225                                                 #calculate the roundness for assessing if the
                                                        particle is an alpha (should be 0.6)
226                         roundness = 4*np.pi*area/(perimeter**2)
227                                                 #ToT values around the com should be above 10
                                                        (can be changed) such that there are no
                                                       holes in the center (due to volcano or
                                                       dead pixels)
228                         around_com = new[(comy_round-1):(comy_round+2),(comx_round-1):(
                                comx_round+2)]
229                                                 #TOA values around TOT max should be higher,
                                                       since the pixels surrounding the Max
                                                       receive charge on a later time (Higer ToA
                                                       ). Only allow 3 to be lower to account
                                                       for displaced TOT/TOA min/max
230                         around_max = particle_TOA_matrix[(max_row-1):(max_row+2),(max_column
                                -1):(max_column+2)]
231                                                 #Here the checks are performed.
232                                                 #There is also a check that removes particles
                                                        on the borders.
233                         if (roundness>minimal_roundness) and (np.all(around_com>10)) and np.
                                sum(around_max<particle_TOA_matrix[max_row,max_column])<=3 and np
                                .sum(mask & borders)==0:
234
235                             #if set to True, perform the alpha calibration
236                             if alpha_calib == True:
237                                 E_sum = apply_alpha_calib(alpha_calib_arr, alpha_calib_avg,
                                        comx_round, comy_round, E_sum)
238
239                                                         #Store the particles data and set
                                                                stored to True (can also be done
                                                                with a while loop)
240                             alphas_all = np.append(alphas_all,[[com_row,com_column,E_sum]],
                                    axis = 0)
241                             particle_stored = True
242
243                             #to show TOT
244                             # plt.title("alpha TOT {}".format(new.sum()))
245                             # plt.xlim(com[1]-10,com[1]+10)
246                             # plt.ylim(com[0]-10,com[0]+10)
247                             # plt.imshow(new)
248                             # plt.colorbar()
249                             # plt.show()
250
251                             #to show TOA
252                             # plt.title("alpha TOA {}".format(new.sum()))
253                             # plt.xlim(com[1]-10,com[1]+10)
254                             # plt.ylim(com[0]-10,com[0]+10)
255                             # plt.imshow(particle_toa)
256                             # plt.clim(particle_toa[round(com[0]),round(com[1])]-10,
                                    particle_toa[round(com[0]),round(com[1])]+10)
257                             # plt.colorbar()
258                             # plt.show()
259
260                                 #This checks if the particle is a beta/gamma with multi hits.
                                        It isnt special. Its just if it is not an alpha and not
                                       a single hit
261                 if (particle_stored == False) and (len(indexparticle)>1) and E_sum<
                        max_expected_beta_E and np.sum(mask & borders)==0:
262
263                                         #Store the data. Here the incident particle position
                                                is the lowest ToA time (Here the FToA is most
                                                important, since ToA can be the same for
264                                         #the same particle.
```

```
265                     index_lowest_toa = indices[particle_TOA_matrix==np.min(
                            particle_TOA_matrix[mask])][0]
266                     betas_gammas_all = np.append(betas_gammas_all,[[index_lowest_toa[0],
                            index_lowest_toa[1],E_sum]],axis = 0)
267
268                     # plt.title("Not-alpha TOT {}".format(new.sum()))
269                     # plt.xlim(com[1]-10,com[1]+10)
270                     # plt.ylim(com[0]-10,com[0]+10)
271                     # plt.imshow(new)
272                     # plt.colorbar()
273                     # plt.show()
274
275                     # plt.title("Not-alpha TOA {}".format(new.sum()))
276                     # plt.xlim(com[1]-10,com[1]+10)
277                     # plt.ylim(com[0]-10,com[0]+10)
278                     # plt.imshow(particle_toa)
279                     # plt.clim(particle_toa[round(com[0]),round(com[1])]-3,particle_toa[round
                            (com[0]),round(com[1])]+3)
280                     # plt.colorbar()
281                     # plt.show()
282
283                                 #Here single pixel hits are stored.
284                 if (particle_stored == False) and (len(indexparticle)==1) and np.sum(mask &
                        borders)==0:
285                     #these can be filtered out beforehand but that only speeds up the code
286                     #if there are a lot single hits, which there are not for ac225
287                     single_hit_all = np.append(single_hit_all,[[com_row,com_column,E_sum]],
                            axis = 0)
288
289
290
291
292     #Here data is saved as .npy (numpy array) files, since this is seriously fast to store
            and load an small in size.
293     np.save('verwerkt/{}_alpha.npy'.format(datafile[:-5]), alphas_all)
294     np.save('verwerkt/{}_beta_gamma.npy'.format(datafile[:-5]), betas_gammas_all)
295     np.save('verwerkt/{}_single_hits.npy'.format(datafile[:-5]), single_hit_all)
296     #move the files that are done to a new folder, you can use this, but some data
            information gets lost.
297     #os.rename("{}".format(datafile), "verwerkt_raw/{}".format(datafile))
298     #os.rename("{}.info".format(datafile), "verwerkt_raw/{}.info".format(datafile))
299     print( "The code took", round(time.time() - start_time,5), "s to run")
```